SINGLE STEP FABRICATION OF SHAPE MORPHING 3D SURFACES

by

AMIRALI NOJOOMI

DISSERTATION

Submitted in partial fulfillment of the requirements

for the degree of Doctor of Philosophy at

The University of Texas at Arlington

May, 2020

Arlington, Texas

Supervising Committee:

Dr. Kyungsuk Yum, Supervising Professor

Dr. Choong-Un Kim

Dr. Seong Jin Koh

Dr. Harry F. Tibbals

Dr. Nancy L. Michael

TO MY PARENTS SUSAN AND KHOSRO,

WITHOUT WHOM NONE OF MY SUCCESS
WOULD BE POSSIBLE.

ACKNOWLEDGMENTS

First and foremost, I would like to express my sincere gratitude to my supervisor, Professor Kyungsuk Yum, for his guidance and kind support during this whole journey. His passion for solving challenges and creativity for novel approaches have been a great source of motivation for me along the way. This work could not have been done without his knowledge, help, encouragement, perseverance, and constructive attitude.

In continuation, I would like to thank the rest of my dissertation committee, Professor Choong-Un Kim, Professor Seong Jin Koh, Professor Harry F. Tibbals, and Dr. Nancy L. Michael for their words of encouragement and intuitive comments that motivated me to keep a focused perspective toward my research work. I would also like to thank all the members of my research group Mr. Hakan Arslan, Mr. Haoqing Yang, Dr. Kwan Lee, and Ms. Astha Jain, for their valuable contributions and constant support. I would like to thank all the professors and staff in the department of materials science and engineering, and Characterization Center for Materials & Biology.

Special thanks to Professor Amir Aghamohammadi and Professor Mohammad Khorrami for their expertise and assistance. I am very grateful to them for imparting all the knowledge and scientific inputs on this work.

Also, I want to thank my friends here in the US for all the support. This journey would not have been possible without them. Most importantly, I want to thank Ava, she is my lucky charm and has been extremely patient and understanding throughout these years. I am not sure I could have done this without her in my life.

Finally, I want to thank my parents for their unconditional love, endless support, and encouragement throughout the years. Without their presence, none of my success would have been possible, and I cannot wait to reunite with them.

May, 2020

LIST OF FIGURES

ABSTRACT

SINGLE STEP FABRICATION OF SHAPE MORPHING 3D SURFACES

Amirali Nojoomi, Ph.D.
The University of Texas at Arlington, 2020

Supervising Professor: Kyungsuk Yum, Ph.D.

Shape-changing materials that can adopt programmable 3-dimensional (3D) shapes offer promise for a wide range of applications. Form the formation of the leaves and flowers to the shaping of complex organs, the analogues of such shape-morphing 3D surfaces are abundant in nature. However, since the formation of such surfaces in biological systems is fundamentally different from that of human-made materials, replicating their complex morphologies, movements, and thereby functions remains a challenge. Inspired by living organisms, we introduce an approach, called digital light 4D printing (DL4P), that encodes thermosensitive 2D hydrogels with a specific pattern of network density and thus temperature-induced growth (expansion and contraction) to create 3D structures with programmed shapes and motions. 3D self-shaping happens readily upon the introduction of the programmed 2D hydrogels into water medium, where programmed non-uniform in-plane growth defines a new metric tensor (target metric) for the surface, which causes a controlled out-of-plane buckling and results in a specific three-dimensional shape. A theoretical platform was introduced for axisymmetric 3D shapes, predicting how a target metric translates to a 3D shape and vice versa. We next introduced modular-based design rules for making complex 3D structures and addressed control of the direction of deformation in non-

Euclidean systems. By controlling the spatial rates of shape transformations, we created 3D structures with complex programmed sequential motions similar to living organisms. To broaden the application of our method beyond soft-materials, we established a thermal/chemical shape stabilization process to achieve robust air-stable 3D surfaces in the ambient environment. Unlike traditional layer-by-layer additive manufacturing, our controlled out-of-plane deformation mechanism allows the creation of 3D structures in a short amount of time from a single layer material. The digital patterning used in this method offers simultaneous printing of 2D materials encoded with custom-designed metrics, rendering it scalable for creating diverse 3D shapes.

TABLE OF CONTENTS

CHAPTER 1

1.1 INTRODUCTION

Shape-changing materials with the ability to adopt programmable 3-dimensional (3D) shapes and motions, known as 4D printing, offer promise for a wide range of applications including, smart textiles[1], soft robotic[2-4], actuators[5-6], shape-changing sensors[7], microfluidic valves[8-9], optical systems [10-11], artificial muscles[12-13], and metrics for bio-separation[13]. Controlled deformation of thin plates, into programmed 3D surfaces, as a form of 4D printing[14], has shown a great potential for the design of complex geometries, hard to achieve with other methods. [15-17] Such methods potentially offer the scalability of the traditional forming processes with the customizability of additive manufacturing with great potential for the creation of complex structures and even motions.

The most straightforward 3D shaping method is based on generating a bending configuration in a planar surface by forming a bilayer cantilever made of layers with different growth (expansion/ contraction) rates[18-19] (Figure 1-1**a**) or directions[20-22] or inducing a growth gradient along the thickness of a thin sheet[23-24]. These configurations can be generally implemented to make smoothly bent surfaces with uniform curvature or to create hinges for origami-like structures. Most of the current approaches use swellable hydrogels[19-20, 25-29], shape-memory polymers[30-31], and liquid crystalline elastomers[32-34] fabricated using photopatterning[19, 24, 26-28], self-folding[19, 24, 35-36], and three-dimensional (3D) printing[20, 31]. These shape morphing thin sheets have been used in many applications, including soft robotic[2-4], actuators[5-6], shape-changing sensors[7], microfluidic valves[8-9], optical systems[10-11], artificial muscles[12-13], and metrics for bio-separation[13].

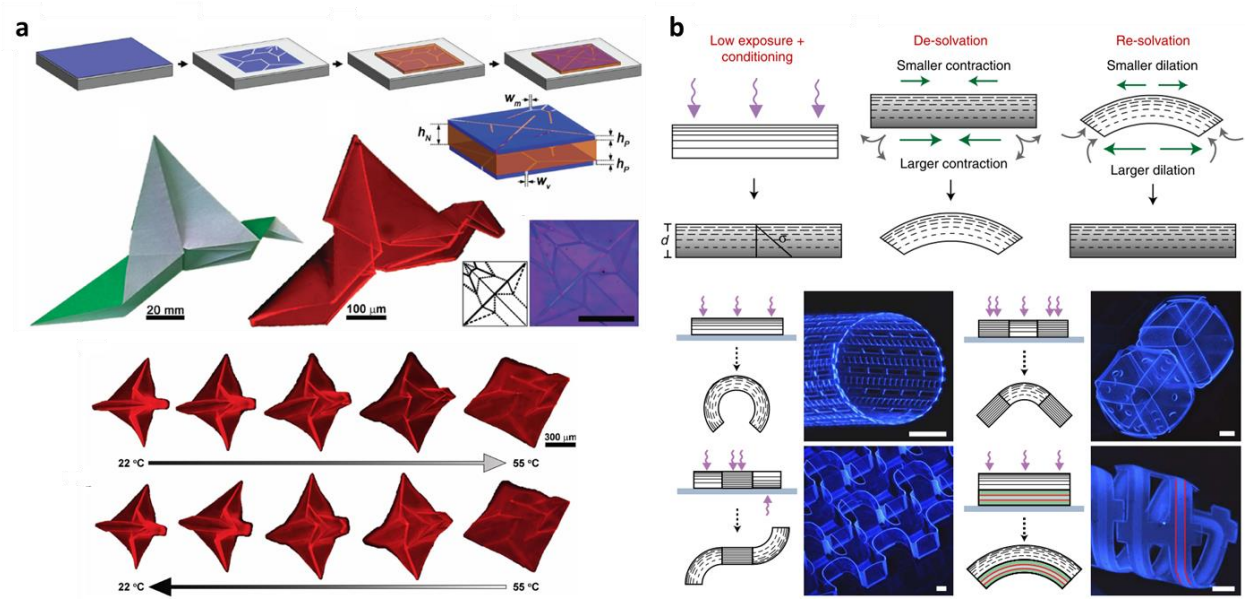

Figure 1-1 **Single direction bending approach for making 3D geometries**. **a** Trilayer structure made of a temperature-responsive polymer sandwiched by glassy polymers patterned with open stripes as hinges. Reversible swelling of the middle layer induces a bending configuration toward the patterned edges[16]. **b** Reversible formation of bent structures through solvent assisted stress formation in a thin epoxy film with a cross-link gradient along its thickness[24]

Although such bending approaches lead to the formation of surfaces with constant and single curvatures (e.g., cylinders and hinges), they fail to make shapes with continuous curvature change (e.g., cone) or doubly curved 3D shapes (e.g., a cap). Limited 3D geometries attainable by these methods have made researchers seek for alternative ways that can offer a broader range of 3D shapes.

One of the most effective methods in this regard is to use thin plates that undergo controlled lateral (in-plane) differential growth (swelling/shrinkage), termed non-Euclidean plates[37]. In this approach, controlled in-plane differential growth (swelling/shrinkage) in thin plates (2D surfaces) causes out-of-plane deformation and forms a 3D surface[25-26, 37]. Here, the controlled non-uniform growth defines new equilibrium distances between points on the 2D surface, leading to a controlled

pattern of internal strain. Since bending energy is more sensitive to thickness ($E_B \sim {t_h}^3$, where t_h is the thickness of a plane) compared to in-plane stretching ($E_S \sim t_h$), the thinner the surface is, the more costly in-plane strains are compared to bending. Therefore, as $t_h \to 0$, the surface configuration tends to adopt out-of-plane bending configuration, resulting in the self-formation of a pre-defined 3D structure (Figure 1-2) (see Section 2.4.2 for more details).

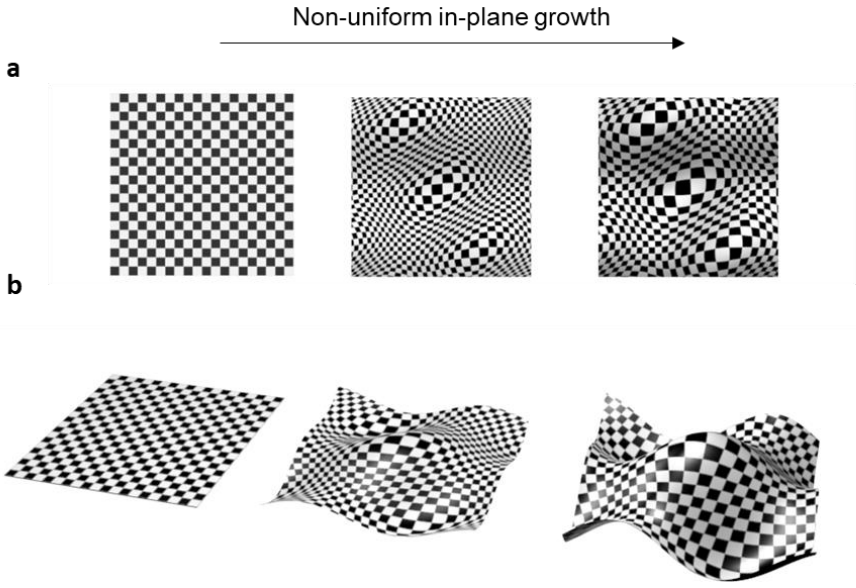

Figure 1-2 **Formation of a target 3D structure by controlled lateral (in-plane) differential growth in a 2D sheet**. **a** Schematic demonstration of a non-uniform growth in a thin plate. **b** Release of internal stresses through out-of-plane deformation, which results in the formation of a programmed 3D structure.

By relying on controlled mechanical instability, this approach creates 3D structures with double curvature geometries[38-39], often seen in natural bodies, such as flowers, skin, or leaves[26, 40]. In contrast to the man-made forming processes, living organisms undergo such mechanical instabilities by creating a controllable distribution of residual stresses under no external confinement to perform various biological processes, including morphogenesis, intricate motions,

and adaptation to environments[25-26, 29, 40-51] (Figure 1-3). Therefore, by controlling this mechanism, we can turn it into a powerful design and shaping strategy to make self-forming 3D surfaces with complex functionalities.

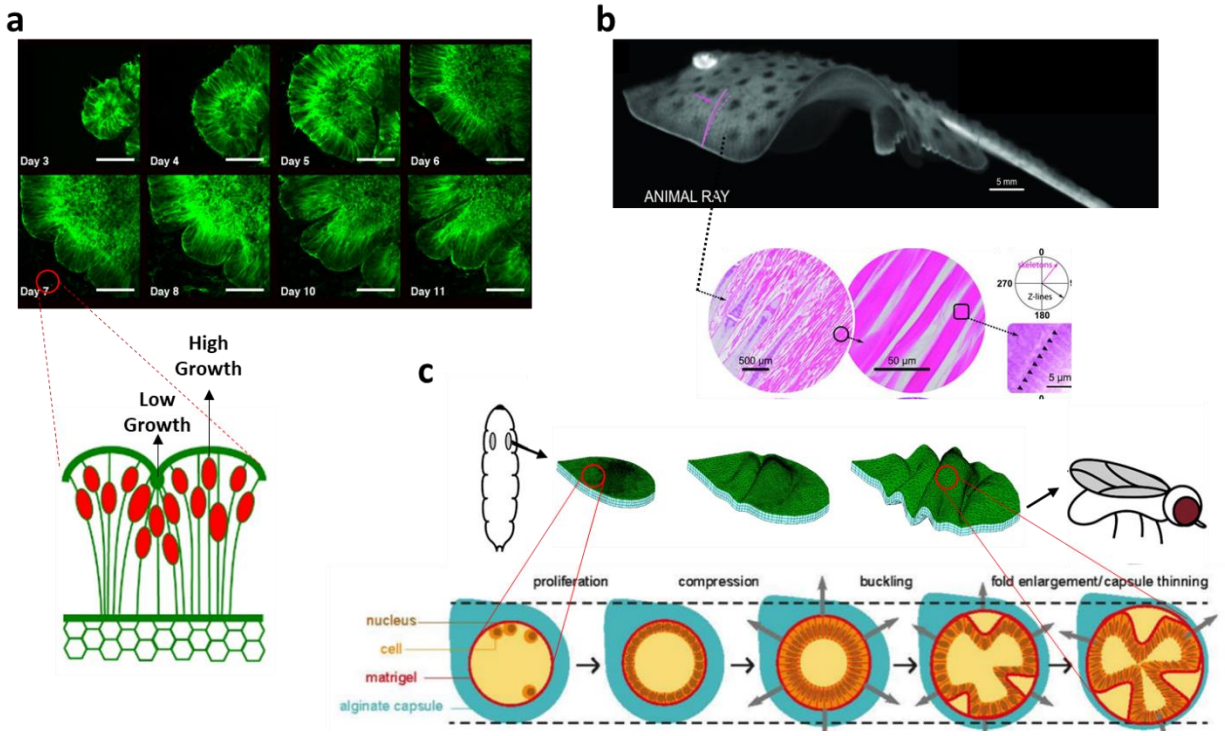

Figure 1-3 **lateral differential growth-induced 3D shaping in living organisms.** Non-uniform cell growth on the brain's surface causes wrinkle formation[52]. **b** Anisotropic muscle expansion (growth) responsible for the complex undulatory swimming motion in batoid fishes[2]. **c** Schematic demonstration of non-uniform growth induced tissue folding as a fundamental process that shapes epithelia into complex 3D organs[53].

By controlling the pattern of lateral growth to make non-Euclidean plates, one can make 3D structures that can mimic not only the complex shape of living organisms but also their continuously deforming motions.[54-55] The physics of non-Euclidean plates is gradually being uncovered, but there are still many open questions. For example, despite the demonstration of 3D shaping for simple geometries,[25-26, 56] 3D structures with complex morphologies have been mostly

unachievable [51, 57-58]. Furthermore, the dynamic growth-induced 3D motions of non-Euclidean plates have remained largely unexplored[25-26]. Furthermore, most of the efforts so far have been focused on the theoretical and experimental aspects of 3D shape formation at equilibrium states[25-26, 56-58], while the dynamic progression of intermediate shapes between equilibrium states has been unexplored.

Aside from theoretical challenges to design and predict the 3D shaping of non-Euclidean surfaces[59-60], there has been a lack of a physical system (both material and fabrication method) capable of creating 2D materials encoded with a precise and continuous pattern of in-plane growth. Current fabrication methods such as injection molding[25] or conventional multi-step lithography[26-27] fail to fabricate structures with continuous and precise growth patterns resulting in poor shape control and limited complexity and accuracy in forming 3D shapes. Moreover, the formation of non-Euclidean surfaces has been mostly limited to soft materials[20, 26, 61-62], or pneumatic devices [63-64] with low mechanical properties, further limiting its potential applications.

In this work, we introduce an approach, called digital light 4D printing (DL4P), that encodes thermosensitive 2D hydrogels with a specific pattern of network density and thus temperature-induced growth (expansion and contraction) to make 3D structures with programmed shapes and motions.

1.2 OVERVIEW OF THE CHAPTERS

In the second chapter of this study, we used the DL4P method to encode 2D polymers with specific growth patterns (Ω) through spatial and temporal control of photo-polymerization and crosslinking reactions via digital light projection grayscale lithography[65]. We developed a photo-polymerizable prepolymer solution of poly(*N*-isopropylacrylamide), a hydrogel with temperature-induced hydrophilic/hydrophobic transition in water. We showed that the use of two types of crosslinkers with different molecular weights increases the range of polymer's tunability during photopolymerization. We used light exposure time to control the polymerization and crosslinking reactions of the prepolymer and thus modulate the subsequent expansion and contraction of the created polymer in a water medium. The grayscale light pattern during polymerization defines the local network and cross-linking densities of the hydrogel, which results in controlled expansion and contraction and allows 3D-shape formation at both swelled and shrunk states for the first time[65]. Also, controlling density provides control over the growth (swelling/shrinking) rate, resulting in the ability to program growth-induced 3D motions.

Single-step digital photo-printing enabled us to use a modular approach for creating complex 3D structures with diverse geometries and motions[26]. We addressed the fundamental problem of the direction control of deformation associated with non-Euclidean surfaces by introducing the concept of transition components.

Our study revealed that the non-uniform rates of swelling and shrinking throughout the hydrogel surface determine the progressive shape-change of it while interchanging between different equilibrium states. To study the progressive shape-change of the 3D surfaces, we introduced the concept of dynamic target metric by studying the relationship between the photo-

polymerization light exposure and the local rate of growth in the hydrogel to predict the dynamic configuration of the structures during the temperature change. These findings helped us to design dynamic 3D structures with complex motions, including ray-inspired 3D structures with programmed motions.

In the third chapter, we introduce a stabilization process to create robust solid 3D structures from 3D hydrogels in the shrunk state. Although 3D forming relies on the controlled 3D buckling of 2D hydrogels in water, we achieved robust air-stable 3D solid structures by stabilizing the 3D shape of the hydrogels formed the shrunk state.

The absence of the moving parts eases the specific rheological ink requirements and makes this method adaptable to a variety of inks with different properties. Building on this capability, we printed composite 3D structures by introducing a wide range of reinforcing phases to the prepolymer solution to make composite structures with tunable mechanical properties similar to the engineering polymers. We also developed a multi-material approach to construct 3D structures with specific material patterns that enable the creation of 3D shapes with point-by-point material control.

References

1.Hu, J.; Meng, H.; Li, G.; Ibekwe, S. I., A review of stimuli-responsive polymers for smart textile applications. *Smart Materials and Structures* **2012,** *21* (5), 053001.
2. Park, S.-J.; Gazzola, M.; Park, K. S.; Park, S.; Di Santo, V.; Blevins, E. L.; Lind, J. U.; Campbell, P. H.; Dauth, S.; Capulli, A. K., Phototactic guidance of a tissue-engineered soft-robotic ray. *Science* **2016,** *353* (6295), 158-162.
3. Maeda, S.; Hara, Y.; Sakai, T.; Yoshida, R.; Hashimoto, S., Self-walking gel. *Advanced Materials* **2007,** *19* (21), 3480-3484.
4.Palagi, S.; Fischer, P., Bioinspired microrobots. *Nature Reviews Materials* **2018,** *3* (6), 113.
5. Techawanitchai, P.; Ebara, M.; Idota, N.; Asoh, T.-A.; Kikuchi, A.; Aoyagi, T., Photo-switchable control of pH-responsive actuators via pH jump reaction. *Soft Matter* **2012,** *8* (10), 2844-2851.
6.Asoh, T. a.; Matsusaki, M.; Kaneko, T.; Akashi, M., Fabrication of Temperature-Responsive Bending Hydrogels with a Nanostructured Gradient. *Advanced Materials* **2008,** *20* (11), 2080-2083.
7.Matsumoto, A.; Ishii, T.; Nishida, J.; Matsumoto, H.; Kataoka, K.; Miyahara, Y., A synthetic approach toward a self-regulated insulin delivery system. *Angewandte Chemie International Edition* **2012,** *51* (9), 2124-2128.
8.Kieviet, B. D.; Schön, P. M.; Vancso, G. J., Stimulus-responsive polymers and other functional polymer surfaces as components in glass microfluidic channels. *Lab on a Chip* **2014,** *14* (21), 4159-4170.
9.Ebara, M.; Uto, K.; Idota, N.; Hoffman, J. M.; Aoyagi, T., Rewritable and shape-memory soft matter with dynamically tunable microchannel geometry in a biological temperature range. *Soft Matter* **2013,** *9* (11), 3074-3080.
10.Zhang, M.; Rabiah, N. I.; Ngo, T. H.; Otanicar, T. P.; Phelan, P. E.; Swaminathan, R.; Dai, L. L., Thermo-responsiveness and tunable optical properties of asymmetric polystyrene/PNIPAM-gold composite particles. *Journal of colloid and interface science* **2014,** *425*, 12-19.
11.Dong, L.; Agarwal, A. K.; Beebe, D. J.; Jiang, H., Adaptive liquid microlenses activated by stimuli-responsive hydrogels. *Nature* **2006,** *442* (7102), 551.
12. Takashima, Y.; Hatanaka, S.; Otsubo, M.; Nakahata, M.; Kakuta, T.; Hashidzume, A.; Yamaguchi, H.; Harada, A., Expansion–contraction of photoresponsive artificial muscle regulated by host–guest interactions. *Nature communications* **2012,** *3* (1), 1-8.
13.Nagase, K.; Kobayashi, J.; Okano, T., Temperature-responsive intelligent interfaces for biomolecular separation and cell sheet engineering. *Journal of the Royal Society Interface* **2009,** *6* (suppl_3), S293-S309.
14.Momeni, F.; Liu, X.; Ni, J., A review of 4D printing. *Materials & design* **2017,** *122*, 42-79.
15.Jamal, M.; Zarafshar, A. M.; Gracias, D. H., Differentially photo-crosslinked polymers enable self-assembling microfluidics. *Nature communications* **2011,** *2* (1), 1-6.
16.Na, J. H.; Evans, A. A.; Bae, J.; Chiappelli, M. C.; Santangelo, C. D.; Lang, R. J.; Hull, T. C.; Hayward, R. C., Programming reversibly self-folding origami with micropatterned photo-crosslinkable polymer trilayers. *Advanced Materials* **2015,** *27* (1), 79-85.

17.Gladman, A. S.; Matsumoto, E. A.; Nuzzo, R. G.; Mahadevan, L.; Lewis, J. A., Biomimetic 4D printing. *Nature materials* **2016,** *15* (4), 413-418.
18.Ding, Z.; Yuan, C.; Peng, X.; Wang, T.; Qi, H. J.; Dunn, M. L., Direct 4D printing via active composite materials. *Science advances* **2017,** *3* (4), e1602890.
19.Jamal, M.; Kadam, S. S.; Xiao, R.; Jivan, F.; Onn, T. M.; Fernandes, R.; Nguyen, T. D.; Gracias, D. H., Bio-origami hydrogel scaffolds composed of photocrosslinked PEG bilayers. *Advanced healthcare materials* **2013,** *2* (8), 1142-1150.
20.Gladman, A. S.; Matsumoto, E. A.; Nuzzo, R. G.; Mahadevan, L.; Lewis, J. A., Biomimetic 4D printing. *Nature materials* **2016**.
21.Kotikian, A.; Truby, R. L.; Boley, J. W.; White, T. J.; Lewis, J. A., 3D printing of liquid crystal elastomeric actuators with spatially programed nematic order. *Advanced Materials* **2018,** *30* (10), 1706164.
22.Arslan, H.; Nojoomi, A.; Jeon, J.; Yum, K., 3D Printing of Anisotropic Hydrogels with Bioinspired Motion. *Advanced Science* **2018**, 1800703.
23. Zhao, Z.; Wu, J.; Mu, X.; Chen, H.; Qi, H. J.; Fang, D., Origami by frontal photopolymerization. *Science Advances* **2017,** *3* (4), e1602326.
24.Jamal, M.; Zarafshar, A. M.; Gracias, D. H., Differentially photo-crosslinked polymers enable self-assembling microfluidics. *Nature communications* **2011,** *2*, 527.
25.Klein, Y.; Efrati, E.; Sharon, E., Shaping of Elastic Sheets by Prescription of Non-Euclidean Metrics. *Science* **2007,** *315* (5815), 1116-1120.
26.Kim, J.; Hanna, J. A.; Byun, M.; Santangelo, C. D.; Hayward, R. C., Designing Responsive Buckled Surfaces by Halftone Gel Lithography. *Science* **2012,** *335* (6073), 1201-1205.
27.Wu, Z. L.; Moshe, M.; Greener, J.; Therien-Aubin, H.; Nie, Z.; Sharon, E.; Kumacheva, E., Three-dimensional shape transformations of hydrogel sheets induced by small-scale modulation of internal stresses. *Nature communications* **2013,** *4*, 1586.
28. Cangialosi, A.; Yoon, C.; Liu, J.; Huang, Q.; Guo, J.; Nguyen, T. D.; Gracias, D. H.; Schulman, R., DNA sequence-directed shape change of photopatterned hydrogels via high-degree swelling. *Science* **2017,** *357* (6356), 1126-1130.
29.Kuksenok, O.; Balazs, A. C., Modeling the photoinduced reconfiguration and directed motion of polymer gels. *Advanced Functional Materials* **2013,** *23* (36), 4601-4610.
30.Lendlein, A.; Jiang, H.; Jünger, O.; Langer, R., Light-induced shape-memory polymers. *Nature* **2005,** *434* (7035), 879-882.
31.Ge, Q.; Sakhaei, A. H.; Lee, H.; Dunn, C. K.; Fang, N. X.; Dunn, M. L., Multimaterial 4D printing with tailorable shape memory polymers. *Scientific reports* **2016,** *6*, 31110.
32. Iamsaard, S.; Aßhoff, S. J.; Matt, B.; Kudernac, T.; Cornelissen, J. J.; Fletcher, S. P.; Katsonis, N., Conversion of light into macroscopic helical motion. *Nature chemistry* **2014,** *6* (3), 229-235.
33.Ware, T. H.; McConney, M. E.; Wie, J. J.; Tondiglia, V. P.; White, T. J., Voxelated liquid crystal elastomers. *Science* **2015,** *347* (6225), 982-984.
34.White, T. J.; Broer, D. J., Programmable and adaptive mechanics with liquid crystal polymer networks and elastomers. *Nature materials* **2015,** *14* (11), 1087-1098.
35.Na, J. H.; Evans, A. A.; Bae, J.; Chiappelli, M. C.; Santangelo, C. D.; Lang, R. J.; Hull, T. C.; Hayward, R. C., Programming reversibly self-folding origami with micropatterned photo-crosslinkable polymer trilayers. *Adv Mater* **2015,** *27* (1), 79-85.

36.Liu, Y.; Shaw, B.; Dickey, M. D.; Genzer, J., Sequential self-folding of polymer sheets. *Science Advances* **2017,** *3* (3), e1602417.
37.Sharon, E.; Efrati, E., The mechanics of non-Euclidean plates. *Soft Matter* **2010,** *6* (22), 5693-5704.
38. O'Neill, B., *Elementary Differential Geometry*. Academic Press, New York: 1997.
39.do Carmo, M. P., *Differential Geometry of Curves and Surfaces*. Dover Publications, New York: 2016.
40.Gladman, A. S.; Matsumoto, E. A.; Nuzzo, R. G.; Mahadevan, L.; Lewis, J. A., Biomimetic 4D printing. *Nat. Mater.* **2016,** *15* (4), 413-418.
41.Forterre, Y.; Skotheim, J. M.; Dumais, J.; Mahadevan, L., How the Venus flytrap snaps. *Nature* **2005,** *433* (7024), 421-425.
42.Goriely, A.; Ben Amar, M., Differential Growth and Instability in Elastic Shells. *Phys. Rev. Lett.* **2005,** *94* (19), 198103.
43.Dervaux, J.; Ben Amar, M., Morphogenesis of Growing Soft Tissues. *Phys. Rev. Lett.* **2008,** *101* (6), 068101.
44.Liang, H.; Mahadevan, L., Growth, geometry, and mechanics of a blooming lily. *Proc. Natl. Acad. Sci. U. S. A.* **2011,** *108* (14), 5516-5521.
45.Studart, A. R., Biologically Inspired Dynamic Material Systems. *Angew. Chem., Int. Ed.* **2015,** *54* (11), 3400-3416.
46.Käpylä, E.; Delgado, S. M.; Kasko, A. M., Shape-Changing Photodegradable Hydrogels for Dynamic 3D Cell Culture. *ACS Appl. Mater. Interfaces* **2016,** *8* (28), 17885-17893.
47.Nawroth, J. C.; Lee, H.; Feinberg, A. W.; Ripplinger, C. M.; McCain, M. L.; Grosberg, A.; Dabiri, J. O.; Parker, K. K., A tissue-engineered jellyfish with biomimetic propulsion. *Nat. Biotechnol.* **2012,** *30* (8), 792-797.
48.Roche, E. T.; Horvath, M. A.; Wamala, I.; Alazmani, A.; Song, S.-E.; Whyte, W.; Machaidze, Z.; Payne, C. J.; Weaver, J. C.; Fishbein, G.; Kuebler, J.; Vasilyev, N. V.; Mooney, D. J.; Pigula, F. A.; Walsh, C. J., Soft robotic sleeve supports heart function. *Sci. Transl. Med.* **2017,** *9* (373).
49.Ko, H.; Javey, A., Smart actuators and adhesives for reconfigurable matter. *Accounts of chemical research* **2017,** *50* (4), 691-702.
50.Ionov, L., Biomimetic Hydrogel-Based Actuating Systems. *Adv. Funct. Mater.* **2013,** *23* (36), 4555-4570.
51.van Rees, W. M.; Vouga, E.; Mahadevan, L., Growth patterns for shape-shifting elastic bilayers. *Proc. Natl. Acad. Sci. U. S. A.* **2017,** *114* (44), 11597-11602.
52.Karzbrun, E.; Kshirsagar, A.; Cohen, S. R.; Hanna, J. H.; Reiner, O., Human brain organoids on a chip reveal the physics of folding. *Nature physics* **2018,** *14* (5), 515-522.
53.Tozluoğlu, M.; Duda, M.; Kirkland, N. J.; Barrientos, R.; Burden, J. J.; Muñoz, J. J.; Mao, Y., Planar Differential Growth Rates Initiate Precise Fold Positions in Complex Epithelia. *Developmental cell* **2019,** *51* (3), 299-312. e4.
54.Kim, S.; Laschi, C.; Trimmer, B., Soft robotics: a bioinspired evolution in robotics. *Trends Biotechnol.* **2013,** *31* (5), 287-294.
55.Rus, D.; Tolley, M. T., Design, fabrication and control of soft robots. *Nature* **2015,** *521* (7553), 467-475.

56.Na, J.-H.; Bende, N. P.; Bae, J.; Santangelo, C. D.; Hayward, R. C., Grayscale gel lithography for programmed buckling of non-Euclidean hydrogel plates. *Soft Matter* **2016,** *12* (22), 4985-4990.
57.Klein, Y.; Venkataramani, S.; Sharon, E., Experimental study of shape transitions and energy scaling in thin non-Euclidean plates. *Physical review letters* **2011,** *106* (11), 118303.
58.Dias, M. A.; Hanna, J. A.; Santangelo, C. D., Programmed buckling by controlled lateral swelling in a thin elastic sheet. *Physical Review E* **2011,** *84* (3), 036603.
59.Efrati, E.; Sharon, E.; Kupferman, R., Elastic theory of unconstrained non-Euclidean plates. *Journal of the Mechanics and Physics of Solids* **2009,** *57* (4), 762-775.
60.Al Mosleh, S.; Santangelo, C., Nonlinear mechanics of rigidifying curves. *Physical Review E* **2017,** *96* (1), 013003.
61.Huang, L.; Jiang, R.; Wu, J.; Song, J.; Bai, H.; Li, B.; Zhao, Q.; Xie, T., Ultrafast digital printing toward 4D shape changing materials. *Advanced Materials* **2017,** *29* (7).
62.Boley, J. W.; van Rees, W. M.; Lissandrello, C.; Horenstein, M. N.; Truby, R. L.; Kotikian, A.; Lewis, J. A.; Mahadevan, L., Shape-shifting structured lattices via multimaterial 4D printing. *Proceedings of the National Academy of Sciences* **2019,** *116* (42), 20856-20862.
63.Pikul, J.; Li, S.; Bai, H.; Hanlon, R.; Cohen, I.; Shepherd, R., Stretchable surfaces with programmable 3D texture morphing for synthetic camouflaging skins. *Science* **2017,** *358* (6360), 210-214.
64. Siéfert, E.; Reyssat, E.; Bico, J.; Roman, B., Bio-inspired pneumatic shape-morphing elastomers. *Nature materials* **2018**, 1.
65.Nojoomi, A.; Arslan, H.; Lee, K.; Yum, K., Bioinspired 3D structures with programmable morphologies and motions. *Nature communications* **2018,** *9* (1), 3705.

CHAPTER 2

2.1 BIOINSPIRED 3D STRUCTURES WITH PROGRAMMABLE MORPHOLOGIES

Amirali Nojoomi, Hakan Arslan, Kwan Lee & Kyungsuk Yum

Nature Communications, 9, 3705 (2018)[1]

DOI: 10.1038/s41467-018-05569-8

Publication Date (Web): Sep 12, 2018

[1] Used with permission of the publisher, 2020

2.2 ABSTRACT

Living organisms use spatially controlled expansion and contraction of soft tissues to achieve complex three-dimensional (3D) morphologies and movements and thereby functions. However, replicating such features in man-made materials remains a challenge. Here we report an approach that encodes 2D hydrogels with spatially and temporally controlled growth (expansion and contraction) to create 3D structures with programmed morphologies and motions. This approach uses temperature-responsive hydrogels with locally programmable degrees and rates of swelling and shrinking. This method simultaneously prints multiple 3D structures with custom designs from a single precursor in a one-step process within 60 s. We suggest simple yet versatile design rules for creating complex 3D structures and a theoretical model for predicting their motions. We reveal that the spatially nonuniform rates of swelling and shrinking of growth-induced 3D structures determine their dynamic shape changes. We demonstrate shape-morphing 3D structures with diverse morphologies, including bioinspired structures with programmed sequential motions.

2.3 INTRODUCTION

Nature has inspired researchers to develop shape-morphing materials that can replicate the functions of native soft tissues[1-2]. Such materials have applications in soft robotics, programmable matter, bioinspired engineering, and biomimetic manufacturing[1-12]. Existing approaches use swellable hydrogels[3-8, 13], shape-memory polymers[14-15], and liquid crystalline elastomers[16-18] with fabrication methods, such as photopatterning[4, 6-8, 11], self-folding[7, 11, 19-20], and three-dimensional (3D) printing[5, 15]. These approaches have been used to build various self-shaping 3D structures, including those with complex 3D morphologies of living organisms[4-5], but reproducing their movements has not been fully achieved[1-2, 21].

A promising approach in this regard is to use spatially controlled in-plane growth (expansion and contraction) of hydrogel sheets to form 3D structures via out-of-plane deformation (non-Euclidean plates)[3-4]. Because bending is energetically less expensive than stretching in a thin sheet, the internal stresses developed by nonuniform in-plane growth are released by out-of-plane deformation[3-4]. This approach defines 3D shapes with Gaussian curvatures[22-23] and is uniquely capable of creating 3D structures with curved geometries, often seen in biological organisms but difficult to achieve by other methods[4-5]. Living organisms, ranging from plants to marine invertebrates, use such approaches (e.g., differential growth) for fundamental biological processes, including morphogenesis, complex growth and movement, and adaptation to environments[3-5, 13, 24-34]. With the physical properties of hydrogels similar to those of soft tissues[7, 12, 33], this approach thus has great potential for creating bioinspired 3D structures[4]. In particular, the ability to spatially and temporally control the local in-plane growth could offer a new strategy to create dynamic 3D structures that can mimic the continuously deforming motions of living organisms.[1-2] However,

dynamic growth-induced 3D motions of non-Euclidean plates remains largely unexplored[3-4]. Previous theoretical and experimental studies have mainly focused on the formation of 3D shapes at equilibrium states[3-4, 35-37], but their dynamic behavior at metastable states during shape transition is not well understood. Furthermore, the principle has been demonstrated for various 3D shapes,[3-4, 37] but achieving nonaxisymmetric 3D structures with complex morphologies remains to be further studied[34-36].

In this chapter, we introduce an approach named digital light 4D printing (DL4P) that creates dynamic 3D structures with programmed morphologies and motions (Figure 2-1a). This approach encodes temperature-responsive 2D hydrogels with spatially and temporally controlled growth (expansion and contraction) functions Ω, or target metrics, which transforms the hydrogels into prescribed 3D structures and programs their motions. Previous studies of differential growth-induced 3D shaping have mostly formed single 3D shapes either at the swelled or the shrunk state[3-4, 38-39]. In contrast, our temperature-responsive hydrogels with phototunable degrees and rates of swelling and shrinking allow us to define target 3D shapes at both the swelled and shrunk states. In particular, the ability to control the rates uniquely enables a new strategy for programming growth-induced 3D motions. This method simultaneously prints multiple 3D structures with custom design (using digital light projection grayscale lithography) from a single precursor solution in a one-step process within 60 s and is thus highly scalable. Taking advantage of our phototunable hydrogels and the flexible 2D printing method for 3D material programming (e.g., without the need for multiple physical masks or nozzles), we established simple yet versatile design rules and the concept of modularity for creating complex 3D structures with diverse morphologies [4], including ray-inspired structures with programmed motions. To investigate the

dynamic growth-induced motions, we introduced a concept of dynamic target metrics and developed a dynamic theoretical model based on the concept. Our experimental and theoretical studies reveal that the spatially nonuniform rates of swelling and shrinking of growth-induced 3D structures determine their dynamic shape changes. Furthermore, the swelling and shrinking rates of our hydrogels are phototunable and thus locally programmable. The ability to spatially control the rates of shape changes allows us to fabricate dynamic 3D structures with programmed sequential motions, as previously demonstrated with photopatterned hydrogels responsive to different molecular inputs (e.g., DNA molecules with different sequences) and those with different thicknesses [40]. Such ability is critical for implementing complex functions but challenging to attain with global external stimuli (e.g., temperature). This work introduces a 3D fabrication method with the advantages of traditional (scalable) and additive (customizable) manufacturing for fabricating soft devices with programmed 3D morphologies and motions.

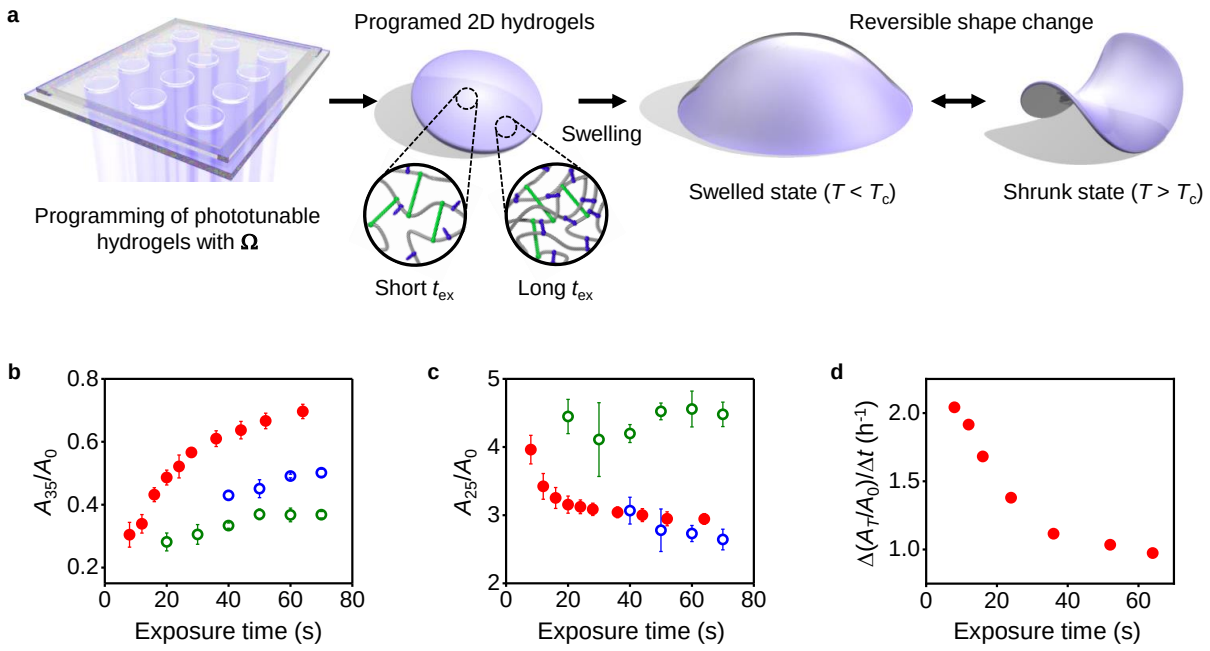

Figure 2-1 **Programming of phototunable hydrogels to create 3D structures**. **a** Digital light 4D printing process. The hydrogels are encoded with a growth function (or target metric) Ω using digital light projection grayscale lithography. The created 3D structures undergo a reversible shape transition at volume phase transition temperature Tc (~32.5 °C). T is temperature. The insets illustrate the polymer networks of the hydrogels at the early (short light exposure time t_{ex}) and late (long t_{ex}) stages of photo-polymerization, where gray, blue, and green structures represent pNIPAm, BIS, and PEGDA, respectively. **b, c** Areal shrinking (**b**) and swelling (**c**) ratios of dual- (red circles), BIS- (blue open circles), and PEGDA (green open circles)-crosslinked pNIPAm hydrogels as a function of t_{ex}. A_{35} and A_{25} are the areas of hydrogels at 25 °C and 35 °C, respectively. A_0 is the area of as-prepared hydrogels. Error bars: s.d. of three independent measurements. **d** Areal swelling rates $\Delta(A_T/A_0)/\Delta t$ of dual-crosslinked pNIPAm hydrogels as a function of tex. A_T is the area of hydrogels. t is time

2.4 RESULTS

2.4.1 Hydrogels with phototunable material properties

Our DL4P approach relies on the ability to prepare temperature-responsive hydrogels with continuously varying compositions and thus material properties (e.g., degrees and rates of swelling

and shrinking) from a single precursor solution through photo-polymerization and crosslinking within 60 s (Figure 2-1). The modulation of the material properties is based on the temporal control of polymerization and crosslinking reactions using two types of crosslinkers with different lengths by light exposure time tex. The phototunability provides a flexible means to encode the hydrogels with spatially and temporally controlled growth (swelling and shrinking), which can be used to program the formation of 3D structures and their motions.

The precursor solution consists of *N*-isopropylacrylamide (NIPAm), *N*,*N*′-methylene bisacrylamide (BIS; short-chain crosslinker), and poly(ethylene glycol) diacrylate (PEGDA; long-chain crosslinker). For an equimolar concentration of crosslinkers, crosslinking with PEGDA forms gels faster than with BIS, due to longer distances between the crosslinking points of PEGDA (Figure 2-2, Figure 2-3) [41]. The BIS- and PEGDA-crosslinked hydrogels swell and shrink in different degrees (Figure 2-1**b**, **c**, Figure 2-2).

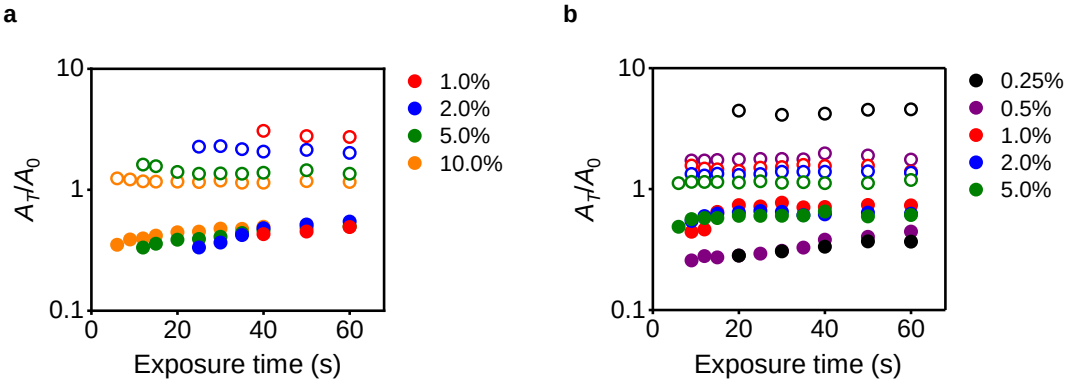

Figure 2-2 **Areal swelling and shrinking ratios of pNIPAm hydrogels crosslinked with single crosslinkers (BIS and PEGDA). a** Areal swelling and shrinking ratios (AT/A0) of pNIPAm hydrogels crosslinked with BIS as a function of light exposure time. The hydrogels were prepared with BIS of 1.0 to 10.0 mol% of NIPAm in precursor solutions (as indicated in the legend). **b** Areal swelling and shrinking ratios (AT/A0) of pNIPAm hydrogels crosslinked with PEGDA as a function of light exposure time. The hydrogels were prepared with PEGDA of 0.25 to 5.0 mol% of NIPAm in precursor solutions (as indicated in the legend). The open and closed circles represent the swelling and shrinking ratios, respectively. The black, purple, red, blue, green, and orange

circles represent AT/A0 of pNIPAm hydrogels crosslinked with crosslinkers (BIS and PEGDA) of 0.25, 0.5, 1.0, 2.0, 5.0, and 10.0 mol% of NIPAm in precursor solutions, respectively, as indicated in the legends. The results show that assuming the same kinetics of polymerization of NIPAm monomers with BIS and PEGDA, pNIPAm hydrogels crosslinked with long-chain crosslinkers (PEGDA) are formed at a lower monomer conversion (thus, lower network density at the gel point) than those crosslinked with short-chain crosslinkers (BIS).

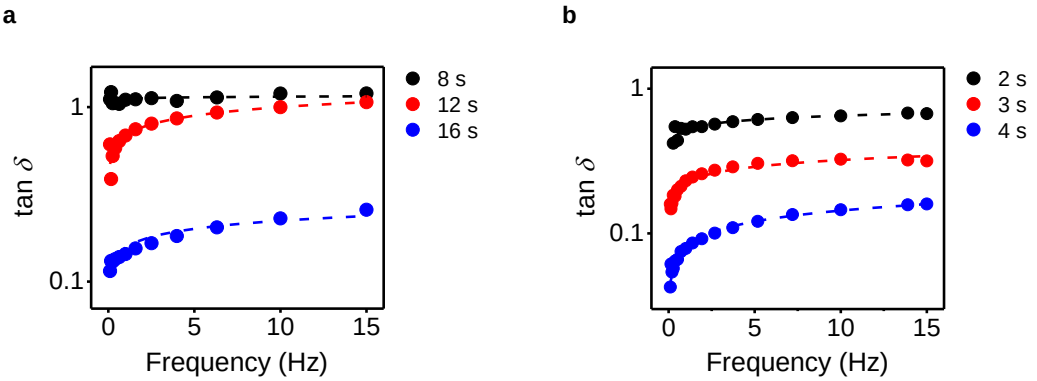

Figure 2-3 **Measurements of the gel points of pNIPAm hydrogels crosslinked with single crosslinkers (BIS and PEGDA). a** $\tan\delta$ of pNIPAm hydrogels crosslinked with BIS as a function of frequency. The black, red, and blue circles represent $\tan\delta$ of pNIPAm hydrogels prepared by light exposure times of 8, 12, and 16 s, respectively. **b** $\tan\delta$ of pNIPAm hydrogels crosslinked with PEGDA as a function of frequency. The black, red, and blue circles represent $\tan\delta$ of pNIPAm hydrogels prepared by light exposure times of 2, 3, and 4 s, respectively. At the gel point, $\tan\delta = G''/G'$ has a constant value over the frequency sweep, where G' and G'' are the shear storage modulus and shear loss modulus, respectively[42-43]. The measurements show that the prepolymer solutions with BIS and PEGDA form gels with light exposure times of around 8 s and less than 2 s, respectively.

Based on these results, we hypothesized that poly(*N*-isopropylacrylamide) (pNIPAm) hydrogels crosslinked with both BIS and PEGDA have a larger phototunable range of swelling and shrinkage over a wider range of t_{ex} than those crosslinked with single crosslinkers. The dual

crosslinking indeed increases the phototunable range of shrinking and swelling and the range of t_{ex} that can be used to tune the shrinking and swelling ratios (Figure 2-1**b**, **c**, Figure 2-4).

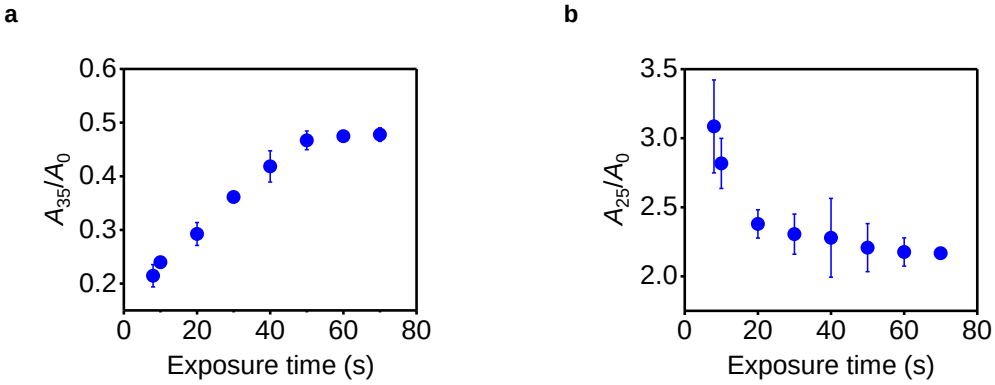

Figure 2-4 **Areal shrinking and swelling ratios of pNIPAm hydrogels crosslinked with both BIS and PEGDA. a** Areal shrinking ratio (A_{35}/A_0) of pNIPAm hydrogels crosslinked with both BIS and PEGDA as a function of light exposure time. **b** Areal swelling ratio (A_{25}/A_0) of pNIPAm hydrogels crosslinked with both BIS and PEGDA as a function of light exposure time. The hydrogels were prepared with precursor solutions of NIPAm (0.2 g), BIS (0.5 mol% of NIPAm), PEGDA (0.25 mol% of NIPAm), and PBPO (0.3 mol% of NIPAm) in 1 mL aqueous solution (1:3 ratio of water and acetone by volume). The precursor solutions contain the same amount of BIS, PEGDA, and PBPO but 50 wt% of NIPAm in the precursor solutions used in Figure 2-1b, c. Error bars: s.d. of three independent measurements.

More interestingly, the swelling and shrinking rates of our hydrogels are also phototunable (Figure 2-1**d**). We reason that crosslinking with long-chain crosslinkers (PEGDA) forms a low density hydrogel framework at an early stage (low monomer conversion), whereas the conversion of monomers to polymers and their crosslinking via short-chain crosslinkers (BIS) continuously occurs within the hydrogel framework throughout the time course of photo-polymerization, increasing the density of the polymer networks (Figure 2-1**a**). Moreover, crosslinking via PEGDA is expected to be suppressed at the late stage, because of diffusional limitations in high-density polymer networks[41]. We verified this mechanism by measuring the density of the polymer networks as a function of t_{ex}. The density increases with t_{ex} (Figure 2-5**a**). The increase in the

density in turn reduces the degrees and rates of macroscopic swelling and shrinking (Figure 2-1**b**–**d**, Figure 2-5**b**, **c**). This mechanism differs from previous ones that control the crosslink density by light irradiation dose, which, for example, tunes only the swelling of pNIPAm hydrogels[4]. In contrast to photoinduced controlled/living radical polymerization (photo-CRP), which precisely controls the molecular architecture of polymers, such as molecular weights and compositions,[44-47] our approach modulates only the overall density of polymer networks (rather than the molecular weight of individual polymer chains).

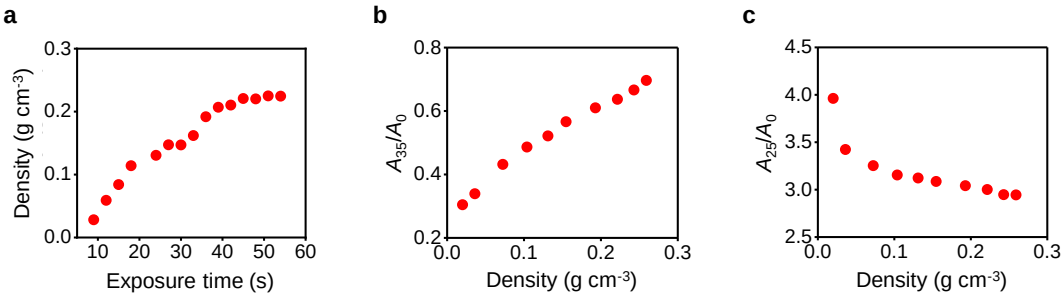

Figure 2-5 Density of pNIPAm hydrogels. **a** The density of pNIPAm hydrogels crosslinked with BIS and PEGDA by different light exposure times was measured. The density of the pNIPAm hydrogels increases with light exposure time. The density was calculated using their dry mass and the volume of as-prepared hydrogels after washing with acetone and IPA. **b** Areal shrinking ratio (A_{35}/A_0) as a function of density. A_{35}/A_0 increases with the density of the hydrogels, showing that the degree of shrinking decreases with the density of the hydrogels. **c** Areal swelling ratio (A_{25}/A_0) as a function of density. A_{25}/A_0 decreases with the density of the hydrogels, showing that the degree of swelling decreases with the density of the hydrogels.

2.4.2 Mathematical theory for 3D shaping

Our theoretical model for making growth function, **Ω,** required to make 3D shapes is based on the theory of differential geometry of surfaces[22-23] and the concept of target metrics (non-Euclidean plates)[3, 48]. A differential growth (swelling or shrinking)-induced 3D shape (surface) adopts an isotropic embedding of a target metric[3-4, 48]. The metric encodes the local equilibrium

distances between points on the 3D shape (surface)[3, 22-23, 48]. Because bending ($E_B \sim {t_h}^3$, where t_h is the thickness of a sheet) is energetically less costly than stretching ($E_S \sim t_h$) in a thin sheet, the internal stresses developed by nonuniform in-plane growth are released by out-of-plane bending deformation ($E_B < E_S$)[3-4, 48]. As the thickness of the sheet decreases, the shape converges to the embedding of the lowest bending energy[3-4, 48].

We consider a 3D shape (suface) with a parameterization[22-23]

$$\mathbf{x}(u,v) = (x_1(u,v), x_2(u,v), x_3(u,v)) \tag{1}$$

where (u,v) are points on the 2D plane. The square of the element of arc length, or the distance between neighboring points, in the 3D surface is given by the first fundamental form (or the metric)

$$ds^2 = Edu^2 + 2Fdudv + Gdv^2 \tag{2}$$

where E, F, and G are the coefficients of the first fundamental form[22-23]. We assume that a spatially-controlled in-plane growth (swelling or shrinking) of a 2D plane in a coordinate system (u', v') can induce the formation of the 3D shape via out-of-plane deformation[3, 48]. The square of the distance between points on the 2D plane before deformation is

$$dl^2 = \mathbf{g}du'dv' \tag{3}$$

where $\mathbf{g}$ is the metric (or first fundamental form) of the 2D plane before deformation[48]. The spatially controlled growth determines new equilibrium distances between points on the 2D plane. The information of the new distances is contained in a new metric $\bar{\mathbf{g}}$. To form the 3D shape with the growth, the new metric of the 2D plane should be the same as that of the 3D shape:

$$ds^2 = \bar{\mathbf{g}}du'dv' \tag{4}$$

We define the new metric $\bar{\mathbf{g}}$ as the target metric[3, 48]. If the target metric (or the parameterization) is isothermal (or conformal), which is the case of our material systems ($E = G$ and $F = 0$), we can write the target metric with scale function λ

$$\bar{\mathbf{g}} = \lambda^2 \mathbf{g} \tag{5}$$

We define $\boldsymbol{\Omega} = \bar{\mathbf{g}}$ as our target metric and λ^2 (or Ω) as our areal growth function[22-23]. $\boldsymbol{\Omega}$ contains all the information about how to encode a 2D plane with spatially controlled growth (swelling or shrinking) to form the target 3D shape. According to Gauss's *theorema egregium*, Gaussian curvature is then

$$K = -\Delta(\ln\lambda)/\lambda^2 = -\Delta(\ln\Omega)/(2\Omega) \tag{6}$$

where Δ is the Laplacian[22-23].

2.4.2.1 Theoretical model for axisymmetric 3D structures

Things greatly simplify if there is an axis symmetry. We consider an axisymmetric 3D shape (surface of revolution) in a cylindrical coordinate system (ρ, φ, z), where the z axis is the axis of symmetry (axis of rotation) and $z = f(\rho)$. Then, we get the square of the element of arc length on the 3D shape from Equation 2: $ds^2 = \left(1 + {f_\rho}^2\right)d\rho^2 + \rho^2 d\varphi^2$, where $f_\rho = df/d\rho$[22-23]. We assume that we can induce the 3D shape by encoding a 2D plane with Ω in a polar corodinate system (r, θ). Then, we get the following equation from Equation 4:

$$\left(1 + {f_\rho}^2\right)d\rho^2 + \rho^2 d\varphi^2 = \Omega(r)(dr^2 + r^2 d\theta^2) \tag{7}$$

The left side of Equation 7 represents the distance between two neighboring points on the 3D shape, whereas the right side represents the distance between neighboring points on the 2D plane after growth (swelling or shrinking). In other words, Equation 7 describes how the spatially-controlled growth of the 2D plane (right side) induces the 3D shape (left side). Because the growth is axisymmetric, we assume that the angle between neighboring points on the 2D plane does not change during growth and thus obtain $d\varphi = d\theta$ and $\rho^2 d\varphi^2 = \Omega(r) r^2 d\theta^2$. Then, Equation 7 gives:

$$\rho^2 = \Omega(r) r^2 \tag{8}$$

$$\left(1 + {f_\rho}^2\right) d\rho^2 = \Omega(r) dr^2 \tag{9}$$

For a given axisymmetric 3D shape, we can thus determine the relationship of r and ρ and that of Ω and ρ. For a given Ω, we can predict the 3D shape that adopts Ω using Equations 8 and 9.

2.4.2.2 Determination of the growth function (Ω) for a target 3D structure

We determine Ω for a spherical cap. A spherical cap with a radius of r_0 is given by

$$\rho^2 + (z - z_0)^2 = {r_0}^2 \tag{10}$$

where z_0 is a constant. We can then get ρ and Ω as a function of r using Equations 8, 9, and 10

$$\rho = \frac{2r_0(r/R)}{1 + (r/R)^2} \tag{11}$$

$$\Omega = \frac{c}{(1 + (r/R)^2)^2} \tag{12}$$

where R and $c = 4(r_0/R)^2$ are constants. We can obtain local Gaussian curvature $K = 1/{r_0}^2 = 4/(cR^2)$ using Equations 6 and 12.

We next determine Ω for a cone structure. A cone with a vertex angle of 2β is given by

$$z - z_0 = \rho \cot \beta \tag{13}$$

We then can get ρ and Ω as a function of r using Equations 8, 9, and 13

$$\rho = \rho_0 \left(\frac{r}{R}\right)^{\alpha} \tag{14}$$

where R is a constant and exponent $\alpha = \sin\beta$, and

$$\Omega = c \left(\frac{r}{\mathrm{R}}\right)^{2(\alpha-1)} \tag{15}$$

where $c = (\rho_0/R)^2$. We can obtain $K = 0$ using Equations 6 and 15.

For a saddle shape, we used

$$\Omega = \frac{c}{(1 - (r/R)^2)^2} \tag{16}$$

We can then obtain $K = -4/(cR^2)$ using Equations 6 and 16.

2.4.2.3 Prediction of a 3D shape from a growth function (Ω)

We demonstrate the prediction of 3D shapes using a growth function in the form

$$\Omega(r) = c \left[1 + \left(\frac{r}{R'}\right)^2\right]^{\alpha-1} \tag{17}$$

where $R' = aR$ and a and α are constants. The constant a is included to make Ω with different α have the same maximum and minimum values ($\Omega_{\max}$ and $\Omega_{\min}$) in $0 < r/R < 1$. We used the experimentally accessible maximum and minimum values of A_{35}/A_0 (Figure 2-1**b**) as $\Omega_{\max}$ and $\Omega_{\min}$. We predicted 3D shapes using Equations 8, 9, and 17 as a function of $\xi = r/R$

$$z(\xi) = \frac{{}_2F_1}{3(1+\alpha)\xi}\left[\frac{(1+\alpha)(a^2+\xi^2)}{a^2(-1+\alpha)}\right]^{\frac{3-\alpha}{2}}[2a^2+(1+a)\xi^2] \quad (18)$$
$$\sqrt{-\frac{1}{(a^2+\xi^2)^3}\left[a^2c^2(-1+\alpha)\xi^2\left(1+\frac{\xi^2}{a^2}\right)^{\alpha}(2a^2+(1+\alpha)\xi^2)\right]}$$

where ${}_2F_1$ is a hypergeometric function ${}_2F_1 = \left[\frac{3}{2}, \frac{3-\alpha}{2}; \frac{5}{2}; -\frac{2a^2+(1+\alpha)\xi^2}{a^2(-1+\alpha)}\right]$. We constructed the theoretical 3D shapes and K as a function ρ, in which $\xi = r/R$ in Equation 18 was converted to ρ using Equation 8. We used Mathematica (Wolfram) and MATLAB for the calculations. We calculated the theoretical values of the base angle γ

$$tan(\gamma) = \frac{(a^2+\xi^2)(1+\xi^2/a^2)^{(1-\alpha)/2}}{c(a^2+\alpha\xi^2)}\sqrt{-\frac{a^2c^2(-1+\alpha)\xi^2(1+\xi^2/a^2)^{\alpha}[2a^2+(1+\alpha)\xi^2]}{(a^2+\xi^2)^3}} \quad (19)$$

2.4.3 Shape-morphing 3D structures with axisymmetric metrics

To validate our DL4P approach and demonstrate its accuracy, we created well-defined geometric 3D structures with axisymmetric metrics (Figure 2-6**a**–**k**). In contrast to previous studies, which mostly form 3D shapes at either the swelled or the shrunk state[3-5], our approach can define the target 3D shapes at both the swelled ($\boldsymbol{\Omega} > 1$) and the shrunk ($\boldsymbol{\Omega} < 1$) states. The

equilibrium 3D shape is selected from the competition between bending ($E_B \sim {t_h}^3$, where t_h is the thickness of a sheet) and stretching ($E_S \sim t_h$) energies[3, 48]. As the thickness decreases, the hydrogel sheet thus converges to the stretch-free configuration that fully follows the target metric[48]. However, the actual metric adopted by experimental 3D structures differs from the target metric, because of a finite-thickness bending energy[36, 48]. The structure at the shrunk state can thus yield a 3D shape closer to the theoretical configuration described by the target metric than one at the swelled state. In addition, the use of hydrogels at the shrunk state is beneficial for practical applications, for example, because of their enhanced mechanical properties and the formation of target shapes under physiological conditions ($T = 37$ °C) for potential biomedical applications[49]. We thus designed $\boldsymbol{\Omega}$ for target shapes at the shrunk state.

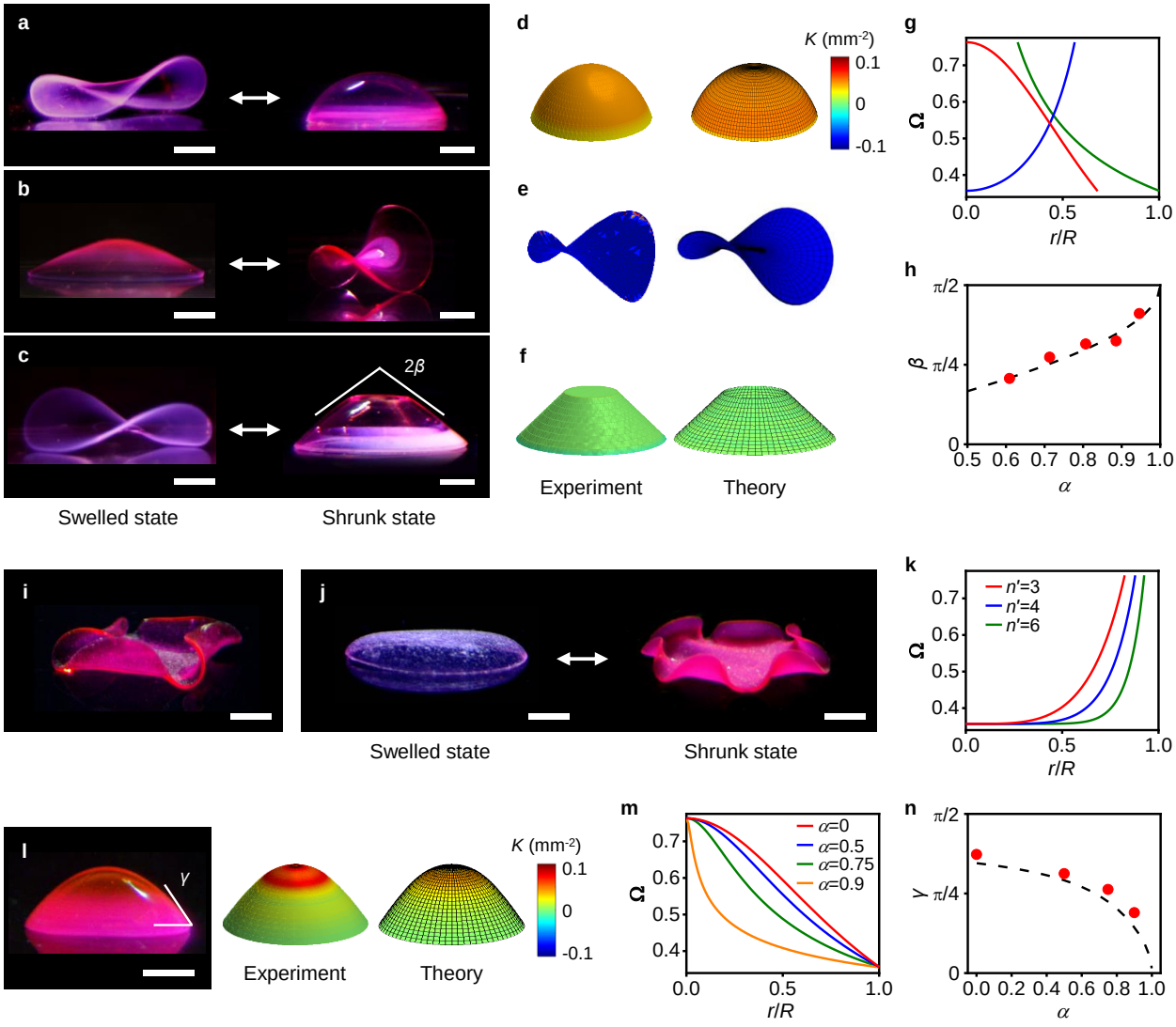

Figure 2-6 **Shape-morphing 3D structures with axisymmetric metrics. a–c** 3D structures with constant Gaussian curvature K at the shrunk state (right) and the corresponding structures at the swelled state (left): spherical cap (**a**), saddle (**b**), and cone (**c**) shapes. **d–f** Reconstructed 3D images with K of experimental (left) and theoretical (right) shapes of the spherical cap (**d**), saddle (**e**), and cone (**f**) structures in **a–c**. **g** $\boldsymbol{\Omega}$ used to form the structures in **a–c**: red line (spherical cap), blue line (saddle), and green line (cone). **h** Experimental (solid circles) and theoretical (dashed line) values of β with different α in $\boldsymbol{\Omega}$ for cone structures. **i**, **j** Enneper's minimal surfaces with n' wrinkles: $n' = 4$ (**i**) and 6 (**j**). The structure reversibly transforms between prescribed 3D shapes at the swelled (left) and shrunk (right) states as shown in **j**. **k** $\boldsymbol{\Omega}$ used to form the Enneper's minimal surfaces with n' wrinkles in **i**, **j** and Figure 2-7: $\boldsymbol{\Omega}$ with $n' = 3$ (red line), $n' = 4$ (blue line), and $n' = 6$ (green line). **l** Experimentally constructed 3D structure with a smooth gradient in K (left) and reconstructed 3D images with K of the experimental (middle) and theoretical (right) structures. γ is the base angle of the structures. **m** $\boldsymbol{\Omega}$ with different α used to form the structures in **l** and

Figure 2-8: $\boldsymbol{\Omega}$ with $\alpha = 0$ (red line), $\alpha = 0.5$ (blue line), $\alpha = 0.75$ (green line), and $\alpha = 0.9$ (orange line). **n** Experimental (solid circles) and theoretical (dashed line) values of γ of the structures formed with Ω in **m** as a function of α. Scale bars, 5 mm (left), 2 mm (right) in **a–c**; 2 mm in **i**; 5 mm (left), 2 mm (right) in **j**; 2 mm in **l**.

We created spherical cap, saddle, and cone structures with constant Gaussian curvature $K > 0$, $K < 0$, and $K = 0$, respectively (Figure 2-6**a–c**, Section **2.4.2.2**). We used Equations 12, 15 and 16 to experimentally create spherical cap, a truncated cone with a vertex angle of 2β and a saddle structures at the shrunk state (Figure 2-6**a-c**). We formed these structures by encoding hydrogels (400 μm in thickness) with $\boldsymbol{\Omega}$ shown in Figure 2-6**g**. Equations 10 and 13, were used to construct theoretical 3D structure and Gaussian curvature (K) of the cap and cone structures, respectively (Figure 2-6**d,f**), while we constructed a theoretical 3D structure with constant negative K (Figure 2-6**e**) by introducing two principle curvatures $k_1 = -k_2 = 2/(\sqrt{c}R)$ into a flat surface using 3ds Max.

The resulting structures agree quantitatively with the theoretical structures, reflecting the accuracy of our approach (Figure 2-6**d–f,** Section **2.4.2.2**). For example, the experimentally measured K of the spherical cap and saddle structures are 0.0464 mm^{-2} and -0.0727 mm^{-2}, which match well with the theoretically calculated K of 0.0468 mm^{-2} and -0.0722 mm^{-2}, respectively. The cone structures constructed with different exponents α in $\boldsymbol{\Omega}$ have the programmed value of the vertex angle β ($\beta = \sin^{-1}\alpha$) (Figure 2-6**h**). We further verified our approach by creating Enneper's minimal surfaces (Figure 2-6**i, j**) using $\boldsymbol{\Omega}(r) = c[1 + (r/R)^{2(n'-1)}]^2$, where r is a radial position and c, R, and n' are constants (Figure 2-6**k**)[4]. As expected, the growth functions

with different n' induce Enneper's surfaces with the targeted number of wrinkles n' (Figure 2-6**i**–**k**, Figure 2-7).

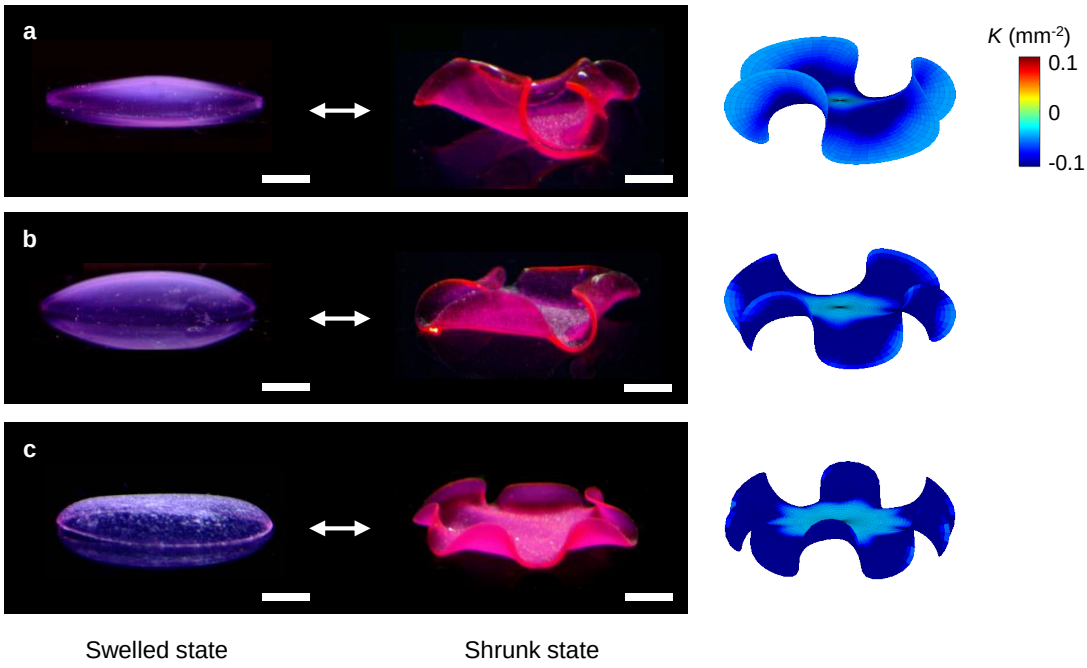

Figure 2-7 **Enneper's minimal surfaces with a different number of wrinkles.** Experimentally created Enneper's minimal surfaces with $n' = 3$ (**a**), $n' = 4$ (**b**), and $n' = 6$ (**c**) at the shrunk state (middle). The images on the left side show the corresponding 3D structures at the swelled state. The images on the right side show the theoretical shapes of Enneper's minimal surfaces with $n' = 3$, $n' = 4$, and $n' = 6$. Scale bars, 5 mm (left); 2 mm (right).

The created structures reversibly transform between prescribed 3D shapes at the swelled and shrunk states in response to temperature change (Figure 2-6**a**–**c**, **j**). The 3D structures at the swelled state adopt new metrics, determined by the areal swelling ratios (Figure 2-1**c**) and the growth functions designed for the target shapes at the shrunk state. Because of the inverse relationship between the areal swelling and shrinking ratios (Figure 2-1**b, c**), 3D shapes with $K > 0$ (e.g., spherical cap in Figure 2-6**a**, right) at the shrunk state in general transform to 3D shapes

with $K < 0$ at the swelled state (e.g., saddle-like shape in Figure 2-6a, left) and vice versa (Figure 2-6**b**).

In addition to determining $\boldsymbol{\Omega}$ for a target 3D shape (Figure 2-6**a, c**), we can predict the 3D shape for a given $\boldsymbol{\Omega}$ (Figure 2-6**l**). To validate the predictive power of the model, we considered a growth function in the form $\boldsymbol{\Omega}(r) = c[1 + (r/R')^2]^{\alpha-1}$, where $R' = aR$ and a and α are constants (Figure 2-6**l–n**, Section **2.4.2.3**). The theoretical model predicts 3D shapes that consist of a spherical cap-like shape with a smooth gradient in K in the central region and a cone-like shape ($K = 0$) in the outer region (Figure 2-6**m**). The experimental structures agree well with the theoretical predictions (Figure 2-6**l–n**, Figure 2-8). For example, the base angle γ of the experimental structures decreases with α, following the predictions (Figure 2-6**n**). We used Equation 19 to plot the theoretical values of γ as a function of α and compared them with the experimentally obtained values in Figure 2-6**n**.

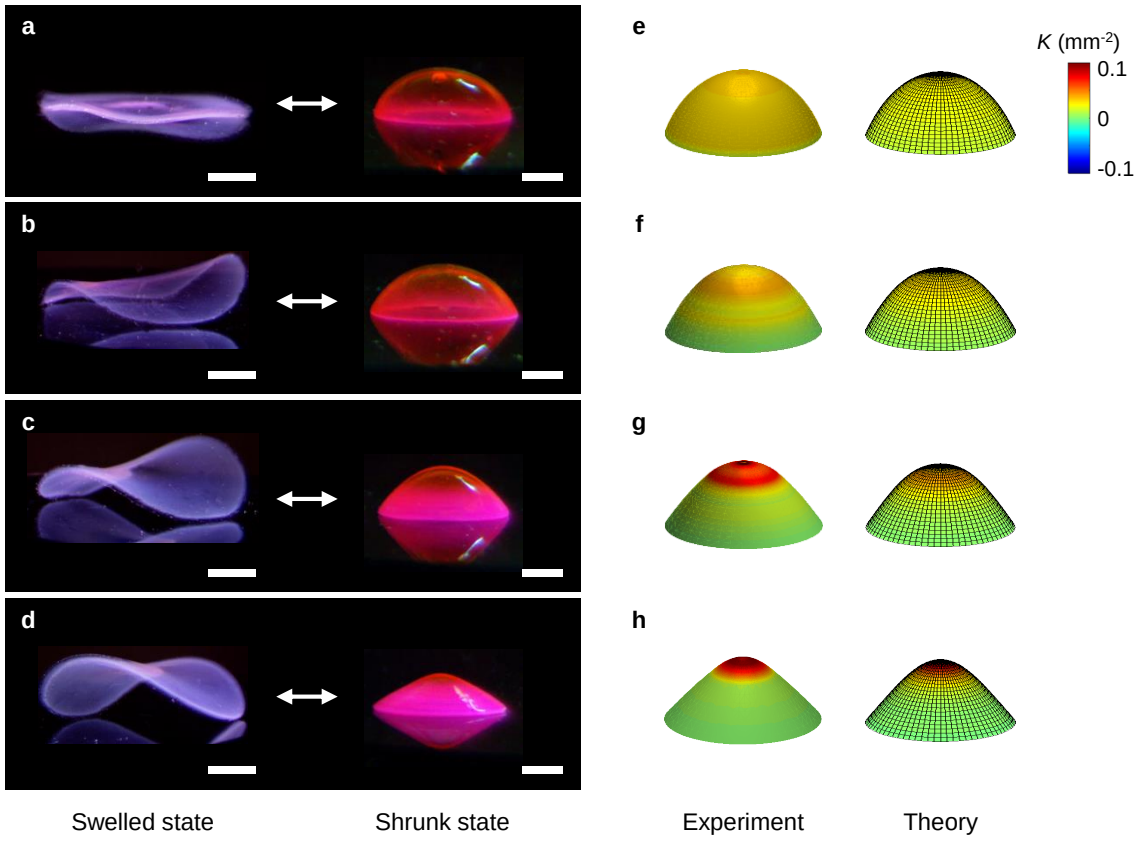

Figure 2-8 **Prediction and creation of 3D structures with a smooth gradient in Gaussian curvature K.** (**a**–**d**) The 3D structures were created with $\Omega(r) = c[1 + (r/R')^2]^{\alpha-1}$, where $R' = aR$, with $\alpha = 0$ and $a = 0.94$ (**a**), $\alpha = 0.5$ and $a = 0.53$ (**b**), $\alpha = 0.75$ and $a = 0.22$ (**c**), which is also shown in Figure 2-6l, and $\alpha = 0.9$ and $a = 0.022$ (**d**) (Figure 2-6m). Scale bars, 5 mm (left); 2 mm (right). (**e**–**h**) Reconstructed 3D images with K of experimentally created (left) and theoretically predicted (right) 3D structures shown in **a**–**d**. The 3D images of the theoretically predicted 3D structures were constructed as described in Section 2.4.2.3. The theoretical model predicts 3D shapes with a smooth gradient in K, which decreases from the maximum value to 0 with r, as shown in **e**– **h**. As compared in **e**–**h**, the experimental structures agree with the theoretical models.

The examples in Figure 2-6 to Figure 2-8 illustrate the accuracy and sensitivity of our approach. Small changes in **Ω** can induce substantial changes in the resulting 3D shapes (e.g., Figure 2-6**i–k**, Figure 2-7) [48].

2.4.4 Design rules for creating complex 3D structures

We next sought to establish design rules for creating nonaxisymmetric 3D structures with diverse morphologies (Figure 2-9). Our schemes involve the combination and transformation of target metrics and the concept of modularity. As they are implemented in the metric space, these schemes require design rules for how to interface metrics[4]. We thus introduced the concepts of linkers and transitional components at the interfaces of metrics.

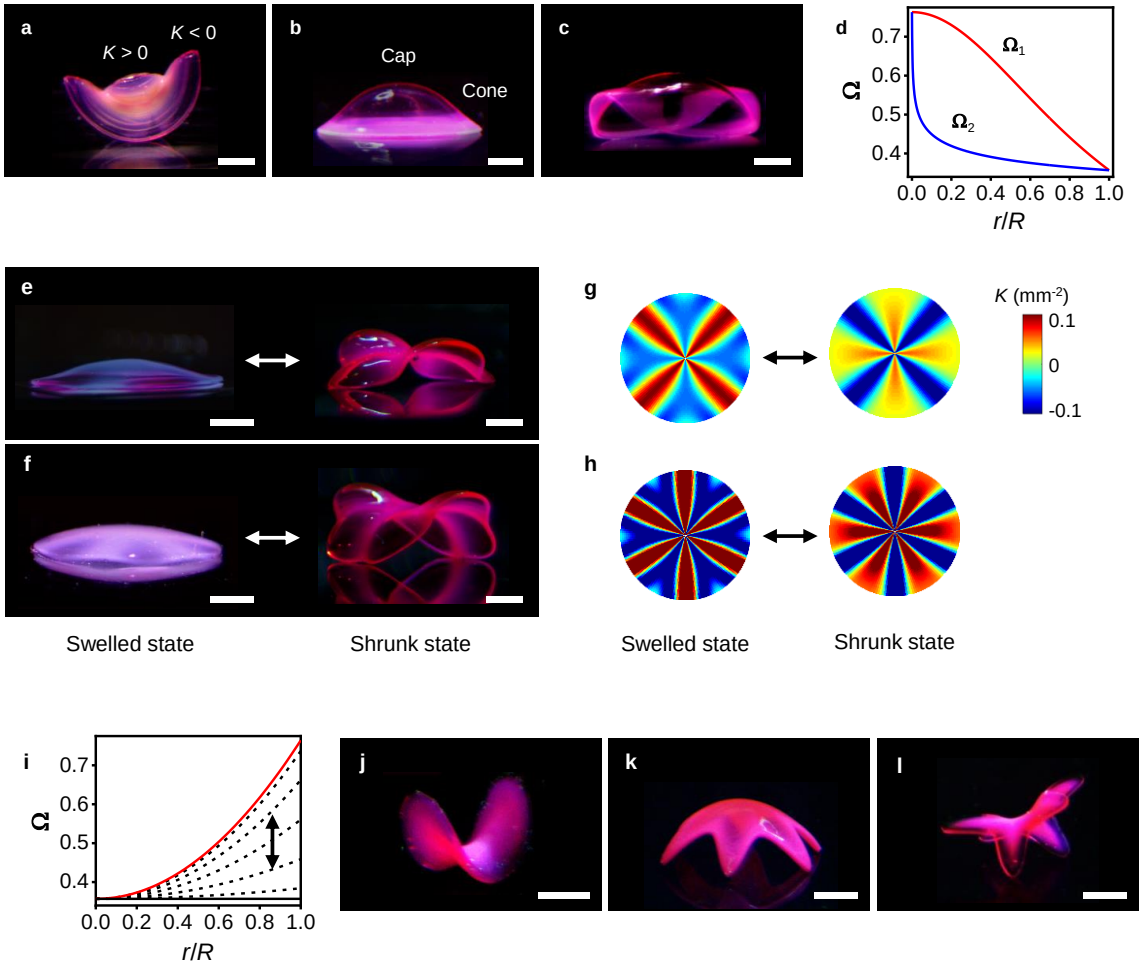

Figure 2-9 **Nonaxisymmetric 3D structures with morphological diversity. a–c**, Hybrid 3D structures with radially (**a**, **b**) and azimuthally (**c**) combined **Ω**. **d** **Ω** used to create the 3D structures in **c**: $\mathbf{\Omega}_1$ (red line), $\mathbf{\Omega}_2$ (blue line). **e**, **f** 3D structures with alternating $K > 0$ and $K < 0$ and 4 (**e**) and 6 (**f**) nodes along θ. **g**, **h** Theoretically calculated Gaussian curvature K of the structures with 4 (**g**) and 6 (**h**) nodes shown in **e**, **f** at the swelled (left) and shrunk (right) states. **i** **Ω** used to form the structures in **e**, **f**. The red line, black line, and dashed black lines indicate **Ω** at $\theta = 0$ and $(l\pi)/L$ (maximum **Ω**), $\theta = (2l-1)\pi/(2L)$ (minimum **Ω**), and θ between the maximum and minimum of **Ω**, where l and L are constants. l is a positive integer. **j** Elongated elliptical saddle structure with an aspect ratio of 2 ($b = 0.5$). **k** Spherical cap with 6 legs ($b = 0.5$, $L = 3$). **l** Saddle-like structure with 6 legs ($b = 0.5$, $L = 3$). Scale bars, 2 mm in **a–c**; 5 mm (left), 2 mm (right) in **e**, **f**; 2 mm in **j–l**.

The radial and azimuthal combinations of growth functions yield hybrid 3D structures with alternating features of the functions along the r (Figure 2-9**a, b**) and θ (Figure 2-9**c**) directions, respectively. For example, the radial combination of $\boldsymbol{\Omega_1}$ for a spherical cap and $\boldsymbol{\Omega_2}$ for a saddle shape induces a structure with $K > 0$ and $K < 0$ in the central and outer regions, respectively (Figure 2-9**a**, Figure 2-10).

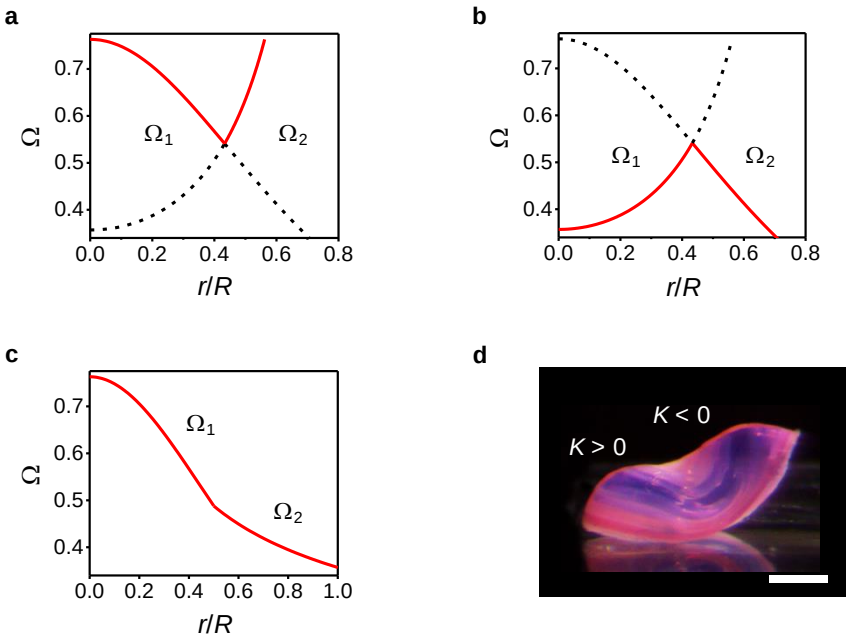

Figure 2-10 **Hybrid 3D structures with radially combined target metrics.** (**a**) Ω (red) used to form the hybrid 3D structure shown in Figure 2-9a. Ω radially combines Ω_1 (Ω for a spherical cap shown in Figure 2-6a) at $0 < r/R < 0.43$ and Ω_2 (Ω for a saddle shape shown in Figure 2-6b) at $0.43 < r/R < 0.56$. The black dashed lines show the projection of Ω_1 and Ω_2. (**b**) Ω that radially combines Ω_1 (Ω for a saddle shape shown in Figure 2-6b) at $0 < r/R < 0.43$ and Ω_2 (Ω for a spherical cap shown in Figure 2-6a) at $0.43 < r/R < 0.56$. The radially combined Ω were used to form the hybrid 3D structure shown in **d**. (**c**) Ω that radially combines Ω_1 (Ω for a spherical cap shown in Figure 2-6a) at $0 < r/R < 0.5$ and Ω_2 (Ω for a cone shape with $\alpha = 0.775$ shown in Figure 2-6c) at $0.5 < r/R < 1.0$. The radially combined Ω were used to form the hybrid 3D structure shown in Figure 2-9b. (**d**) Hybrid 3D structure generated with Ω in **b**. The hybrid structure combines the saddle shape with $K < 0$ and the spherical cap shape with $K > 0$ in the center and outer regions, respectively. Scale bar, 2 mm.

Another example is a hybrid structure that combines a spherical cap and a cone (Figure 2-9**b**). The azimuthal combination of $\boldsymbol{\Omega}_1$ ($5° < \theta < 85°$ and $185° < \theta < 265°$) and $\boldsymbol{\Omega}_2$ ($95° < \theta < 175°$ and $275° < \theta < 355°$) shown in Figure 2-9**d** yields a structure with alternating features of $\boldsymbol{\Omega}_1$ and $\boldsymbol{\Omega}_2$ along θ (Figure 2-9**c**). We introduced a linear linker with a form $\boldsymbol{\Omega}_L = (\boldsymbol{\Omega}_1 - \boldsymbol{\Omega}_2)\theta/\Delta\theta + \boldsymbol{\Omega}_2$ with $\Delta\theta = 10°$ at the interfaces of $\boldsymbol{\Omega}_1$ and $\boldsymbol{\Omega}_2$ to make $\boldsymbol{\Omega}$ continuous, as sharp discontinuities in $\boldsymbol{\Omega}$ can cause stress accumulation and thereby shape distortion (e.g., hybrid $\boldsymbol{\Omega}$ without linkers or linkers with $\theta = 5°$, Figure 2-11).

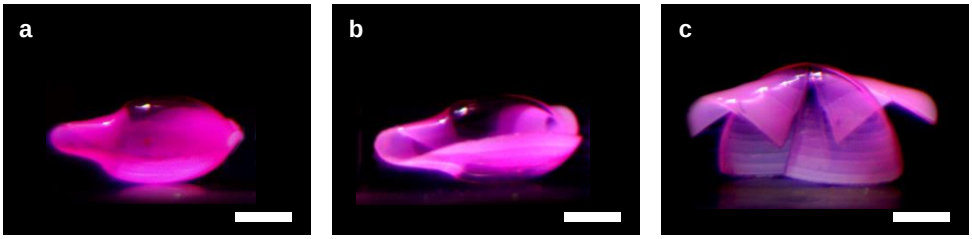

Figure 2-11 **Hybrid 3D structures with azimuthally combined target metrics.** (**a**) Hybrid 3D structure created with Ω that azimuthally combines Ω_1 and Ω_2 shown in Figure 2-9d without Ω_L. Ω_1 and Ω_2 are shown in Figure 2-6m, which have with $\alpha = 0$ and $\alpha = 0.9$, respectively. The sharp discontinuities in Ω induce stress accumulation and thus shape distortion. (**b**) Hybrid 3D structure created with Ω that azimuthally combines Ω_1 and Ω_2 (Figure 2-9**d**) with $\Omega_L = (\Omega_1 - \Omega_2)(\theta/\Delta\theta) + \Omega_2$ with $\Delta\theta = 5°$ at the interfaces. Ω that combines Ω_1 and Ω_2 using Ω_L with $\Delta\theta = 5°$ induces shape distortion, because of sharp changes at the interfaces. (**c**) Hybrid 3D structure created with Ω that azimuthally combines Ω_1 and Ω_2 shown in Figure 2-9**d** without Ω_L but with space $\Delta\theta = 5°$ at the interfaces of Ω_1 and Ω_2. The hybrid structure shows the key signatures of the structures induced by Ω_1 and Ω_2 along the θ direction (Figure 2-8**a, d**). Ω_1 yields a spherical cap-like shape (Figure 2-8a), whereas Ω_2 yields a shape that combines a spherical cap-like shape in the center and a cone-like shape with a large vertex angle in the edge (Figure 2-8d). Scale bars, 2 mm.

Transforming axisymmetric $\boldsymbol{\Omega}$ into a function of θ in the form $\boldsymbol{\Omega}(r,\theta) = c(\theta)\boldsymbol{\Omega}(r/(a(\theta)R))$ leads to nonaxisymmetric structures with varying morphologies along θ (Figure 2-9**e**–**l**). $c(\theta)$ scales $\boldsymbol{\Omega}$ along θ. Therefore, transforming $\boldsymbol{\Omega}(r) = c(r/R)^2 + \Omega_{\min}$ for a modified excess cone (Figure 2-12)[50-51] with $c(\theta) = c_0\cos^2(L\theta)$, where $\Omega_{\min}$ and L are constants, forms a shape with alternating $K > 0$ and $K < 0$ and a programmed number of nodes $n' = 2L$ (Figure 2-9**e**–**i**, Figure 2-12). The resulting structures with 4 ($L = 2$) and 6 ($L = 3$) nodes are shown in Figure 2-9**e, f**, respectively. The structures have the same number of nodes at the swelled and shrunk states (Figure 2-9**e**–**h**). On the other hand, $a(\theta)$ in $\boldsymbol{\Omega}(r,\theta) = c\boldsymbol{\Omega}(r/(a(\theta)R))$ scales $\boldsymbol{\Omega}$ along r. This transformation defines the boundary of structures, while maintaining the functional form and thereby the shape along r. Transforming $\boldsymbol{\Omega}$ for a saddle shape with $a(\theta) = b/\sqrt{1 + (b^2 - 1)\sin^2\theta}$ thus forms an elongated elliptical saddle structure with an aspect ratio of $1/b$ ($0 < b < 1$) (Figure 2-9**j**, Figure 2-13); an elongated saddle structure with an aspect ratio of 2 ($b = 0.5$) is shown in Figure 2-9**j**. Interestingly, the directions of the principal curvatures at the center of the saddle structure align with the major and minor axes of the ellipse, suggesting that this configuration is an embedding of the lowest bending energy of the target metric. Furthermore, adding periodicity into $\boldsymbol{\Omega}$ with $a(\theta) = b/\sqrt{1 + (b^2 - 1)\sin^2 L\theta}$ modulates the number of nodes $n' = 2L$ along θ. Using this transformation, we could form spherical cap and saddle-like structures with a targeted number of legs (Figure 2-9**k, l**, Figure 2-14). The examples in Figure 2-9 show the versatility of our approach in creating diverse 3D morphologies. These structures can be further used as a building block for multimodular 3D structures.

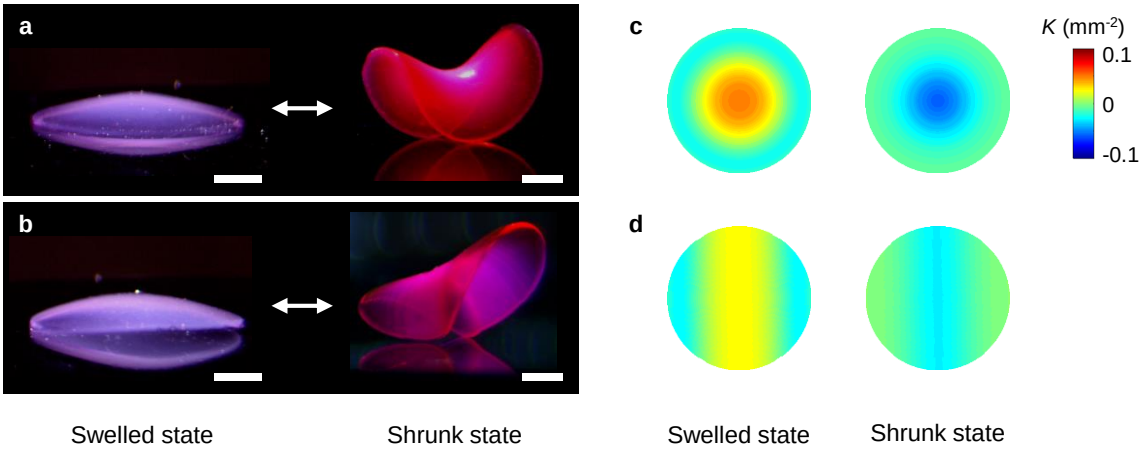

Figure 2-12 **3D structures with continuously varying morphologies along the θ direction.** (**a**, **b**) 3D structures created with $\Omega(r, \theta)$ in Figure 2-9i with $L = 0$ (**a**) and $L = 1$ (**b**). The structures on the left and right sides are at the swelled and shrunk states, respectively. Scale bars, 5 mm (left); 2 mm (right). (**c**, **d**) Corresponding Gaussian curvature K maps of the structures with $L = 0$ (**c**) and $L = 1$ (**d**) at the swelled and shrunk states. Gaussian curvature K is calculated from Ω in Figure 2-9i.

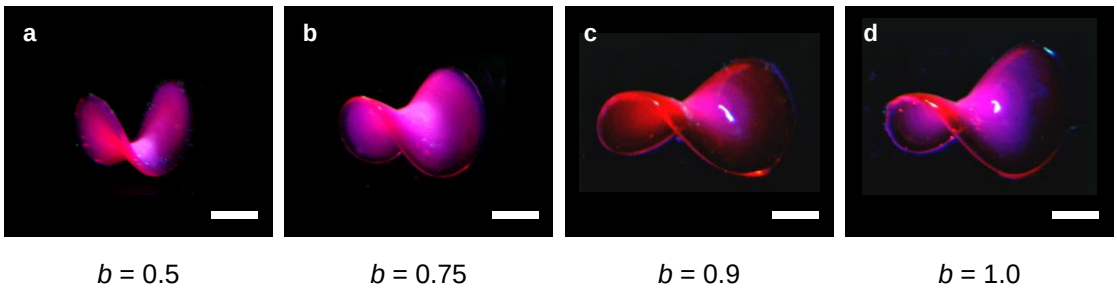

Figure 2-13 **Elongated elliptical saddle structures.** The elongated elliptical saddle structures were created by transforming axisymmetric Ω for an saddle shape into a nonaxisymmetric form $\Omega(r, \theta) = c\Omega(r/(a(\theta)R))$, where $a(\theta) = b/\sqrt{1 + (b^2 - 1)\sin^2\theta}$. The major and minor axes of the ellipse are R and bR ($0 < b < 1$) or bR and R ($b > 1$), respectively. The elongated elliptical saddle structures were formed with $b = 0.5$ (**a**), $b = 0.75$ (**b**), $b = 0.9$ (**c**), and $b = 1.0$ (**d**), respectively. The structure with $b = 0.5$ in **a** is also shown in Figure 2-9j. Scale bars, 2 mm.

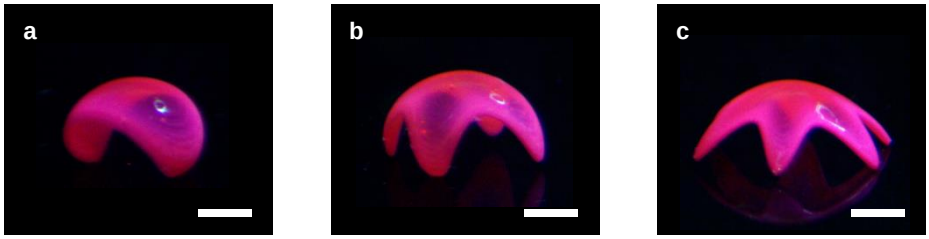

Figure 2-14 **Spherical caps with a targeted number of legs (nodes).** The spherical caps with a targeted number of legs (nodes) were created by transforming axisymmetric $\Omega(r)$ for a spherical cap into a nonaxisymmetric form $\Omega(r, \theta) = c\Omega(r/(a(\theta)R))$, where $a(\theta) = b/\sqrt{1 + (b^2 - 1)\sin^2 L\theta}$. The transformed $\Omega(r, \theta)$ has the period of π/L along the θ direction and thus induces a 3D structure with $2L$ nodes (legs). b defines the ratio of the inner diameter to the outer diameter of the structure (and thus the length of the legs). The spherical caps with 2 (**a**), 4 (**b**), and 6 (**c**) legs were formed using $\Omega(r, \theta)$ with $b = 0.5$ and $L = 1$, 2, and 3, respectively. Scale bars, 2 mm.

2.4.5 Multimodular 3D structures

The modular assembly of target metrics can create 3D structures with broad morphological and functional diversity (Figure 2-15, Figure 2-16)[4]. However, there is an intrinsic problem in assembling modules in the metric space[4]. Each module can randomly adopt the direction of deformation (e.g., upward or downward)[4] or the orientation with respect to other modules due to the symmetric nature of metrics. Thus, a multimodular **Ω** can in general form multiple different conformations presumably with the same elastic energy (as shown in previous work[4] and Figure 2-16). To tackle this problem, we introduced the concept of transitional components, designed to control the direction of deformation and the orientation of modular components (Figure 2-15**a**–**j**). A saddle-like structure with $K < 0$ (e.g., Figure 2-6**b**, Figure 2-9**j**) has the principle curvatures with the same sign along its parallel edges. We thus postulated that modular components with $K > 0$ that share the parallel edges of a saddle-like structure ($K < 0$), or a parallel transitional component (e.g., small circles with dashed white lines in Figure 2-15**f**–**i**), would deform in the same direction as the parallel edges. On the other hand, modular components with $K > 0$ that share the perpendicular edges of a saddle-like structure ($K < 0$), or a perpendicular transitional component (e.g., large circles with dashed white lines in Figure 2-15**f**–**i**), would deform in the opposite directions.

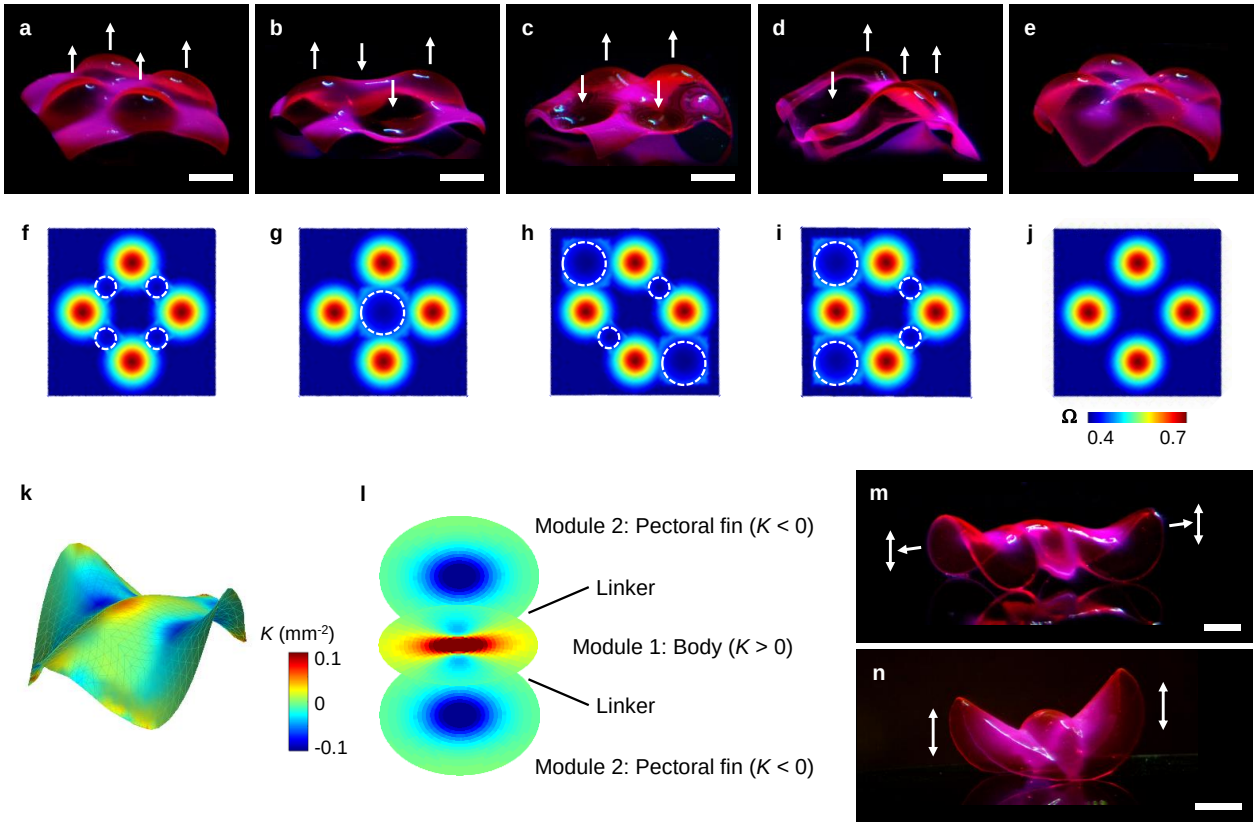

Figure 2-15 **Multimodular 3D structures. a**–**e** Examples of multimodular 3D structures with 4 modules with (**a–d**) and without (**e**) directional control. The modules were programmed to deform in the directions indicated by the white arrows. **f–j** Strategies to control the orientation of the modules in the corresponding structures in **a–e**. The color maps illustrate **Ω** used to create the structures. The small and large circles with white dashed lines indicate the parallel and perpendicular transitional components, respectively. **k** Reconstructed 3D image of a stingray model with K. **l** Modular design of a stingray-inspired 3D structure in **m**. The modules for the body and the pectoral fins were designed based on the K map in **k** and Figure 2-17. **m**, **n** Stingray-inspired 3D structures with oscillatory flapping motions. The white arrows indicate the direction of the motions. Scale bars, 4 mm in **a–e**; 2 mm in **m**; 4 mm in **n**.

Figure 2-15**a–d** show examples of multimodular structures with directional control, where the arrows indicate the programmed orientation of each module. Placing the parallel and perpendicular transitional components between modules (indicated by the small and large circles

with white dashed lines in Figure 2-15**f–i**, respectively) led to the multimodular structures with designed morphologies (Figure 2-15**a–d**). In contrast, the modules in a control structure without transitional components tend to deform in the same direction, implying slight variations in shrinkage through the thickness; the variations make a specific direction energetically favorable for all modules (Figure 2-15**e, j**).

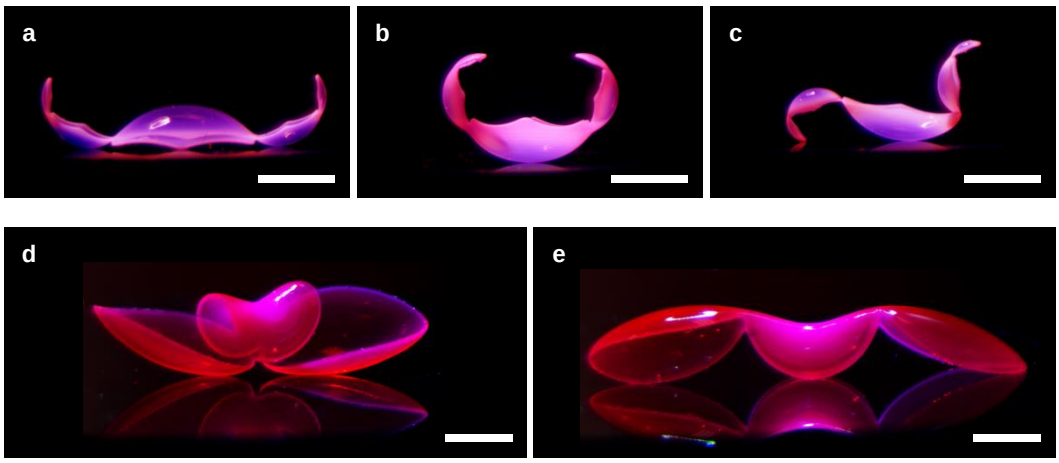

Figure 2-16 **Multimodular 3D structures with the same target metric but different conformations.** (**a**–**c**) Multimodular structures that consist of a modular component with $K > 0$ (spherical cap with $R = 10$ mm in Equation 12 in Section 2.4.2.2) in the center and two smaller components with $K > 0$ (spherical caps with $R = 5$ and 2.5 mm in Equation 12 in Section 2.4.2.2) on the left and right sides. The three structures in **a**, **b**, and **c** were formed with the same growth function but have different conformations, as the modules can randomly select a direction of deformation (upward or downward) with respect to neighboring modules. Scale bars, 2 mm. (**d**, **e**) Multimodular structures that consist of a module with $K < 0$ in the center and two modules with $K > 0$ on the left and right sides. The two structures shown in **d** and **e** were formed with the same growth function but have different conformations, as the modules can randomly adopt an orientation with respect to neighboring modules. Scale bars, 4 mm.

The design rules established in this work (Figure 2-9, Figure 2-15) offer simple yet versatile ways to build complex 3D structures without the need for extensive computation. To demonstrate this capability, we fabricated ray-inspired 3D structures that replicate the key morphological features of stingrays, including the pectoral fins with $K < 0$ (Figure 2-15**k–n**)[21, 52]. We designed multi-modular structures based on the reconstructed 3D images, K, and swimming motions of stingrays (Figure 2-15**k, l**, Figure 2-17)[21, 52]. The growth functions for the body and the pectoral fins were designed and merged with linear linkers (Figure 2-15**l**), using the design rules shown in Figure 2-9, Figure 2-15**a–j**. For example, the module for the body structure with the linkers was used as a transitional component that controls the orientation of the left and right pectoral fins with respect to the body and thus synchronizes their motions (Figure 2-18). Furthermore, the ray-inspired structures were designed to produce different types of oscillatory flapping motions in response to temperature cycles (between 31.5 °C and 33.5 °C), mimicking those of stingrays.

We designed and fabricated stingray-inspired 3D structures (Figure 2-15**m, n**) based on the 3D morphology and swimming motions of stingrays in literature[21, 52]. We first reconstructed and rendered the 3D morphology of a stingray using a computer-aided 3D modeling and rendering tool (3ds Max, Autodesk) as shown in Figure 2-17**a**. We then calculated K and H^2 from the reconstructed 3D image using MATLAB (Figure 2-15**k**, Figure 2-17**b**). To fabricate the stingray-inspired 3D structure (Figure 2-15**m**), we designed the modular components that mimic K and the morphologies of the body and the pectoral fins of the stingray model (Figure 2-15**k, l**, Figure 2-17). For the body structure with $K > 0$ (module 1), we designed Ω_{body} by transforming $\Omega(r) = c[1 + (r/R')^2]^{\alpha-1}$ with $\alpha = 0.8$ ($K > 0$; Figure 2-6**l, m**, Figure 2-8) to $\Omega(r, \theta) = \Omega(r/(a(\theta)R))$, where $a(\theta) = b/\sqrt{1 + (b^2 - 1)\sin^2\theta}$ with $b = 0.5$. This transformation changes the

axisymmetric 3D structure ($K > 0$) into an elongated structure with an aspect ratio of 2 ($b = 0.5$). For the pectoral fins with $K < 0$ (module 2), we designed Ω_{fin} by transforming $\Omega(r) = c[1 + (r/R')^2]^{\alpha-1}$ with $\alpha = 1.5$ ($K < 0$) to $\Omega(r, \theta) = \Omega(r/(a(\theta)R))$, where $a(\theta) = b/\sqrt{1 + (b^2 - 1)\sin^2\theta}$ with $b = 0.75$. $\Omega(r) = c[1 + (r/R')^2]^{\alpha-1}$ with $\alpha > 1$ induces a 3D structure with $K < 0$, which is a negative analog to the structures with $K > 0$ shown in Figure 2-6**l** and Figure 2-8. To merge the pectoral fins with the body, we introduced linear linkers between Ω_{body} and Ω_{fin}, as described in Figure 2-9**c** and Figure 2-11. The structure for the body ($K > 0$) along with the linkers functions as transitional components, which control the direction of deformation of the pectoral fins ($K < 0$) and their orientation with respect to the body and thus synchronize the motions of the left and right fins in response to temperature cycles. Without proper linkers, the modular components can be randomly oriented (Figure 2-18). We designed and fabricated the stingray-inspired 3D structure in Figure 2-15**n** as described above, using two modular components: (i) the body structure ($K > 0$) and (ii) the pectoral fin structures ($K < 0$). The motions of the ray-inspired structures (Figure 2-15**m, n**) were controlled by modulating temperature cycles between 31.5 °C and 33.5 °C in a temperature-controlled water bath. For detailed observations of shape changes, we changed the temperature slowly.

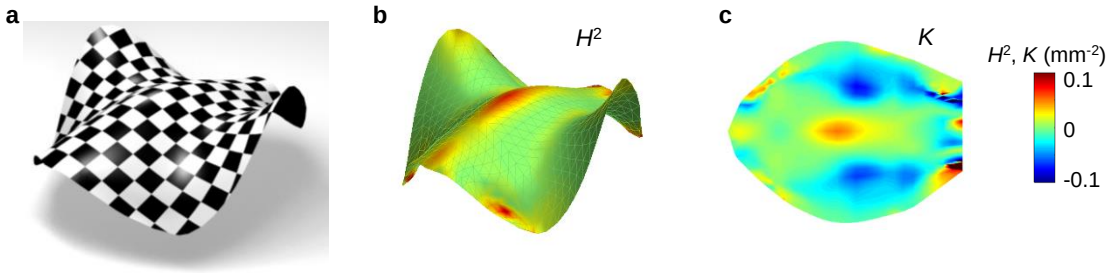

Figure 2-17 **Design of stingray-inspired 3D structures. a**, Reconstructed 3D image and rendering of a stingray. The 3D image was reconstructed based on the 3D morphology of stingrays in literature[21, 52]. **b**, Reconstructed 3D image of the stingray model with squared mean curvature H^2. **c**, Top-view of the reconstructed 3D image of the stingray model with K (Figure 2-15k).

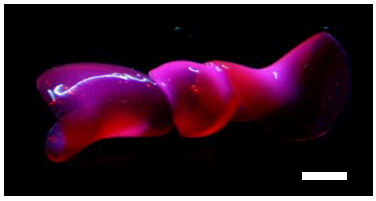

Figure 2-18 **Stingray-inspired 3D structure without linkers.** The stingray-inspired 3D structure was constructed with the same modules for the body and the pectoral fins used in the structure in Figure 2-15m but without linkers. Although they maintain the designed shape ($K < 0$), the pectoral fin structures are randomly oriented with respect to the body without linkers. Scale bar, 2 mm.

2.4.6 Dynamic behavior of growth-induced 3D structures

We next explored how growth-induced 3D structures transform their shapes (Figure 2-19). To elucidate the underlying mechanism of the shape evolution, we introduced the concept of dynamic target metrics (Figure 2-19**a**–**e**). To verify this concept, we used a spherical cap structure shown in Figure 2-6**a** as our model system. Figure 2-19**a** shows the shape evolution of a spherical cap. Despite its simple shapes at equilibrium (swelled and shrunk states), the structure undergoes complex shape transformations. Our results reveal that the spatially nonuniform rates of swelling and shrinking of growth-induced 3D structures determine their dynamic shape changes as described below.

To understand the dynamic behavior, we first measured A_T/A_0 of homogeneous hydrogels (i.e., hydrogel disks uniformly crosslinked by t_{ex}) as a function of time t during cooling (Figure 2-19**b**). The measurements indicate that the swelling rates decrease with t_{ex} (as shown in Figure 2-1**d**), reflecting the difference in the rate of diffusion of water through the hydrogels with different densities (supporting the mechanism in Figure 2-1). The crossover of A_T/A_0 of hydrogels prepared with short and long t_{ex} at around 30 to 35 min (indicated by the dashed black line in Figure 2-19**b**) implies how growth-induced structures transform between shapes with $K > 0$ and $K < 0$ (e.g., Figure 2-6**a**–**c, j**, Figure 2-19**a**).

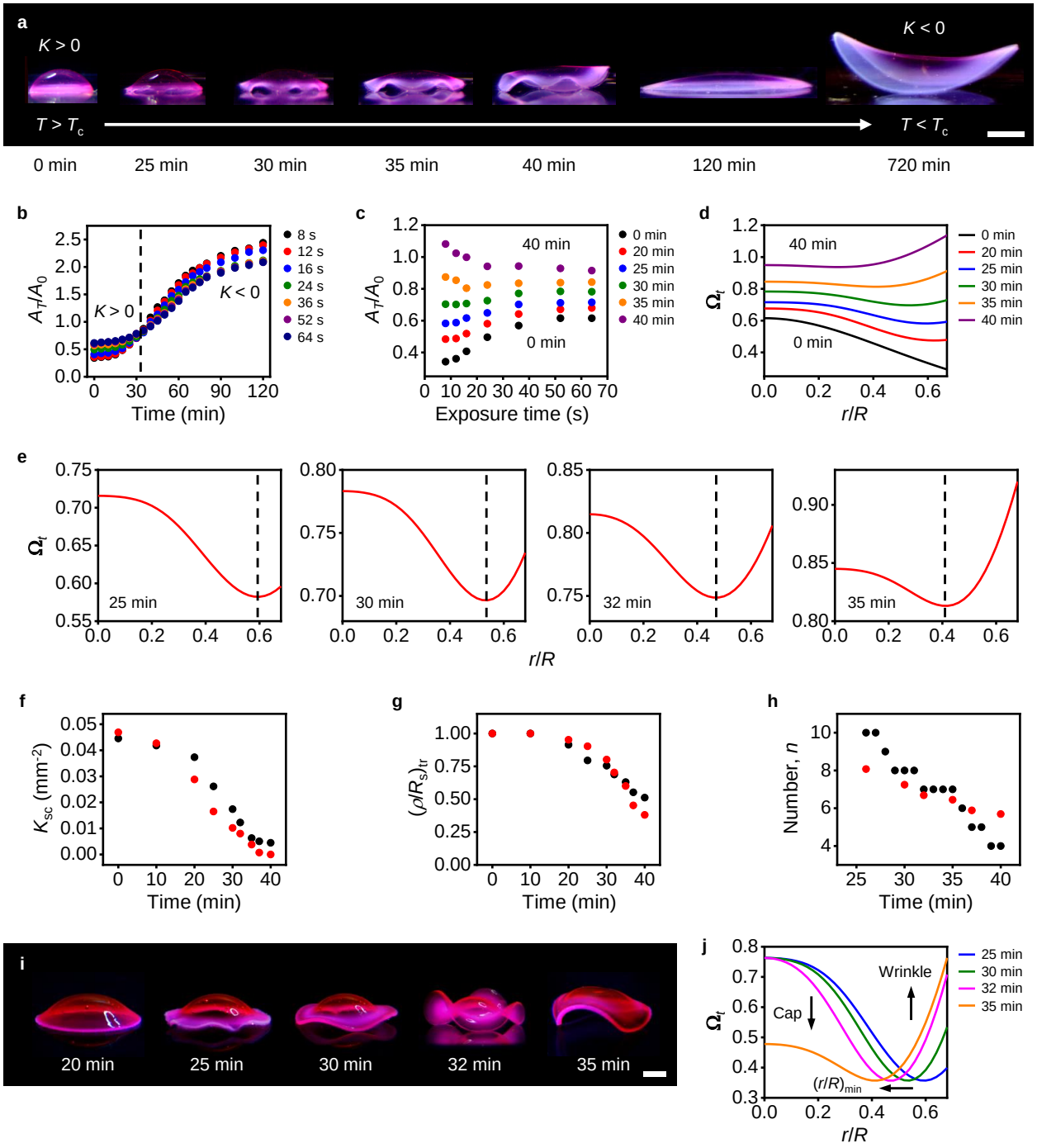

Figure 2-19 **Dynamic behavior of growth-induced 3D structures. a** Shape evolution of a spherical cap during cooling. **b** A_T/A_0 of homogeneous hydrogels formed with different t_{ex} as a function of cooling time t. The black, red, blue, green, orange, purple, and navy circles represent A_T/A_0 of the hydrogels formed with t_{ex} of 8, 12, 16, 24, 36, 52, and 64 s, respectively. **c** A_T/A_0 in **b** as a function of t_{ex} at different t (dynamic calibration curves). The black, red, blue, green,

orange, and purple circles represent A_T/A_0 at t of 0, 20, 25, 30, 35, and 40 min, respectively. **d** Dynamic growth function (or target metric) $\boldsymbol{\Omega}_t$ of the spherical cap at $t = 0$ to 40 min. The black, red, blue, green, orange, and purple line represent Ω_t at t of 0, 20, 25, 30, 35, and 40 min, respectively. **e** $\boldsymbol{\Omega}_t$ for the shapes of the spherical cap in **a** at 25, 30, 32, and 35 min. **f** Experimentally measured K_{sc} (K of the spherical cap-like shape in the center) (black circles) and theoretically calculated K_{sc} (red circles) as a function of t. **g** Experimentally measured $(\rho/R_{\mathrm{s}})_{\mathrm{tr}}$ (location of the shape transition) (black circles) and theoretically calculated $(\rho/R_{\mathrm{s}})_{\mathrm{tr}}$ (red circles) as a function of t. **h** Experimentally measured number of the wrinkles (black circles) as a function of time. The red circles represent n obtained from the fit of $\boldsymbol{\Omega} = c/[1 + (r/(aR))^2]^2 + [1 + (r/R)^n]^2 - 1$ to $\boldsymbol{\Omega}_t$ as described in the main text and Figure 2-25. **i** Replicated structures of the dynamic shapes of the spherical cap in **a** at 20, 25, 30, 32, and 35 min. **j** Normalized Ω_t used to create the structures shown in **i**. The blue, green, magenta, and orange lines represent $\boldsymbol{\Omega}_t$ at 25, 30, 32, and 35 min, respectively. Scale bars, 5 mm in **a**; 2 mm in **i**.

To quantitatively describe the shape evolution, we next constructed dynamic calibration curves (A_T/A_0 as a function of t_{ex} at times t) using A_T/A_0 shown in Figure 2-19**b** (Figure 2-19**c**, Figure 2-20), analogous to the static calibration curves (Figure 2-1**b, c**). The dynamic calibration curves show how the local areas created with t_{ex} in 3D structures swell (or shrink) with t. $A_T/A_0(t_{\mathrm{ex}})$ changes from the static calibration curve at the shrunk state (i.e., $A_T/A_0(t_{\mathrm{ex}})$ at $t = 0$ min in Figure 2-19**c**) to the static calibration curve at the swelled state (Figure 2-20). We can then determine how $\boldsymbol{\Omega}$ for a 3D shape evolves with t (dynamic growth function or target metric $\boldsymbol{\Omega}_t$) from $\boldsymbol{\Omega}$ at $t = 0$ min (i.e., $\boldsymbol{\Omega}$ at the shrunk state), using the dynamic calibration curve $A_T/A_0(t_{\mathrm{ex}})$ at t.

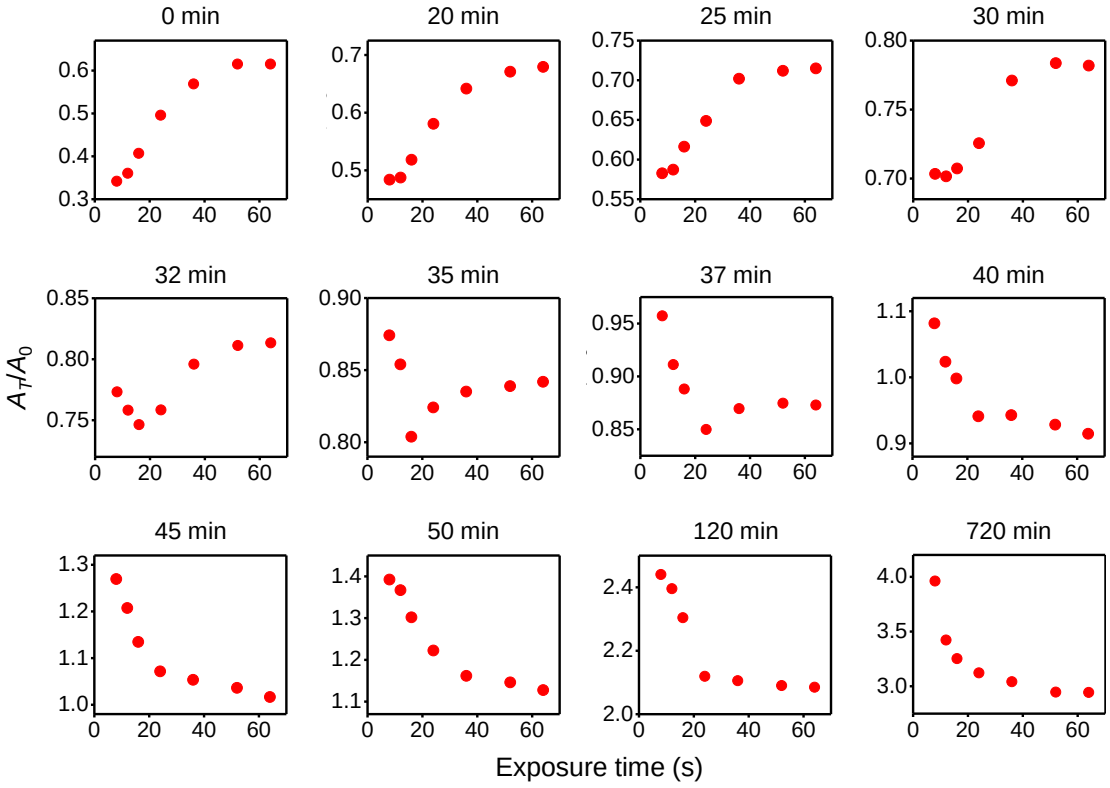

Figure 2-20 **Time-dependent areal swelling and shrinking ratios as a function of light exposure time at different times during cooling.** The areal swelling and shrinking ratios as a function of light exposure time t_{ex} at different times t during cooling were constructed using Figure 2-19b. $A_T/A_0(t_{\mathrm{ex}})$ changes from an increasing function of t_{ex} (shrunk state) to a decreasing function of t_{ex} (swelled state) with time. The transition of $A_T/A_0(t_{\mathrm{ex}})$ reflects how the spherical cap in Figure 2-19a transforms from a shape with $K > 0$ at the shrunk state to a shape $K < 0$ at the swelled state.

Having established the procedure to determine $\boldsymbol{\Omega}_t$, we applied the concept of dynamic target metrics to investigate the shape evolution of the spherical cap structure (Figure 2-19**a**). We determined $\boldsymbol{\Omega}_t$ for the spherical cap (Figure 2-19**d**, **e**, Figure 2-21) from its static growth function (shown in Figure 2-6**g**), using the dynamic calibration curves (shown in Figure 2-19**c**, Figure 2-20).

$\boldsymbol{\Omega_t}$ shows how the metric of the spherical cap changes with time and thus how the structure changes its shape (Figure 2-19**d, e**, Figure 2-21, Figure 2-22).

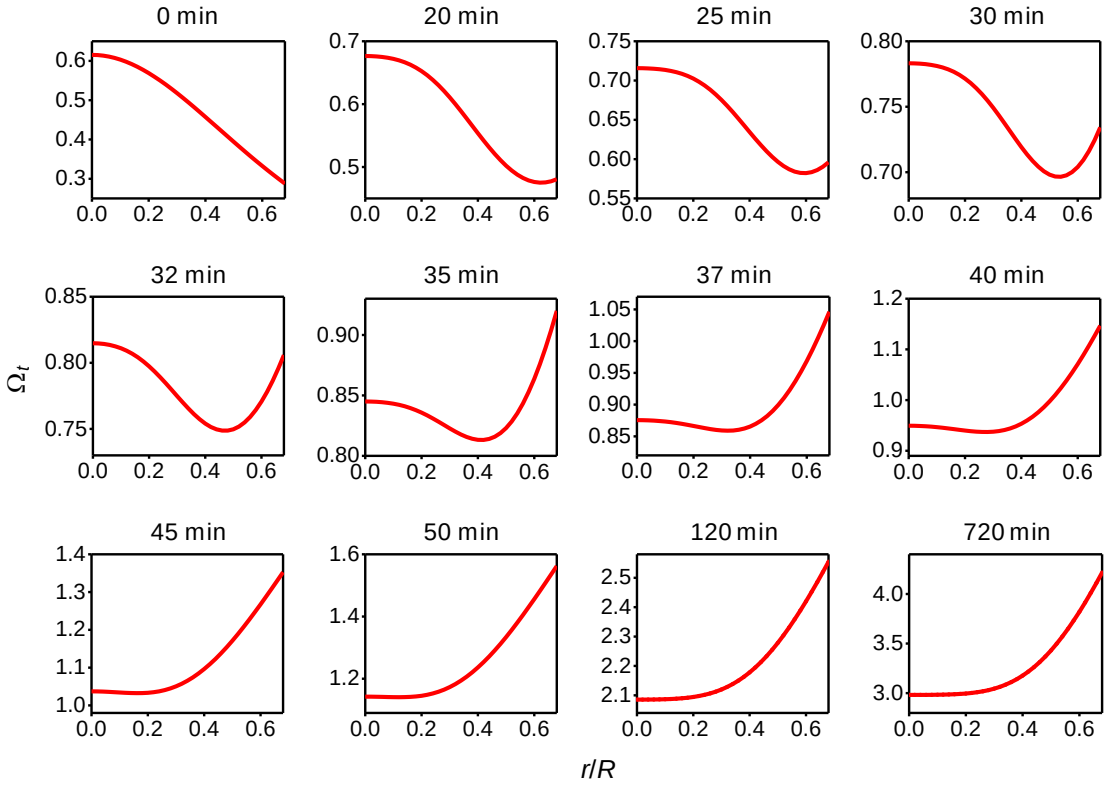

Figure 2-21 **Dynamic growth functions (target metrics) for a spherical cap structure at different times during cooling.** The dynamic growth functions (or target metrics) Ω_t of the spherical cap at different times during cooling (Figure 2-19a) were constructed from Ω for a spherical cap structure (Figure 2-6g) using the dynamic calibration curves (Figure 2-20). Ω_t changes from a decreasing function of r/R to an increasing function, reflecting the transformation of the spherical cap shape ($K > 0$) at the shrunk state to the saddle-like shape ($K < 0$) at the swelled state.

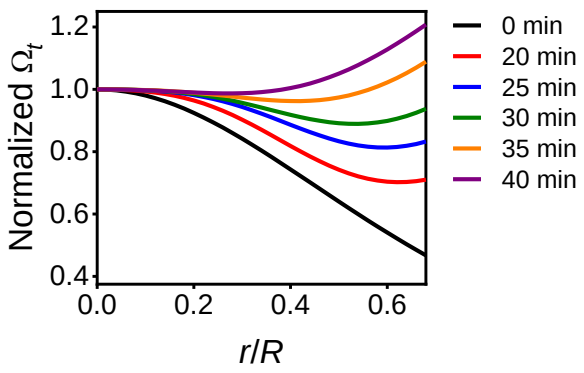

Figure 2-22 **Normalized dynamic $\boldsymbol{\Omega_t}$ t of the spherical cap structure at t= 0 to 40 min.**

During this transition, $\boldsymbol{\Omega_t}$ undergoes complex transformations, forming hybrid elliptic and hyperbolic metrics (Figure 2-19**d, e**) and thus inducing hybrid 3D shapes (Figure 2-19a, Figure 2-23). The spatially nonuniform kinetics of swelling produces hybrid $\boldsymbol{\Omega_t}$ with a minimum at $(r/R)_{\min}$ at t of 20 to 40 min (as indicated by dashed black lines in Figure 2-19**e** and Figure 2-23). $\boldsymbol{\Omega_t}$ at $r/R < (r/R)_{\min}$ and $r/R > (r/R)_{\min}$ represents the spherical cap-like shape in the center ($K > 0$) and the wrinkles in the edge ($K < 0$), respectively. The functional form of $\boldsymbol{\Omega_t}$ (e.g., sharp change in the gradient of $\boldsymbol{\Omega_t}$ at $r/R > (r/R)_{\min}$) reflects how $\boldsymbol{\Omega_t}$ forms wrinkles, reminiscent of Enneper's surfaces (Figure 2-6**i–k**, Figure 2-7).

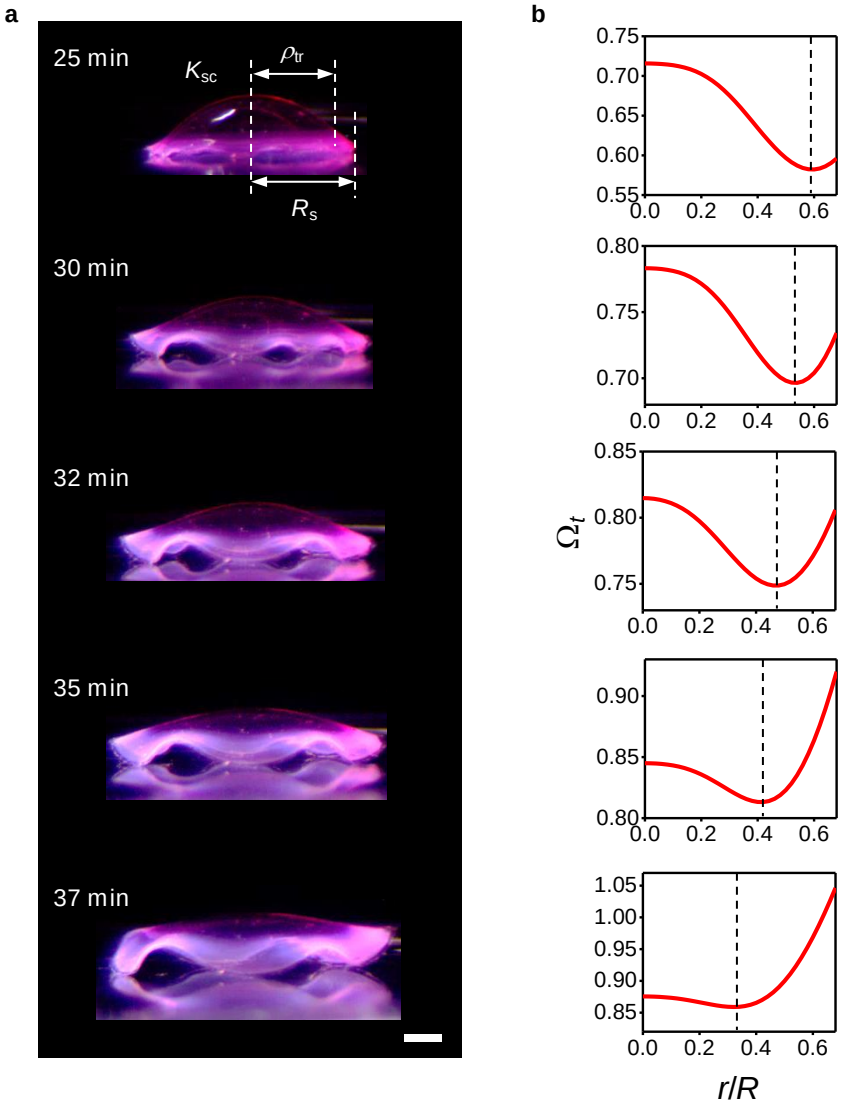

Figure 2-23 **Dynamic shapes of the spherical cap structure. a**, Dynamic shapes of the spherical cap structure shown in Figure 2-19a at 25, 30, 32, 35, and 37 min. The location of the shape transition between the spherical cap-like shape ($K > 0$) and the wrinkles ($K < 0$) $(\rho/R_s)_{tr}$ was obtained by measuring ρ_{tr} and R_s as shown in the structure at 25 min: $(\rho/R_s)_{tr} = \rho_{tr}/R_s$. Scale bar, 2 mm. **b**, Ω_t for the spherical cap at 25, 30, 32, 35, and 37 min. The location of the minimum $(r/R)_{min}$, indicated by the dashed lines in the graphs, shifts from the edge toward the center with time.

To demonstrate that $\boldsymbol{\Omega_t}$ predicts the dynamic shape change, we quantified the shape evolution of the spherical cap structure at 0 to 40 min and compared it with our theoretical model

(Figure 2-19**f**–**h**, Figure 2-23, Figure 2-24, Figure 2-25). We characterized the dynamic shapes by Gaussian curvature of the spherical cap-like shape in the center K_{sc} (Figure 2-19**f**), the location of the shape transition between the spherical cap-like shape ($K > 0$) and the wrinkles ($K < 0$) $(\rho/R_s)_{tr}$, where ρ is the radial coordinate of the 3D structure and R_s is the radius of the structure (Figure 2-19**g**, Figure 2-23, Figure 2-24), and the number and amplitude of wrinkles (Figure 2-19**,** Figure 2-25). The experimentally measured K_{sc} decreases with time and the spherical cap-like shape gradually disappears at around 40 min ($K \to 0$), matching well with K_{sc} obtained from $\boldsymbol{\Omega}_t$ (Figure 2-19**f**). The measured $(\rho/R_s)_{tr}$ decreases with time (i.e., shifts toward the center of the structure), showing a good agreement with $(\rho/R_s)_{tr}$ calculated from $(r/R)_{min}$ (using Equation 8 in Section 2.4.2.1). The shift of $(\rho/R_s)_{tr}$ (or $(r/R)_{min}$) results in the decrease in the region of the spherical cap-like shape and the increase in the region of the wrinkles.

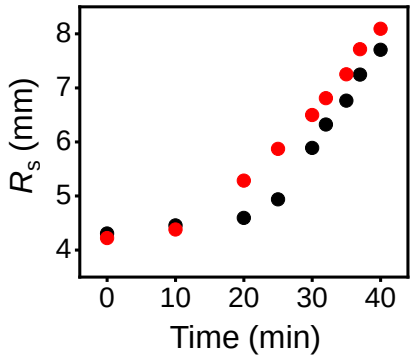

Figure 2-24 **Radius of the spherical cap structure as a function of time.** The radius R_s of the dynamic shapes of the spherical cap structure shown in Fig 5a was measured as a function time (black circles) as shown in Figure 2-23a. The theoretically calculated R_s (red circles) was obtained from Ω_t (Figure 2-19d, e, Figure 2-21) using Equation 8 in Section 2.4.2.

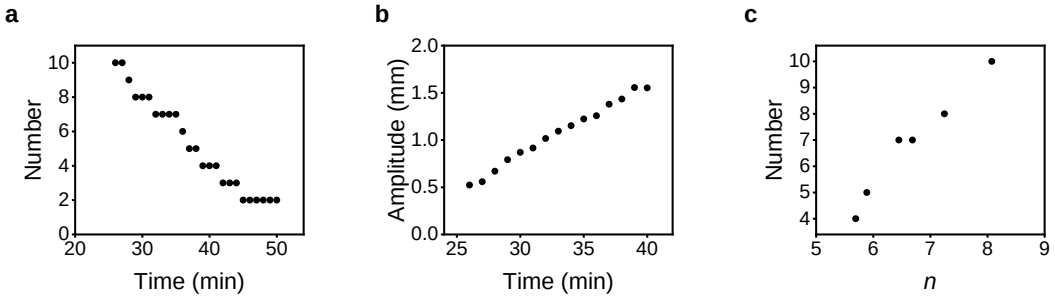

Figure 2-25 **Experimentally measured number and amplitude of the wrinkles in the dynamic shapes of the spherical cap structure. a**, Experimentally measured number of the wrinkles of the spherical cap structure shown in Figure 2-19a as a function of time. **b**, Experimentally measured maximum amplitude of the wrinkles of the structure as a function of time. **c**, Experimentally measured number of the wrinkles shown in **a** as a function of n. The values of n were obtained by fitting $\Omega = c/[1 + (r/(aR))^2]^2 + [1 + (r/R)^n]^2 - 1$ to Ω_t (shown in Figure 2-19d, e and Figure 2-21), where the first and second terms in Ω represent the spherical cap-like shape (a functional form of spherical caps in Figure 2-6g) and the wrinkles (a functional form of Enneper's surfaces in Figure 2-6k), respectively, and c, a, and n are constants. As observed in Enneper's surfaces (Figure 2-6i–k, Figure 2-7), the number of wrinkles in the structure increases with n.

Furthermore, our theoretical model describes how the number of the wrinkles decreases with time while their amplitude increases (as shown in Figure 2-19a and Figure 2-23). To understand how the structure forms the wrinkles, we fitted $\boldsymbol{\Omega} = c/[1 + (r/(aR))^2]^2 + [1 + (r/R)^n]^2 - 1$ to $\boldsymbol{\Omega}_t$, where the first and second terms in $\boldsymbol{\Omega}$ represent the spherical cap-like shape (as shown in Figure 2-6**g**) and the wrinkles (a functional form of Enneper's surfaces in Figure 2-6**k**), respectively, and c, a, and n are constants. The results show that n decreases with time, suggesting that the decrease in n results in the decrease in the number of the wrinkles and the increase in their amplitude (Figure 2-19**h**, Figure 2-25), as observed in Enneper's surfaces with different n' (Figure 2-6**i–k**, Figure 2-7)[4, 37]. The dynamic K maps theoretically calculated from $\boldsymbol{\Omega}_t$ reflect the experimentally observed shape transformations (Figure 2-26).

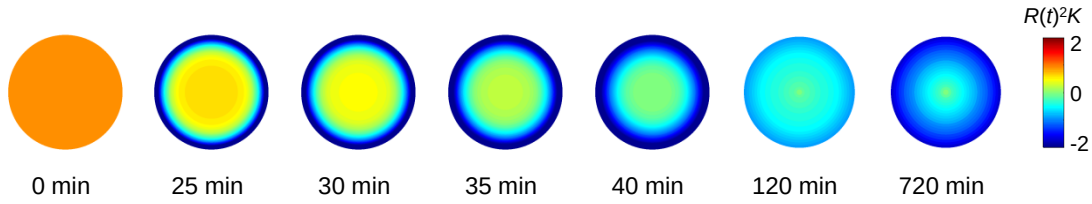

Figure 2-26 **Maps of normalized Gaussian curvature of the spherical cap structure at different times during cooling.** The maps of normalized Gaussian curvature $R^2(t)K$ of the spherical cap structure at different times (Figure 2-19a) were constructed from Ω_t shown in Figure 2-21. The K maps reflect the experimentally observed shape transformations shown in Figure 2-19a as described in the main text. $R(t)$ is the time-dependent R in the coordinate of 3D structures at the swelled and shrunk states (ρ, φ, z) calculated by Equation 8 in Section 2.4.2: $R(t)^2 = \Omega_t(R)R^2$.

To further demonstrate that $\boldsymbol{\Omega_t}$ can predict the dynamic behavior of growth-induced 3D structures, we replicated the dynamic shapes of the spherical cap using $\boldsymbol{\Omega_t}$ (Figure 2-19**i**). Because the full range of $\boldsymbol{\Omega_t}$ is not accessible by our material systems, we rescaled $\boldsymbol{\Omega_t}$ to the experimentally accessible range of $\boldsymbol{\Omega}$ (Figure 2-19**j**). The replicated structures reproduce the key signatures of the shape evolution, including the formation of wrinkles and their shape changes (e.g., increase in the amplitude of wrinkles, decrease in their number, and gradual disappearance of the spherical cap-like shape in the center) (Figure 2-19**i**). The discrepancy in the detailed shapes (e.g., enhanced wrinkles) is attributed to the use of normalized $\boldsymbol{\Omega_t}$. Moreover, this approach that uses $\boldsymbol{\Omega_t}$ for 3D shaping provides new pathways for creating complex 3D structures. This approach offers rich sources to design complex 3D shapes, difficult to access with current theories (e.g., wrinkle formation)[35], and to understand how differential in-plane growth translates to 3D shapes. Manufacturing complex 3D structures, such as those shown in Figure 2-19**i**, is difficult and expensive to achieve by other methods.

2.4.7 Dynamic 3D structures with programmed sequential motions

Another important finding is that the swelling and shrinking rates of our hydrogel systems are phototunable and thus locally programmable. To demonstrate the ability to control the speed of shape change, we created saddle structures with an identical shape but different speeds of shape transformation (Figure 2-27**a, b**, Figure 2-28).

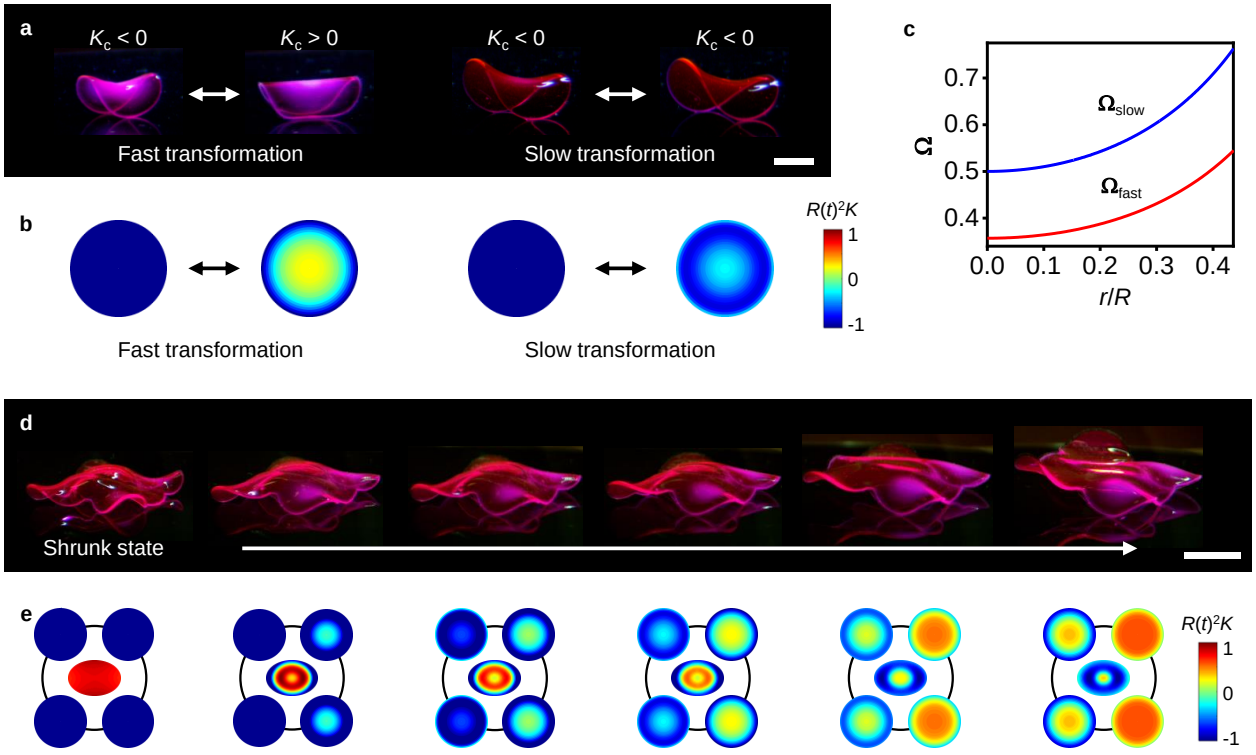

Figure 2-27 **Dynamic 3D structures with programmed sequential motions. a** Fast and slowly transforming saddle structures at $t = 0$ (left) and 30 min (right) during cooling. K_c is K in the center of structures. **b** Theoretically calculated K of the structures in **a**. $R(t)^2K$ is normalized K using the time-dependent R as described in Figure 2-26. **c** Growth functions used to create the saddle structures with different speeds of shape transformation in **a**. The red and blue lines represent $\boldsymbol{\Omega}_{\mathbf{fast}}$ and $\boldsymbol{\Omega}_{\mathbf{slow}}$ used to create the fast and slowly transforming structures in **a**, respectively. **d** Ray-inspired 3D structure with programmed sequential motions. The images show the structure at the equilibrium shrunk state and the dynamic structures at 0, 5, 10, 20, and 25 min during cooling of a temperature cycle (from left to right). **e** Theoretically calculated dynamic K maps of the modules in the structures in **d** at the equilibrium shrunk state and at 0, 5, 10, 20, and 25 min during cooling (from left to right). Scale bars, 2 mm in **a**; 5 mm in **d**.

To create these structures, we designed $\boldsymbol{\Omega}_{\text{fast}}$ and $\boldsymbol{\Omega}_{\text{slow}}$ with the same functional form ($\boldsymbol{\Omega}$ for a saddle shape shown in Figure 2-6**g**) but in different $\boldsymbol{\Omega}$ ranges: $\boldsymbol{\Omega}_{\text{slow}}/\boldsymbol{\Omega}_{\text{fast}} = C$, where C is a constant and $C > 1$ (Figure 2-27**c**). The growth (swelling and shrinking) rates decrease with t_{ex} and thus with $\boldsymbol{\Omega}$ (Figure 2-1**d**, Figure 2-29), but a 3D shape is determined by the relative growth (not by the absolute values of $\boldsymbol{\Omega}$). We can therefore program the speed of shape transformation without changing 3D shapes by controlling the range of $\boldsymbol{\Omega}$ (e.g., the maximum and minimum values of $\boldsymbol{\Omega}$) but maintaining the relative growth (e.g., $\boldsymbol{\Omega}(r/R)/\Omega_{\text{min}}$, where Ω_{min} is a constant). As designed, the structure with $\boldsymbol{\Omega}_{\text{fast}}$ transforms its shape faster than the structure with $\boldsymbol{\Omega}_{\text{slow}}$ (Figure 2-27**a,b**, Figure 2-28). The dynamic K maps theoretically calculated from the dynamic growth functions describe the experimentally observed shape transformations with different speeds (Figure 2-27**b**, Figure 2-28). Within the structures (Figure 2-27**a, b**), due to the difference in the range of $\boldsymbol{\Omega}$, the central regions ($r/R \sim 0$; low range $\boldsymbol{\Omega}$) transform faster than the edge regions ($r/R \sim 0.4$; high range $\boldsymbol{\Omega}$), also seen in the dynamic K maps (Figure 2-27**b**, Figure 2-28). The same trend is observed in the spherical cap structure (Figure 2-27**a**), in which the edge region (low range $\boldsymbol{\Omega}$) transforms faster than the central region (high range $\boldsymbol{\Omega}$) (Figure 2-26).

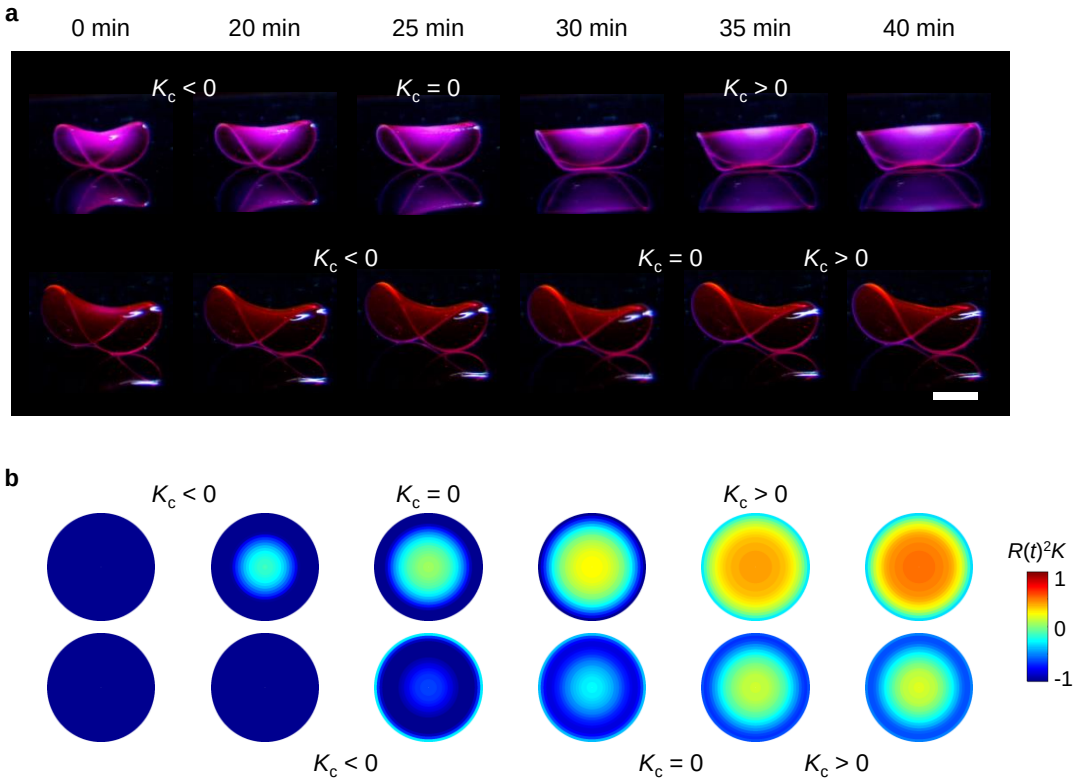

Figure 2-28 **Saddle structures with different speeds of shape transformation. a**, Dynamic shape evolution of saddle structures ($K < 0$) with high and low speeds of shape transformation during cooling. The top (fast) and bottom (slow) structures were created with the growth functions in the low (red line) and high (blue line) ranges in Figure 2-27c, respectively. The two structures have the same shape but different sizes because of the use of Ω in different ranges. As designed, the top structure transforms its shape faster than the bottom structure. For example, the top structure transforms from a shape with $K_c < 0$ to a shape with $K_c > 0$ around 25 min, whereas the bottom structure at around 30 to 35 min. K_c is Gaussian curvature in the center of the structures. Scale bar, 2 mm. **b**, Maps of normalized Gaussian curvature $R^2(t)K$ of the structures in **a**. The dynamic K maps were constructed using Ω_t for the saddle structures.

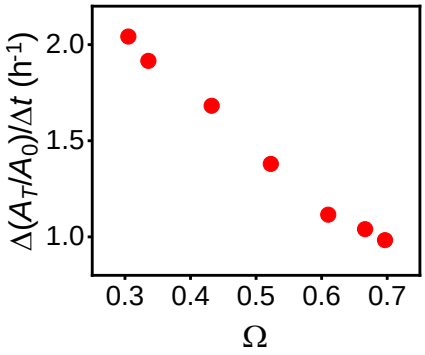

Figure 2-29 **Areal swelling rates (speeds of shape change) as a function of Ω.** The areal swelling rates $\Delta(A_T/A_0)/\Delta t$ were calculated using the swelling rates of the hydrogels as a function of t_{ex} (Figure 2-1d) and the static calibration curve at the shrunk state (Figure 2-1b). As the swelling rate decreases with a value of Ω, we can create structures with different speeds of shape change by programming the structures with different ranges of Ω (as shown in Figure 2-27a–c and Figure 2-28).

The ability to spatially control the rate of shape transformation allows us to create dynamic 3D structures with programmed sequential motions, difficult to achieve with global external stimuli[8]. As a demonstration, we fabricated a ray-inspired 3D structure with programmed sequential motions (Figure 2-27**d, e**,Figure 2-30, Figure 2-31). The structure consists of modules for the body ($K > 0$), front wings ($K < 0$), and rear wings ($K < 0$) (Figure 2-30). The front and rear wings were designed to transform fast and slowly, respectively, and thereby be sequentially actuated in response to temperature change (Figure 2-27**d, e**). As designed, the front wings transform first from a shape with $K_c < 0$ to $K_c > 0$ (around 5 min), gradually lifting the rear wings, while the rear wings slowly transform (e.g., $K_c < 0$ up to 10 min) and flap after 20 min (Figure 2-27**d**). Moreover, we can control the oscillatory motions (e.g., amplitude and frequency) by modulating temperature cycles (Figure 2-31). The theoretically calculated dynamic K maps for each module illustrate the experimentally observed sequential motions (Figure 2-27**e**).

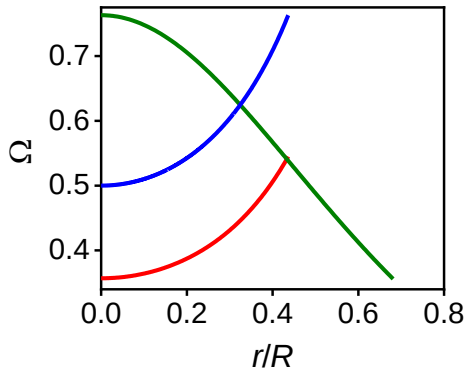

Figure 2-30 **Ω used to fabricate a ray-inspired structure with programmed sequential motions.** Ω shown in green, red, and blue lines were used for the modules for the body, the front wings, and the rear wings of the structure shown in Figure 2-27d, respectively.

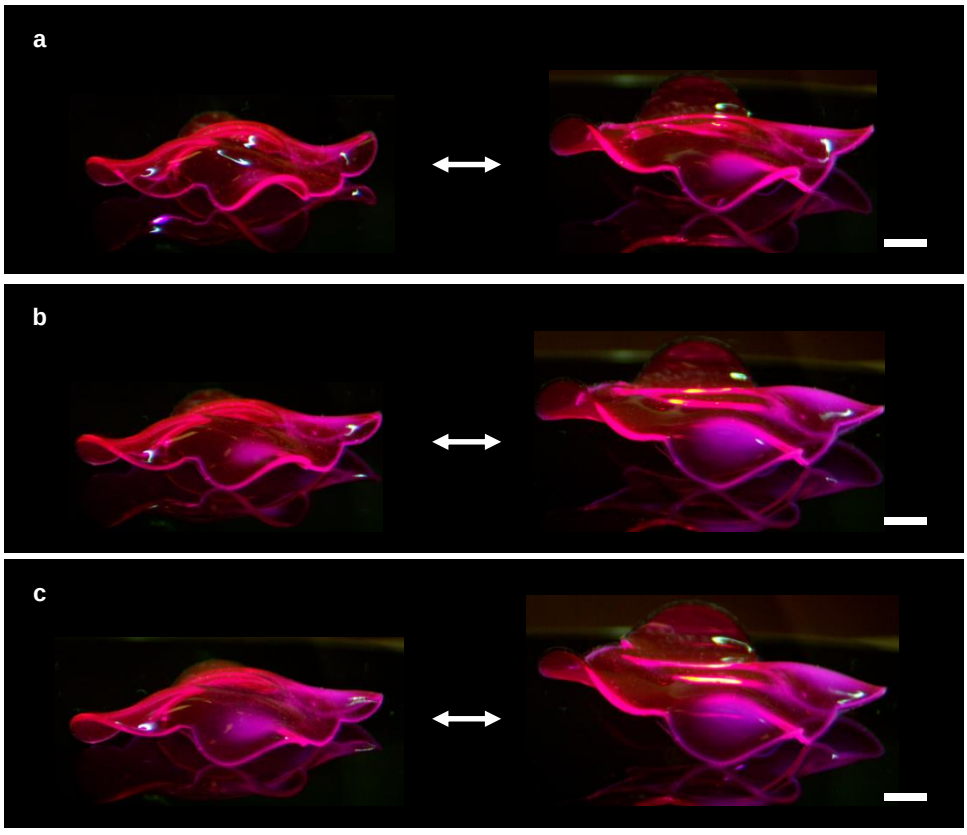

Figure 2-31 **Control of the motions of the ray-inspired structure by modulating temperature cycles.** The motions of the ray-inspired structure can be controlled by modulating temperature cycles. The figures show 3 continuous cycles of the motions with 20 (**a**), 25 (**b**), and 30 (**c**) minute cooling times. By controlling the temperature cycle (e.g., cooling and heating times), the

amplitude and frequency of the programmed motions can be controlled. The amplitude of the motions increases with increasing cooling times. The rear wings show a rapid snapping motion. This behavior is attributed to the transformation of stored elastic energy, resulted from the interactions of the rear wings and the surface, into the kinetic energy of the motions [24, 53]. Scale bars, 2 mm.

2.5 CONCLUSION

Living organisms often achieve 3D morphologies and movements by using spatially patterned and temporally controlled expansion and contraction of continuously deformable soft tissues. Our approach that uses the spatially and temporally controlled growth for programming 3D shapes and their motions, possibly with a large number of degrees of freedom, could thus create dynamic 3D structures that mimic the morphologies and motions of living organisms and thus, potentially, their functions. The ability to program growth-induced 3D shapes and motions could potentially transform the way we design and fabricate soft engineering systems, such as soft robots, actuators, and artificial muscles. The concept is applicable to other programmable materials. The 2D printing approach for 3D material programming represents a scalable and customizable 3D manufacturing technology, potentially integrable with biological systems[1-2, 7, 21, 30] and existing 2D fabrication methods and devices for multifunctionalities and broader applications[54].

2.6 MATERIALS AND METHODS

2.6.1 Preparation of precursor solutions

The precursor solutions for pNIPAm crosslinked with BIS and PEGDA were prepared by dissolving NIPAm (0.4 g), BIS (0.5 mol% of NIPAm), PEGDA with an average molecular weight (MW) of ~700 g mol^{-1} (0.125 mol% of NIPAm), and diphenyl(2,4,6-trimethylbenzoyl)phosphine oxide (PBPO) (0.15 mol% of NIPAm) in 1 mL aqueous solutions (1:3 ratio of water and acetone by volume). The precursor solutions for pNIPAm crosslinked with BIS were prepared by dissolving NIPAm (0.2 g), BIS (0.25 to 5.0 mol% of NIPAm), and PBPO (0.3 mol% of NIPAm) in 1 mL aqueous solutions (1:3 ratio of water and acetone). The precursor solutions for pNIPAm crosslinked with PEGDA were prepared by dissolving NIPAm (0.2 g), PEGDA (1.0 to 10.0 mol% of NIPAm), and PBPO (0.3 mol% of NIPAm) in 1 mL aqueous solutions (1:3 ratio of water and acetone). All materials were purchased from Sigma-Aldrich and used as received.

2.6.2 Creation of shape-morphing 3D structures

Projection lithography cells were prepared by placing a polydimethylsiloxane (PDMS) spacer with a thickness of 400 μm on a PDMS substrate. After purging with nitrogen to reduce the effects of oxygen on photo-polymerization, the precursor solutions were introduced into the cells. The cells were then covered with a glass coverslip (150 μm in thickness). The precursor solutions were then programmed with growth functions (or target metrics) $\boldsymbol{\Omega}$ by spatially and temporally controlled ultraviolet (UV) light (dynamic light projection grayscale lithography).

Shape-morphing 3D structures were created using DL4P. 2D structures that define the boundary of target structures were designed using 3ds Max (Autodesk). Growth functions **Ω** designed for target 3D shapes were converted into 2D maps of light exposure times using the calibration curves of the areal swelling and shrinking ratios versus light exposure time (Figure 2-1**b, c**) with a custom-made MATLAB (MathWorks) code. The growth functions define local A_T/A_0 of 2D structures. STL (stereolithography) files were generated that contains the information of the 2D maps of light exposure times. The precursor solutions were polymerized and crosslinked by spatially and temporally controlled UV light using a digital light processing (DLP) projector (Vivitek D912HD) with the STL files (dynamic light projection lithography). After polymerization and crosslinking, the 2D hydrogel structures were detached from the cell and immediately washed with acetone, isopropyl alcohol (IPA), and water for 3 times to remove unreacted monomers, crosslinkers, and photoinitiators, and suppress photo-polymerization and crosslinking reactions. To achieve the target 3D shapes at the equilibrium swelled state, the hydrogel structures were immersed in water at 4 °C for 72 hours, while exchanging the water every 12 hours, and then at 25 °C for 2 hours in a temperature controlled water bath. To induce the target 3D shapes at the equilibrium shrunk state, the temperature of the water was slowly increased to 35 °C. Food color dyes were introduced into hydrogel structures for imaging. Hydrogel structures without dyes are transparent at equilibrium states.

2.6.3 Measurement of areal swelling and shrinking ratios

Homogeneous pNIPAm hydrogel disks with a diameter of 5 mm (i.e., hydrogel disks formed with constant **Ω**) were prepared by DL4P. The hydrogel disks were uniformly exposed to UV light over the entire disks with light exposure times of 8 to 70 s. The areas of the hydrogel disks at the swelled state A_{25} were measured at 25 °C. The areas of the hydrogel disks at the shrunk state A_{35} were measured at 35 °C. The areal swelling and shrinking ratios are defined as A_{35}/ A_0 and A_{25}/ A_0, respectively, where A_0 is the area of as-prepared hydrogel disks. The hydrogel disks were used to generate the calibration curves of the areal swelling and shrinking ratios versus light exposure time (Figure 2-1**b, c**, Figure 2-2). This process induces essentially no or little variation of swelling and shrinking through the thickness and thus does not induce bending of homogeneous hydrogel disks.

2.6.4 Measurements of mechanical properties and gel points

The dynamic mechanical properties of hydrogels at the swelled state were measured using a rheometer (DHR-2, TA Instruments) with a 20-mm plate geometry. Hydrogel disks with a diameter of 20 mm were used. The shear storage modulus G' and loss modulus G'' were measured by frequency sweeps of 0.01 to 100 rad s^{-1} at an oscillatory strain of 1%. The hydrogel disks with a storage shear modulus larger than 20 Pa were used for the measurements of the swelling and shrinking ratios (Figure 2-1**b, c**, Figure 2-2).

The gel points of hydrogels crosslinked with single crosslinkers were measured by the method of Winter and Chambon (Figure 2-3)[42-43]. Hydrogel disks with a diameter of 20 mm were

prepared with single crosslinkers (BIS and PEGDA; 1 mol% of NIPAm in precursor solutions) with different light exposure times (BIS-crosslinked hydrogels: 4, 8, 12, and 16 s; PEGDA-crosslinked hydrogels: 1, 2, 3, and 4 s). The hydrogel disks that form stable hydrogels after washing with acetone and IPA were used for the measurements. G' and G'' were measured by frequency sweeps of 0.1 to 15 Hz at an oscillatory strain of 0.1% using the rheometer with a 20-mm plate geometry. To determine the gel points, $\tan\delta = G''/G'$ were plotted as a function of frequency. At the gel point, $\tan\delta = G''/G'$ has a constant value over the frequency sweep (Figure 2-3)[42-43].

2.6.5 Reconstruction of 3D images and Gaussian curvatures

The 3D images and Gaussian curvatures K of experimentally created 3D structures were constructed based on the spin image 3D recognition method[55]. 2D images of the 3D structures were captured from different angles by taking images while rotating the structures. 3D images were then reconstructed from the 2D images and converted into STL files using 3ds Max. The reconstructed 3D images with K were constructed using MATLAB with the STL files (Figure 2-6**d–f, l**, Figure 2-8).

2.7 REFERENCES

1.Kim, S.; Laschi, C.; Trimmer, B., Soft robotics: a bioinspired evolution in robotics. *Trends Biotechnol.* **2013,** *31* (5), 287-294.
2.Rus, D.; Tolley, M. T., Design, fabrication and control of soft robots. *Nature* **2015,** *521* (7553), 467-475.
3.Klein, Y.; Efrati, E.; Sharon, E., Shaping of Elastic Sheets by Prescription of Non-Euclidean Metrics. *Science* **2007,** *315* (5815), 1116-1120.
4.Kim, J.; Hanna, J. A.; Byun, M.; Santangelo, C. D.; Hayward, R. C., Designing Responsive Buckled Surfaces by Halftone Gel Lithography. *Science* **2012,** *335* (6073), 1201-1205.
5.Gladman, A. S.; Matsumoto, E. A.; Nuzzo, R. G.; Mahadevan, L.; Lewis, J. A., Biomimetic 4D printing. *Nat. Mater.* **2016,** *15* (4), 413-418.
6.Wu, Z. L.; Moshe, M.; Greener, J.; Therien-Aubin, H.; Nie, Z.; Sharon, E.; Kumacheva, E., Three-dimensional shape transformations of hydrogel sheets induced by small-scale modulation of internal stresses. *Nat. Commun.* **2013,** *4*, 1586.
7.Jamal, M.; Kadam, S. S.; Xiao, R.; Jivan, F.; Onn, T.-M.; Fernandes, R.; Nguyen, T. D.; Gracias, D. H., Bio-Origami Hydrogel Scaffolds Composed of Photocrosslinked PEG Bilayers. *Adv. Healthcare Mater.* **2013,** *2* (8), 1142-1150.
8. Cangialosi, A.; Yoon, C.; Liu, J.; Huang, Q.; Guo, J.; Nguyen, T. D.; Gracias, D. H.; Schulman, R., DNA sequence–directed shape change of photopatterned hydrogels via high-degree swelling. *Science* **2017,** *357* (6356), 1126-1130.
9.Pikul, J. H.; Li, S.; Bai, H.; Hanlon, R. T.; Cohen, I.; Shepherd, R. F., Stretchable surfaces with programmable 3D texture morphing for synthetic camouflaging skins. *Science* **2017,** *358* (6360), 210-214.
10.Shepherd, R. F.; Ilievski, F.; Choi, W.; Morin, S. A.; Stokes, A. A.; Mazzeo, A. D.; Chen, X.; Wang, M.; Whitesides, G. M., Multigait soft robot. *Proc. Natl. Acad. Sci. U. S. A.* **2011,** *108* (51), 20400-20403.
11.Jamal, M.; Zarafshar, A. M.; Gracias, D. H., Differentially photo-crosslinked polymers enable self-assembling microfluidics. *Nat. Commun.* **2011,** *2*, 527.
12. Jeon, S.-J.; Hauser, A. W.; Hayward, R. C., Shape-Morphing Materials from Stimuli-Responsive Hydrogel Hybrids. *Acc. Chem. Res.* **2017,** *50* (2), 161-169.
13.Kuksenok, O.; Balazs, A. C., Modeling the Photoinduced Reconfiguration and Directed Motion of Polymer Gels. *Adv. Funct. Mater.* **2013,** *23* (36), 4601-4610.
14.Lendlein, A.; Jiang, H.; Jünger, O.; Langer, R., Light-induced shape-memory polymers. *Nature* **2005,** *434* (7035), 879-882.
15.Ge, Q.; Sakhaei, A. H.; Lee, H.; Dunn, C. K.; Fang, N. X.; Dunn, M. L., Multimaterial 4D Printing with Tailorable Shape Memory Polymers. *Sci. Rep.* **2016,** *6*, 31110.
16.Iamsaard, S.; Aßhoff, S. J.; Matt, B.; Kudernac, T.; CornelissenJeroen, J. L. M.; Fletcher, S. P.; Katsonis, N., Conversion of light into macroscopic helical motion. *Nat. Chem.* **2014,** *6* (3), 229-235.
17.Ware, T. H.; McConney, M. E.; Wie, J. J.; Tondiglia, V. P.; White, T. J., Voxelated liquid crystal elastomers. *Science* **2015,** *347* (6225), 982-984.

18.White, T. J.; Broer, D. J., Programmable and adaptive mechanics with liquid crystal polymer networks and elastomers. *Nat. Mater.* **2015,** *14* (11), 1087-1098.
19.Na, J.-H.; Evans, A. A.; Bae, J.; Chiappelli, M. C.; Santangelo, C. D.; Lang, R. J.; Hull, T. C.; Hayward, R. C., Programming Reversibly Self-Folding Origami with Micropatterned Photo-Crosslinkable Polymer Trilayers. *Adv. Mater.* **2015,** *27* (1), 79-85.
20.Liu, Y.; Shaw, B.; Dickey, M. D.; Genzer, J., Sequential self-folding of polymer sheets. *Sci. Adv.* **2017,** *3* (3).
21.Park, S.-J.; Gazzola, M.; Park, K. S.; Park, S.; Di Santo, V.; Blevins, E. L.; Lind, J. U.; Campbell, P. H.; Dauth, S.; Capulli, A. K.; Pasqualini, F. S.; Ahn, S.; Cho, A.; Yuan, H.; Maoz, B. M.; Vijaykumar, R.; Choi, J.-W.; Deisseroth, K.; Lauder, G. V.; Mahadevan, L.; Parker, K. K., Phototactic guidance of a tissue-engineered soft-robotic ray. *Science* **2016,** *353* (6295), 158-162.
22. O'Neill, B., *Elementary Differential Geometry*. Academic Press, New York: 1997.
23.do Carmo, M. P., *Differential Geometry of Curves and Surfaces*. Dover Publications, New York: 2016.
24.Forterre, Y.; Skotheim, J. M.; Dumais, J.; Mahadevan, L., How the Venus flytrap snaps. *Nature* **2005,** *433* (7024), 421-425.
25.Goriely, A.; Ben Amar, M., Differential Growth and Instability in Elastic Shells. *Phys. Rev. Lett.* **2005,** *94* (19), 198103.
26.Dervaux, J.; Ben Amar, M., Morphogenesis of Growing Soft Tissues. *Phys. Rev. Lett.* **2008,** *101* (6), 068101.
27.Liang, H.; Mahadevan, L., Growth, geometry, and mechanics of a blooming lily. *Proc. Natl. Acad. Sci. U. S. A.* **2011,** *108* (14), 5516-5521.
28.Studart, A. R., Biologically Inspired Dynamic Material Systems. *Angew. Chem., Int. Ed.* **2015,** *54* (11), 3400-3416.
29.Käpylä, E.; Delgado, S. M.; Kasko, A. M., Shape-Changing Photodegradable Hydrogels for Dynamic 3D Cell Culture. *ACS Appl. Mater. Interfaces* **2016,** *8* (28), 17885-17893.
30.Nawroth, J. C.; Lee, H.; Feinberg, A. W.; Ripplinger, C. M.; McCain, M. L.; Grosberg, A.; Dabiri, J. O.; Parker, K. K., A tissue-engineered jellyfish with biomimetic propulsion. *Nat. Biotechnol.* **2012,** *30* (8), 792-797.
31.Roche, E. T.; Horvath, M. A.; Wamala, I.; Alazmani, A.; Song, S.-E.; Whyte, W.; Machaidze, Z.; Payne, C. J.; Weaver, J. C.; Fishbein, G.; Kuebler, J.; Vasilyev, N. V.; Mooney, D. J.; Pigula, F. A.; Walsh, C. J., Soft robotic sleeve supports heart function. *Sci. Transl. Med.* **2017,** *9* (373).
32.Ko, H.; Javey, A., Smart actuators and adhesives for reconfigurable matter. *Accounts of chemical research* **2017,** *50* (4), 691-702.
33.Ionov, L., Biomimetic Hydrogel-Based Actuating Systems. *Adv. Funct. Mater.* **2013,** *23* (36), 4555-4570.
34.van Rees, W. M.; Vouga, E.; Mahadevan, L., Growth patterns for shape-shifting elastic bilayers. *Proc. Natl. Acad. Sci. U. S. A.* **2017,** *114* (44), 11597-11602.
35.Klein, Y.; Venkataramani, S.; Sharon, E., Experimental study of shape transitions and energy scaling in thin non-Euclidean plates. *Physical review letters* **2011,** *106* (11), 118303.
36.Dias, M. A.; Hanna, J. A.; Santangelo, C. D., Programmed buckling by controlled lateral swelling in a thin elastic sheet. *Physical Review E* **2011,** *84* (3), 036603.

37.Na, J.-H.; Bende, N. P.; Bae, J.; Santangelo, C. D.; Hayward, R. C., Grayscale gel lithography for programmed buckling of non-Euclidean hydrogel plates. *Soft Matter* **2016,** *12* (22), 4985-4990.
38.Efrati, E.; Sharon, E.; Kupferman, R., Elastic theory of unconstrained non-Euclidean plates. *Journal of the Mechanics and Physics of Solids* **2009,** *57* (4), 762-775.
39.Gladman, A. S.; Matsumoto, E. A.; Nuzzo, R. G.; Mahadevan, L.; Lewis, J. A., Biomimetic 4D printing. *Nature materials* **2016**.
40. Cangialosi, A.; Yoon, C.; Liu, J.; Huang, Q.; Guo, J.; Nguyen, T. D.; Gracias, D. H.; Schulman, R., DNA sequence-directed shape change of photopatterned hydrogels via high-degree swelling. *Science* **2017,** *357* (6356), 1126-1130.
41.Bowman, C. N.; Kloxin, C. J., Toward an enhanced understanding and implementation of photopolymerization reactions. *AIChE Journal* **2008,** *54* (11), 2775-2795.
42.Winter, H. H.; Chambon, F., Analysis of Linear Viscoelasticity of a Crosslinking Polymer at the Gel Point. *J. Rheol.* **1986,** *30* (2), 367-382.
43.Rodd, A. B.; Cooper-White, J.; Dunstan, D. E.; Boger, D. V., Gel point studies for chemically modified biopolymer networks using small amplitude oscillatory rheometry. *Polymer* **2001,** *42* (1), 185-198.
44.Zhou, H.; Johnson, J. A., Photo-controlled Growth of Telechelic Polymers and End-linked Polymer Gels. *Angew. Chem., Int. Ed.* **2013,** *52* (8), 2235-2238.
45.Chen, M.; Zhong, M.; Johnson, J. A., Light-Controlled Radical Polymerization: Mechanisms, Methods, and Applications. *Chem. Rev.* **2016,** *116* (17), 10167-10211.
46.Pan, X.; Fang, C.; Fantin, M.; Malhotra, N.; So, W. Y.; Peteanu, L. A.; Isse, A. A.; Gennaro, A.; Liu, P.; Matyjaszewski, K., Mechanism of Photoinduced Metal-Free Atom Transfer Radical Polymerization: Experimental and Computational Studies. *J. Am. Chem. Soc.* **2016,** *138* (7), 2411-2425.
47.Matyjaszewski, K., Advanced materials by atom transfer radical polymerization. *Advanced Materials* **2018,** *30* (23), 1706441.
48.Sharon, E.; Efrati, E., The mechanics of non-Euclidean plates. *Soft Matter* **2010,** *6* (22), 5693-5704.
49. Kamata, H.; Akagi, Y.; Kayasuga-Kariya, Y.; Chung, U.-i.; Sakai, T., "Nonswellable" Hydrogel Without Mechanical Hysteresis. *Science* **2014,** *343* (6173), 873-875.
50.Müller, M. M.; Amar, M. B.; Guven, J., Conical defects in growing sheets. *Physical review letters* **2008,** *101* (15), 156104.
51.Seffen, K. A., Fundamental conical defects: The d-cone, its e-cone, and its p-cone. *Physical Review E* **2016,** *94* (1), 013002.
52.Blevins, E. L.; Lauder, G. V., Rajiform locomotion: three-dimensional kinematics of the pectoral fin surface during swimming by freshwater stingray *Potamotrygon orbignyi*. *J. Exp. Biol.* **2012,** *215*, 3231-3241.
53.Fratzl, P.; Barth, F. G., Biomaterial systems for mechanosensing and actuation. *Nature* **2009,** *462* (7272), 442-448.
54.Xu, S.; Yan, Z.; Jang, K.-I.; Huang, W.; Fu, H.; Kim, J.; Wei, Z.; Flavin, M.; McCracken, J.; Wang, R.; Badea, A.; Liu, Y.; Xiao, D.; Zhou, G.; Lee, J.; Chung, H. U.; Cheng, H.; Ren, W.; Banks, A.; Li, X.; Paik, U.; Nuzzo, R. G.; Huang, Y.; Zhang, Y.; Rogers, J. A., Assembly of

micro/nanomaterials into complex, three-dimensional architectures by compressive buckling. *Science* **2015,** *347* (6218), 154-159.
55.Johnson, A. E.; Hebert, M., Using spin images for efficient object recognition in cluttered 3D scenes. *IEEE Transactions on pattern analysis and machine intelligence* **1999,** *21* (5), 433-449.

CHAPTER 3

3.1 DIGITAL LIGHT 4D PRINTING OF ROBUST SOLID COMPOSITES

Amirali Nojoomi & Kyungsuk Yum

3.2 ABSTRACT

Printing shape evolving structures, known as four-dimensional (4D) printing, has opened up new opportunities in fabricating complex structures with different functionalities. Amongst a variety of 4D printing technologies, thin elastic 2D plates that undergo lateral differential growth to make programmed 3D surfaces, termed non-Euclidean plates, promise access to a wide array of complex 3D shapes while requiring only a single-layer patterning. However, this method has been mostly limited to soft materials and pneumatic devices, restricting its usage significantly. Here we use a light projection grayscale lithography to create non-Euclidean plates by encoding 2D hydrogels with a pattern of non-uniform lateral growth. While this approach relies on controlled 3D self-shaping of 2D hydrogels in water, we achieved robust air-stable 3D structures using a thermal/chemical shape stabilization process. Using this process, we enhanced the modulus of the formed structures by 10^6 to 10^7 times, while preserving their 3D accuracy. Taking advantage of growth metrics continuity and freedom in the surfaces made by this approach, we showed the shape versatility and accuracy of the solid structures, by encoding the source 2D hydrogels with a wide range of known growth patterns. The absence of moving parts made us able to make composite structures by introducing reinforcing phases to the prepolymer solution, further increasing the mechanical controllability of the solid structures. We also introduced a sequential printing process to create multi-material 3D structures using different prepolymer solution to form distinct areas of structures. Finally, we demonstrated the programmable fabrication of solid 3D structures with non-developable surface morphologies and specific material patterns, which can serve as a new way of customized manufacturing.

3.3 INTRODUCTION

Shape-changing materials with the ability to adopt programmable 3-dimensional (3D) shapes and motions, known as 4D printing, offer promise for a wide range of applications including, smart textiles[1], soft robotic[2-4], actuators[5-6], shape-changing sensors[7], microfluidic valves[8-9], optical systems [10-11], artificial muscles[12-13], and metrics for bio-separation[13]. Controlled deformation of thin plates, into programmed 3D surfaces, as a form of 4D printing[14], have shown a great potential for the design of complex geometries, hard to achieve with other methods. [15-17]Such methods potentially offer the scalability of the traditional forming processes with the customizability of additive manufacturing. The most straightforward approach is creating a bending configuration in a planar surface by forming a bilayer structure made of materials with different growth (expansion/contraction) rates [18-19] or directions [20-22]or inducing a growth gradient along the thickness of a thin sheet.[23-24] While these approaches often lead to the formation of surfaces with constant and single curvatures, they fail to make shapes with continuous curvature change or doubly curved 3D shapes, significantly limiting the attainable geometries. Therefore, alternative methods offering access to a broader range of shapes has been in the center of attention in recent years, amongst which forming non-Euclidean plates is the most widely used[25-27]. In this approach, controlled in-plane differential growth (swelling/shrinkage) in a thin elastic plate causes out-of-plane deformation and forms a programmed 3D shape[28]. This method offers access to a broader array of shapes with non-zero mean and Gaussian curvatures, while it requires patterning of only a single material layer. However, so far, the formation of non-Euclidean surfaces has been mostly limited to soft materials[20, 25-27] or pneumatic devices [29-30] with low mechanical properties, limiting the potential applications.

Recently, we introduced an approach to create non-Euclidean plates by preparing temperature-responsive thin flat hydrogels, encoded with a spatially controlled network density and thus lateral growth (Ω). The non-uniform growth defines a new surface metric tensor , the "target metric", which causes a controlled out-of-plane buckling and results in a specific three-dimensional hydrogels with specific morphologies.[28]

To broaden the application of such 3D surfaces beyond aqueous environment, in this study, we describe a solidification strategy to form 3D solid surfaces by stabilizing the formed 3D hydrogels at ambient environment (Figure 3-1**a,b**). Due to the high-water content, solidification of hydrogels while preserving their shape has been a challenge. Specially for most non-Euclidean hydrogel systems, differential water content throughout the sample induces the non-uniform lateral growth which results to 3D shape formation. Therefore, water removal will collapse the 3D structure back to the flat state[20, 26]. However, uniquely to our material system, 3D configurations of the hydrogel develop in both swelled ($T<T_C$) and shrunk ($T>T_C$) states (T_C ~32.5 °C) due to difference in cross-linking and network density, respectively (Figure 3-1**c**). Independency of the growth to the water content combined with overall low internal water of 3D structures at the shrunk state makes hydrogels easier to solidify while preserving the morphology. The fast processing combined with an on-demand 3D self-formation of non-Euclidean solid surfaces makes our approach ideal for scalable and customizable fabrication of hinge-free deployable, robust 3D structures with complex morphologies.

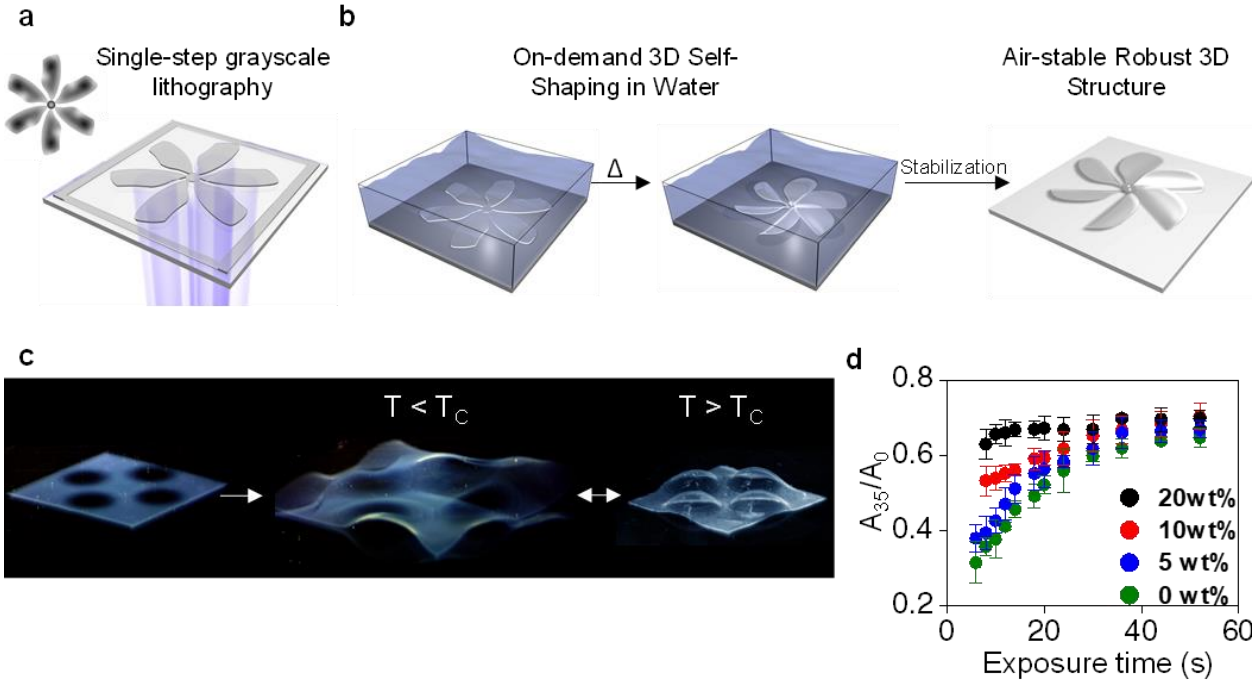

Figure 3-1 **Digital Light 4D Processing of solid 3D structures. a** Schematic illustration of the grayscale lithography. A 2D hydrogel is created from a liquid precursor while being encoded with growth function Ω through grayscale photo-lithography. The inset is the digitally made grayscale light pattern exposed to the precursor via a commercial projector. **b** Schematic illustration of the temperature-induced shape transformation of a 2D hydrogel to the target 3D shape in the water. The formed 3D structure is then stabilized to create robust solid structures in the ambient environment. **c** Experimental demonstration of a programmed 2D hydrogel transforming to the prescribed 3D shape at the swelled state upon immersion in water ($T < T_c$), where T_c is the volume phase transition temperature of the hydrogel (~32.5 °C). The 3D structure at the swelled state reversibly transforms to the target 3D shape at the shrunk state upon temperature increase ($T > T_c$). **d** Areal shrinking ratios (A_{35}/A_0) of dual-crosslinked pNIPAm hydrogels versus light exposure time for hydrogels made from precursors with different concentrations of solid particles. A_{35} is the area of the hydrogel at 35°C, and A_0 is the area of the as-prepared hydrogel. Error bars: s.d. of three independent measurements.

3.4 RESULTS

3.4.1 Digital Light 4D Processing of composite structures

The programmable precursor solution consists of NIPAm monomer as the building block of the temperature-responsive network and two crosslinkers (PEGDA and BIS) with different molecular weights to increase the photo-tunable density and thus growth range over the wide range of light exposure time (Figure 3-1**d**).[31] The absence of the moving parts eases the specific ink requirements and makes our method adaptable to variety of inks with different rheological properties. Building on this capability, we created composite hydrogels by introducing a wide range of reinforcing phases to the base precursor before printing.

Extracting the relationship between the photo-polymerization exposure time and the hydrogel shrinkage is essential for encoding hydrogels with specific growth patterns Ω. To explore the impact of the reinforcing phase on the shrinkage of the hydrogels, we first studied the temperature-activated growth (shrinking) behavior of the hydrogels at temperatures over the volume phase transition temperature Tc (~32.5 °C), prepared from precursors with 0, 5, 10, and 20 wt% silica particles as the reinforcing material (Figure 3-1**d**). As expected, the existence of a non-shrinkable phase in the hydrogel network increases the shrinking ratio (A_{35}/A_0) by occupying the free spaces between the polymer chains and hindering the network chain collapse.[32] More importantly, the shrinkage limitation is more dominant for low-density hydrogels, made at short light exposure, due to the higher solid to polymer ratios, which causes a decrease in the attainable shrinking range with the increase in solid loading.

3.4.2 Geometrical limitation and shape Accuracy

Primary shapes with constant positive (spherical cap), negative (saddle) and zero (truncated cone) gaussian curvatures K, were made by encoding $\Omega_{cap} = \Omega_{max}/(1 + (r/R)^2)^2$, $\Omega_{saddle} = \Omega_{min}/(1 - (r/R)^2)^2$, and $\Omega_{cone} = \Omega_{min}\ (r/R)^{2(\alpha-1)}$ growth patterns, written in terms of the circular coordinates on a flat, as-printed pure and composite gel sheets. Here, r/R is the normalized radial coordinate, α is a constant, and Ω_{max} and Ω_{min} are the maximum and the minimum shrinking ratios, respectively (Figure 3-2**a,b**). Since the non-uniform growth induced stretching and bending energies scale differently with the thickness ($E_s \propto t$ and $E_b \propto t^3$)[28], it is expected that the buckling configuration and thus out-of-plane deformation happens at specific geometries with $R/t > (R/t)_c$, where t is the thickness. To check the geometrical limitation of our system, we created spherical cap structures, with different lateral sizes and a fixed thickness (t≈400 μm). Our results show that printing sizes with $(R/t)_c > 12.5$ makes samples adopt bending-dominated configuration and form a perfect spherical cap, which is an embedding of the target metric at the stretch-free configuration (Figure 3-2**c**). To further understand the level of accuracy, we investigated the compliance of structures' specific features with the theoretical calculations. For example, the vertex angles of the truncated cones made at different exponents α, show a good match to the programmed value of the deficit angle δ ($\delta = 2\pi(1-\alpha)$)[31] (Figure 3-2**d-f**).

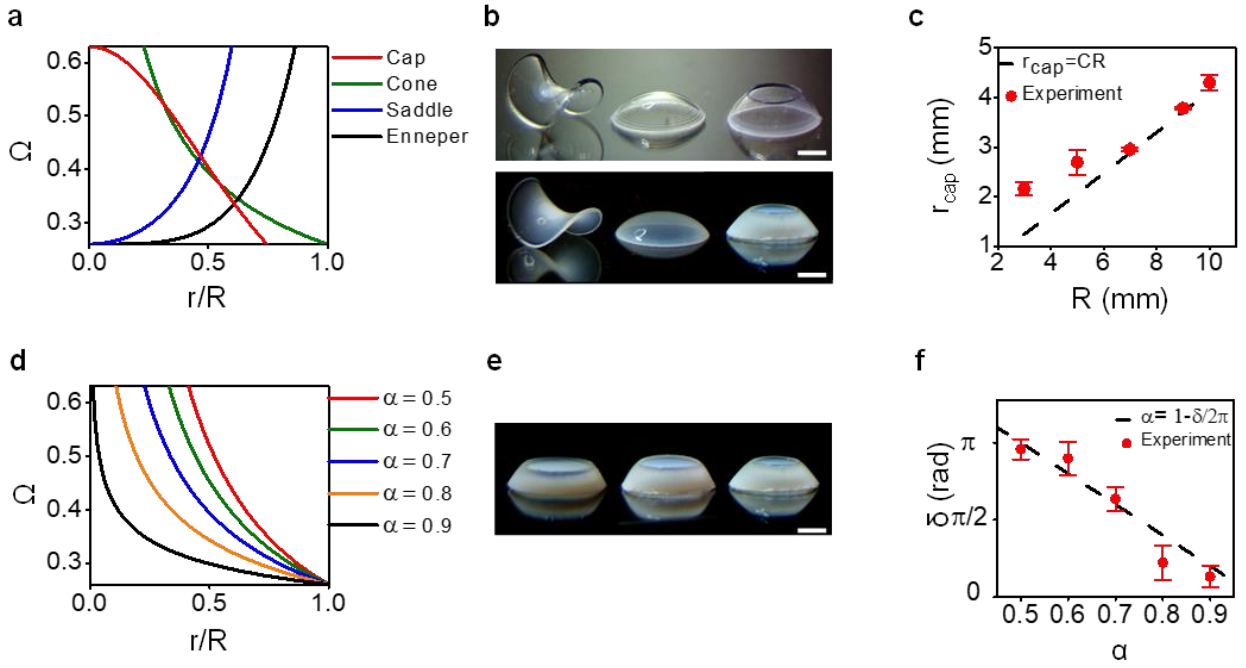

Figure 3-2 **a** Axis-symmetric growth pattern Ω used to form the primary shapes with constant positive (cap), negative (saddle) and zero (cone) Gaussian curvatures and an Enneper's minimal surface with three nodes. **b** Primary shapes made from pure precursor (top) and a precursor with 5 wt% silica (bottom) Scale bar is 2mm. **c** Experimental (solid circles) and theoretical (dashed line) values of spherical cap radius (r_{cap}) printed with different printing radius R in Ω. Constant C is $\Omega_{max}/4$. **d** Axis-symmetric growth pattern Ω with different α used to form cone structures with different deficit angles (δ). **e** Truncated cones with α=0.5,0.6 and 0.7 from a precursor with 5 wt% silica (bottom). Scale bar is 2mm. **f** Experimental (solid circles) and theoretical (dashed line) values of deficit angle δ with different α in Ω for cone structures.

3.4.3 Solidification process

The solidification process relies on the ability to form target 3D structures at the shrunk state. As an example, we encoded a flat composite hydrogel (5% silica) with a growth pattern of $\Omega = \Omega_{min}(1 + (r/R)^4)^2$ (Figure 3-2**a**), associated with an Enneper's minimal surface with three nodes. [26, 31] Here, r/R is the normalized radial coordinate, and Ω_{min} is the minimum shrinking ratio.

The programmed flat hydrogel is then swelled in a water environment at $T<T_C$ (Figure 3-3**a**) to be removed from unreacted monomers and oligomers. This step provides molecular free-space for the hydrogel chains to shrink freely at $T<T_C$ and form the target 3D shape at a shrunk state.

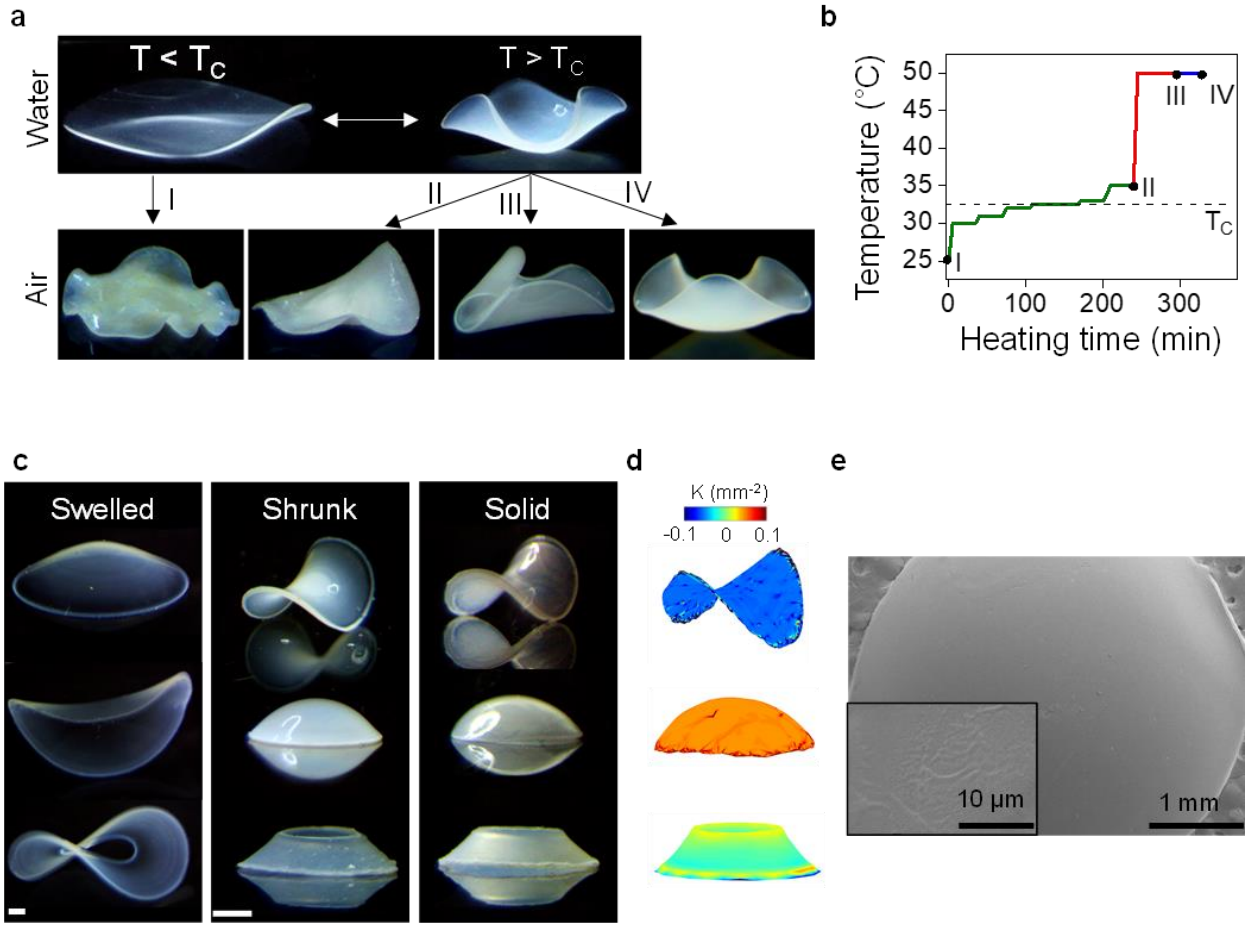

Figure 3-3 **Solidification process. a** Formation of a solid structures. The top panel shows a composite hydrogel encoded with a growth pattern corresponding to an Enneper's surface in swelled ($T < T_C$) and shrunk ($T < T_C$) states. The bottom panel shows the morphology of the hydrogels upon removal from water at different states. **b** Thermal/chemical process used to form a solid 3D structure from a swelled hydrogel (I). Slow temperature increase from room temperature to over Tc (~32.5C) to form target 3D shapes at the shrunk state (II). Increasing the temperature well beyond Tc to further exclude the internal water of the hydrogel in shrunk state (III). Introducing ions to the solution to achieve stable 3D shape before removal from water (IV). **c** Composite disks programmed to generate shapes with constant Gaussian curvature (K) at swelled (left panel), deswelled (middle panel), and solid (right panel) states. Reconstructed 3D images of

the solid structures with Gaussian curvature colormap (Scale bars, 2mm). **d** SEM surface image of the stabilized cap at solid state.

Figure 3-3**b** shows the thermal/chemical process used to form a solid 3D structure from a hydrogel at a swelled state. The first step is to 3D form the target structures at a shrunk state by increasing the temperature of a swelled hydrogel over T_C (~32.5C) (Figure 3-3**a**). A gradual temperature increase is required to avoid the formation of a dense skin layer, which prevents the exchange of water molecules between the hydrogel and the surrounding. While 3D structures at swelled state are not stable outside the aqueous environment (I in Figure 3-3**a**) due to the necessity of water in forming the 3D morphology (Figure 3-4**a**), structures at shrunk state are thermodynamically free of water.[33] However, the remaining structural water at the shrunk state (Figure 3-4**b**) can still deform the samples upon environmental exchange from water to the air (II in Figure 3-3**a**). To exclude this residual water, we raised the temperature of the samples well above the T_C (~20 °C) to further increase the free energy of hydration[33]. However, even at the full exclusion of structural water, the remaining surface water can still deform the structure once it cools down to $T<T_C$ at air (III in Figure 3-3**a**). One can solve this problem by further increasing the temperature to keep the surface temperature higher than T_C before blotting the surface water. However, this would be hard to achieve for big samples or samples with complex geometries. Therefore, we instead introduced the samples to a near-saturated ionic aqueous solution (~20 w/v saline water) to sharply decrease the T_C and maintain the hydrogel at shrunk state even at room temperature.[34] The samples were then safely transferred to the ambient environment and formed air-stable solid structures with the same shape accuracy of the original shapes at the shrunk state (IV in Figure 3-3**a** and Figure 3-4**c**). Figure 3-3**c** shows cap, saddle, and cone structures at swelled,

shrunk, and solid states, respectively. To investigate the shape accuracy of the solid samples, we scanned and measured the Gaussian curvature profiles (K) (Figure 3-3**d**), which show excellent agreement with the expected constant curvature data for all three shapes. Also, the absence of texture discontinuity in the solid surfaces (Figure 3-3**e**), which is a result of the continuous forming process, eliminates the need for post-processing, thus further increases the overall fabrication speed. Shapes at both shrunk and solid states retained their programmed 3D configuration for months in water ($T > T_C$) and ambient environment, respectively. To avoid shape distortion due to the water spillage or high humidity, we coated the solid samples with a protective-layers of PDMS and paint (Figure 3-4**d**).

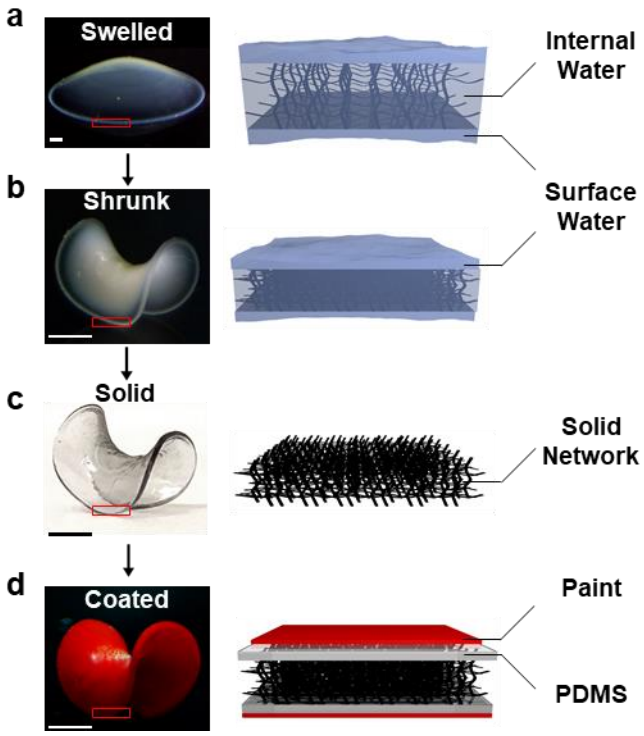

Figure 3-4 **a-d**) 3D structures of a sample encoded with Ω_{saddle} at swelled state (**a**), shrunk state (**b**), solid state (**c**), and coated solid (**d**). Left panels are the schematic illustration of the internal structure. Scale bar 2mm.

3.4.4 Mechanical Properties of structures at different states

The absence of structural water significantly enhances the mechanical behavior of the solid structures compared to the hydrogels in both swelled and shrunk states. To understand the difference, we first study the mechanical behavior of the hydrogels in both swelled and shrunk states. The dynamic shear analysis shows that the hydrogels at shrunk state have higher and more consistent modulus (~2 kPa) compared to those in the swelled state (~0.05 to 0.5kPa), which attributes to their internal structure. While the modulus of the swelled hydrogels are mostly controlled by the degree of cross-linking [35] and thus the light exposure time during polymerization, the same hydrogels at shrunk state show higher and more similar modulus due to their dense and collapsed molecular structure (Figure 3-5**a**). On the other hand, solid structures show significantly higher modulus ~2 GPa (Figure 3-5**b**), which can be related to the plasticizing role of water molecules [36]. The tensile behavior difference between the hydrogels in shrunk state and solid structures further indicates the role of water as a plasticizer in decreasing the glass transition temperature (Tg). The shrunk hydrogels show rubbery behavior (Tg << 32.5°C) (Figure 3-6) with an elastic strain of ~ 500% (Figure 3-5**c**) while the solid samples mostly show fully brittle fracture (Tg >> 32.5°C) with the strain of < 5% (Figure 3-5**b,d** and Figure 3-7**b**). The solid samples, therefore, can withstand loads hundreds of times larger their own weights (Figure 3-5**e**).

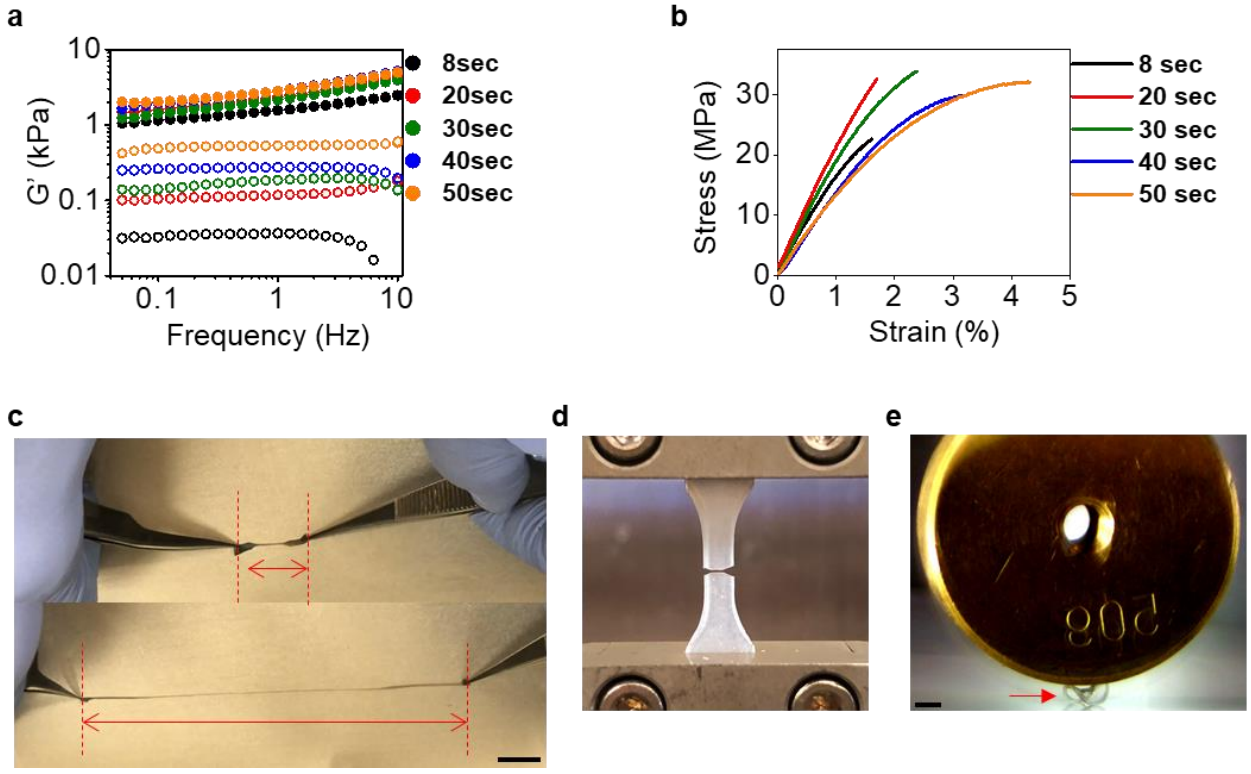

Figure 3-5 **Mechanical properties. a** Dynamic oscillatory shear measurement of the hydrogels at swelled (hollow dots) and shrunk (solid dots) states. **b** Tensile behavior of the solid samples prepared with different light exposure times. **c** Elastomeric behavior demonstration of a hydrogel at shrunk state. The sample is prepared at 8 sec light exposure time. scale bar is 2cm. **d** Brittle fracture of a composite sample made from 5 wt% silica precursor at 20 sec light exposure time. **e** Experimental demonstration of a solid sample withstanding loads about hundred times its weigh. scale bar is 2mm.

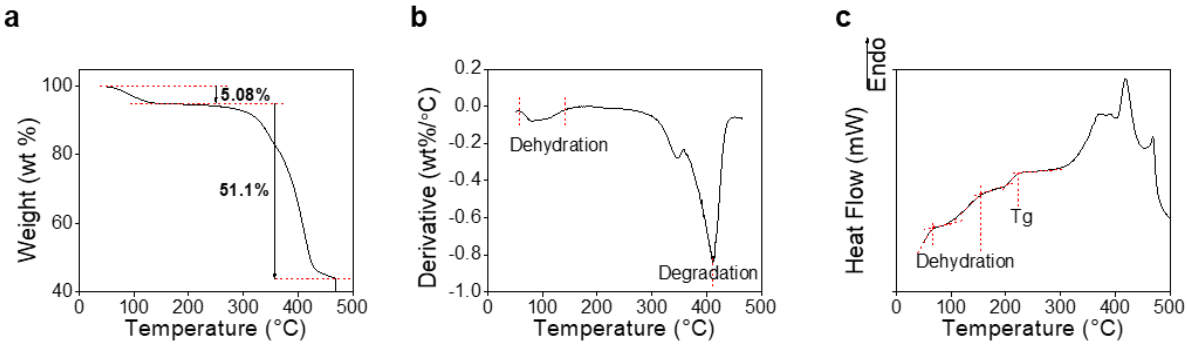

Figure 3-6 **a** Thermal Gravimetric Analysis (TGA) of the solid sample form 50°C to 500 °C. **b** First derivative of the wight change in respect to temperature. **c** Differential Scanning Calorimetry of the solid structures showing Tg ~ 230 °C.

We showed improvements in the hardness of the solid samples adding silica reinforcing phases to the precursor (Figure 3-7**c**). Since all solvents are removed throughout the deswelling and ultimately at the shape stabilization process, the final concentration of Silica in the composite samples are 14.75, 25.71, and 40.9 wt%. Unlike our method, the processability of precursors in other projection-based systems is often limited by the rheological behavior, making such high concentrations of reinforcing phases unachievable. [37]

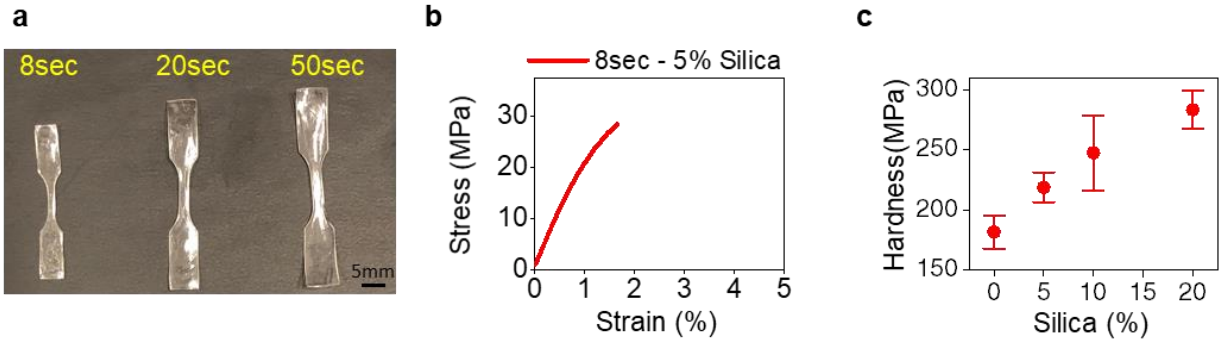

Figure 3-7 **a** Air stabilized samples prepared at 8 sec, 20 sec, and 50 sec light exposure for tensile study. Scale bar is 5 mm. **b** Tensile behavior of the sample in Figure 3-5d. **c** Vickers hardness of the samples made from precursors with 0,5,10 and 20 wt% of silica

3.4.5 Solid structures with diverse metrics

Our method can create solid 3D structures with various geometries. To validate the accuracy and precision of the patterned metrics, we encoded hydrogels with $\Omega = \Omega_{max}/(1 + (r/aR)^2)^2 + (1 + (r/R)^n)^2 - c$, corresponding to Enneper's minimal surface with n nodes and a cap-like center [31] (Figure 3-8 **a**). Including a cap-like geometry (K > 0) in the middle of an Enneper's surface with (K < 0), reduces the portion of the metric governed by the Enneper's metric (Figure 3-8**a**). Despite this reduced control and given subtle differences between Enneper's part of the metric plotted in Figure 3-8a, the number of the wrinkles in the resulting structures agree quantitatively with the targeted number of nodes programmed through Ω [26] (Figure 3-8**b**). Such accuracy is strong proof of the precision of the metrics patterned by our method.

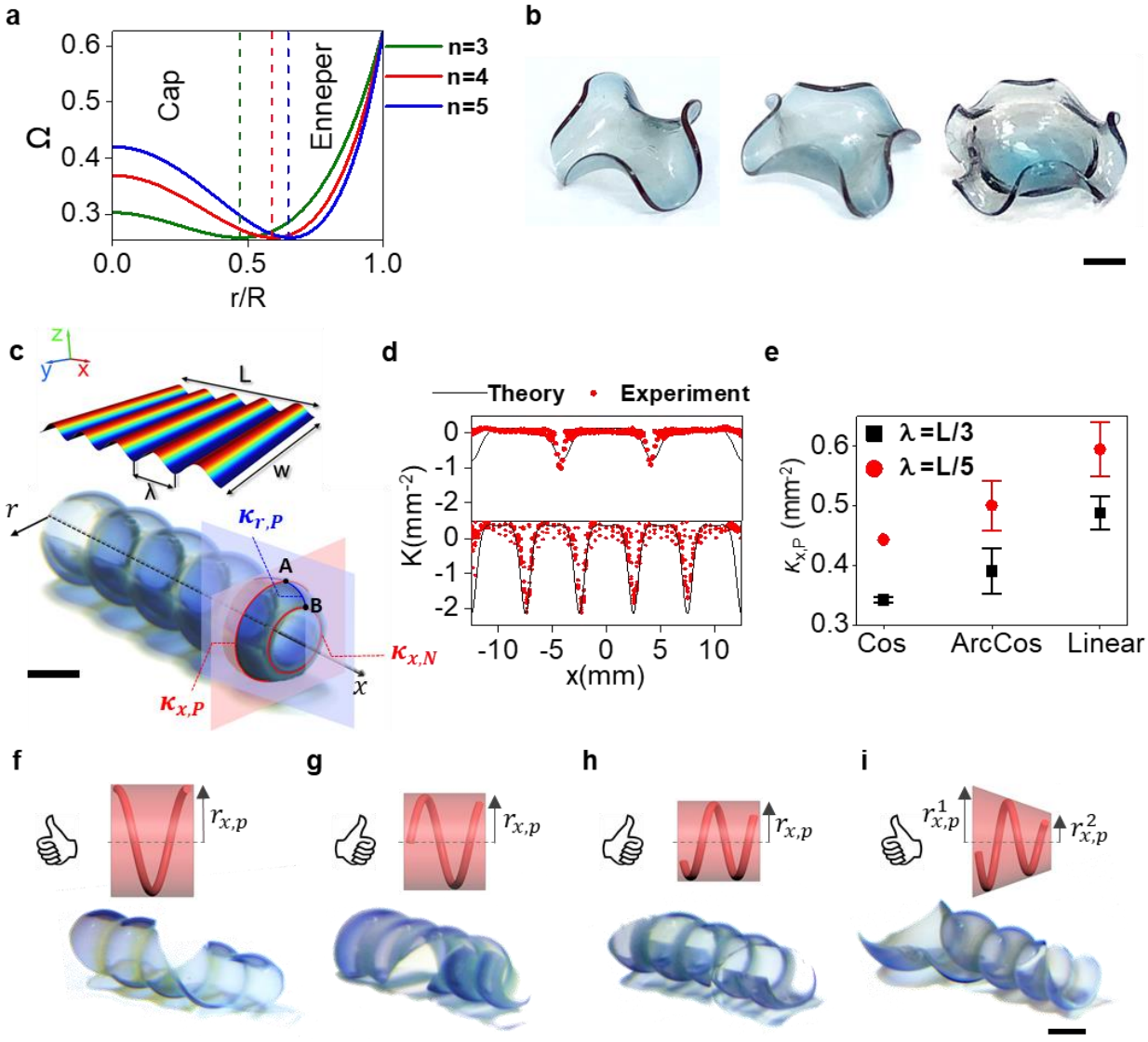

Figure 3-8 **Creating diverse 3D geometries with high accuracy. a** Axis-symmetric growth pattern Ω corresponding to Enneper's minimal surface with n nodes and a cap like center. **b** Solid 3D shapes created based on Ω in (A) with n=3, 4 and 5 from left to right, respectively. scale bar is 2mm. **c** Growth pattern Ω (top) and 3D structure of a sample formed from a 10mmx25mm stripe encoded with a single direction Ω with cosine function. $\kappa_{x,P}$ and $\kappa_{r,P}$ are principle curvatures of point A (Positive Gaussian curvature) on the intersecting planes perpendicular to x and r axis, respectively. $\kappa_{x,N}$ is the principle curvature of point B (Negative Gaussian curvature) on the plane perpendicular to r axis. scale bar is 2mm. **d** Experimental (solid dots) and theoretical (solid line) values of the gaussian curvature ($K= \kappa_x . \kappa_r$) as a function of x for structures formed with Ω in (**c**)

at L/w=2.5 with λ=L/3 and L/5. **e** The average $\kappa_{x,P}$ for the structures formed with cosine, alternative arccosine and alternative linear Ω functions in Figure 3-10, Supporting Information. Error bars: s.d. of at least three independent measurements. **f-i** Schematic of turns and handedness (top) and the real images of the air stable helical structures (bottom) formed with cosine function with $\theta = 45$ (**f**), alternative arccosine function at $\theta = 135$ (**g**) , alternative linear function at $\theta = 135$ (H), and cosine function with variant λ at $\theta = 135$ (**i**). Scale bars are 2mm.

The freedom of digitally made exposure masks offers the creation of geometric 3D structures with almost any metric. To show the adaptability of our method to make shapes beyond structures with axis-symmetric metrics, we created well-studied rolled sheets patterned with single direction lateral growth patterns (Figure 3-8**c-i** and Figure 3-9). So far, the implementation of such metrics has been limited to stripes with discrete regions where each region seeks to attain a different, discontinuous level of growth.[38-41] The existence of such discontinuities in the boundaries between regions induces stresses in the ground state and prevents the continuous surface from obeying the target metric. On the contrary, implementing continuous smooth growth patterns in our method allows the formation of rolled configurations with the isometric immersion of the target metric, making the shapes more predictable, consistent, and accurate. To theoretically study the rolling deformation, we considered structures formed by single direction growth pattern $\Omega = (\Omega_{max} - \Omega_{min})(\mathrm{Cos}(2\pi\, m(x/L)) + 1)/2 + \Omega_{min}$, where L is the length along the x-direction, and L/m is the growth variation wavelength (Figure 3-8**c**). The sheets adopt an isometric embedding of the target metric by rolling around the x-axis, while each point follows the target Gaussian curvature (K), according to Gauss's Theorema Egregium, $K = -\nabla \ln\Omega/(2\Omega)$ where $K=\kappa_x.\kappa_r$, and κ_x and κ_r are principle curvatures on planes perpendicular to x and r cylindrical axes, respectively (Figure 3-8 **c** and Figure 3-9**a**, Supporting Information). The experimental structures

agree well with the theoretical predictions (Figure 3-8**d,e** and Figure 3-9 **b,c**). For example, Figure 3-8**d** shows the experimentally extracted K as a function of x for the structures made with m=3 and 5, matching well with the predicted curvature function prescribed by the target metric. Such high accuracy suggests a precise control over curvature and, thus, the rolling radius only by controlling the Ω function wavelength. Furthermore, utilizing continuous growth functions offers high-level control over 3D morphology by taking advantage of function and direction modulations.

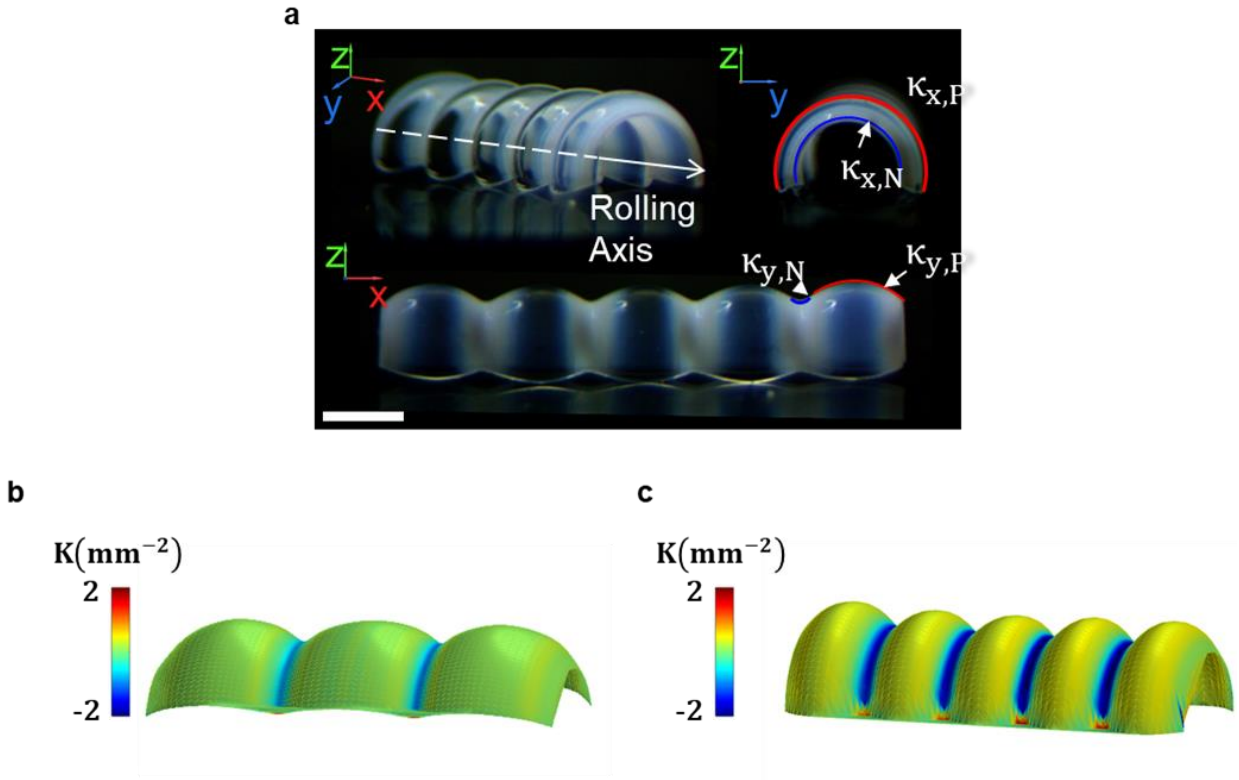

Figure 3-9 **a** A sample made from a 10mmx25mm sheet programmed by cosine Ω function with m=5, showing the general features (Rolling axis, $\kappa_{x,P}$, $\kappa_{x,N}$, $\kappa_{y,P}$, $\kappa_{y,N}$) of a structure patterned with single direction metric variations. Scale bar is 2mm. **b,c** Reconstructed models with Gaussian curvature K colormap for samples formed from 10mmx25mm sheets programmed by cosine function metric with m=3 **b** ,and m=5 **c.**

To show the effect of growth function on the rolling behavior, we created sheets with single direction growth functions following cosine, alternative arccosine, and alternative linear functions with different wavelengths (Figure 3-8**e** and Figure 3-10). We investigated the impact of Ω variation function on the rolling curvature of the structures, by measuring the principal curvature of the points with lowest positive curvature (points with Ω_{max}) on planes perpendicular to the rolling direction, $\kappa_{x,P}$ (Figure 3-8**e**). The results show higher rolling curvature for structures with linear, arccosine, and cosine target metrics, respectively (Figure 3-8**e** and Figure 3-10). In comparison, theoretical calculations suggest higher curvature for arccosine metric compared to linear metric. This discrepancy can be due to the limited 2D printing resolution for replicating the sharp Ω profile at the extremum points (Ω_{max} and Ω_{min}) of the arccosine function, which reduces the attainable curvature in samples made by this function.

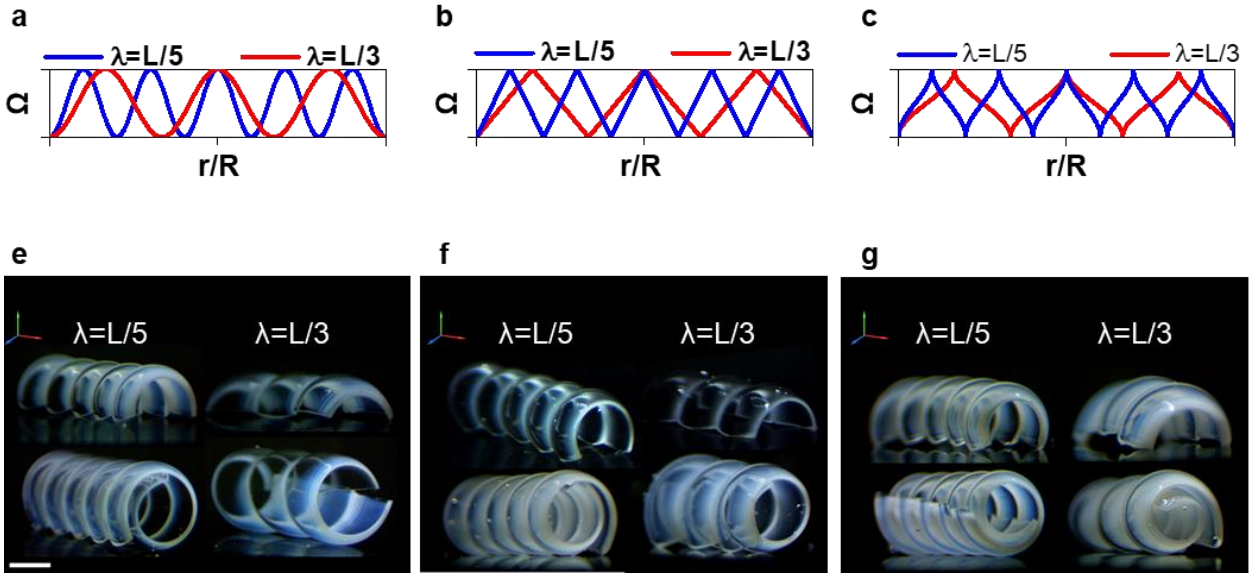

Figure 3-10 **a-c** Single direction cosine **a**, alternating arccosine **b** and alternating linear **c** Ω functions. **e-f** Samples formed from 10mm x 25mm (top) and 25mmx25mm (bottom) sheets programmed by **e** cosine Ω function with m=5 (Left) and m=3 (Right), **f** alternating arccosine Ω function with m=5 (Left) and m=3 (Right), and **g** alternating linear Ω function with m=5 (Left) and m=3 (Right). Scale bar is 2mm.

Having established the procedure to create rolling structures, we applied the same concept to make solid cylindrical and conical helices with specific morphological characteristics. We made helix structures by rotating the function axis and thus the rolling axis to make an oblique angle, θ, with respect to the long axis of the sheet (Figure 3-8 **f-i** and Figure 3-11). Similar to the previous structures, alternation to the Ω, such as base function change, can lead to different rolling curvatures ($\kappa_{x,P}$) and thus different rolling radius ($r_{x,P} = 1/\kappa_{x,P}$) (Figure 3-8**f-i** and Figure 3-11). This control over rolling radius offers control over the number of turns N, and pitch p, in helical structures. For example, samples with cosine, arccosine, and linear functions show N of 1, ~1.2, and ~1.5, respectively. Furthermore, we were able to make a conical helix with gradually

decreasing $r_{x,p}$ by smoothly changing the wavelength of the growth function (Figure 3-8**i** and Figure 3-11**d**). The limited oxygen inhibition due to the presence of PDMS substrate at one side of the printing cell causes a slight variation in density and results in a minor growth (Ω) gradient through the thickness. Although this growth variation has a neglectable impact on the accuracy of the 3D structures, it fixes the direction of the out-of-plane deformation by inducing a slight bending towards the side with less Ω. Taking advantage of this fixed deformation direction, we created helical structures with defined handedness by changing the function direction θ. For example, samples with $0 < \theta < 90$ form right-handed helix (Figure 3-8**f,i** and Figure 3-11**a,d**) while samples with $90 < \theta < 180$ create left-handed helix (Figure 3-8**g,h**, and Figure 3-11**b,c**).

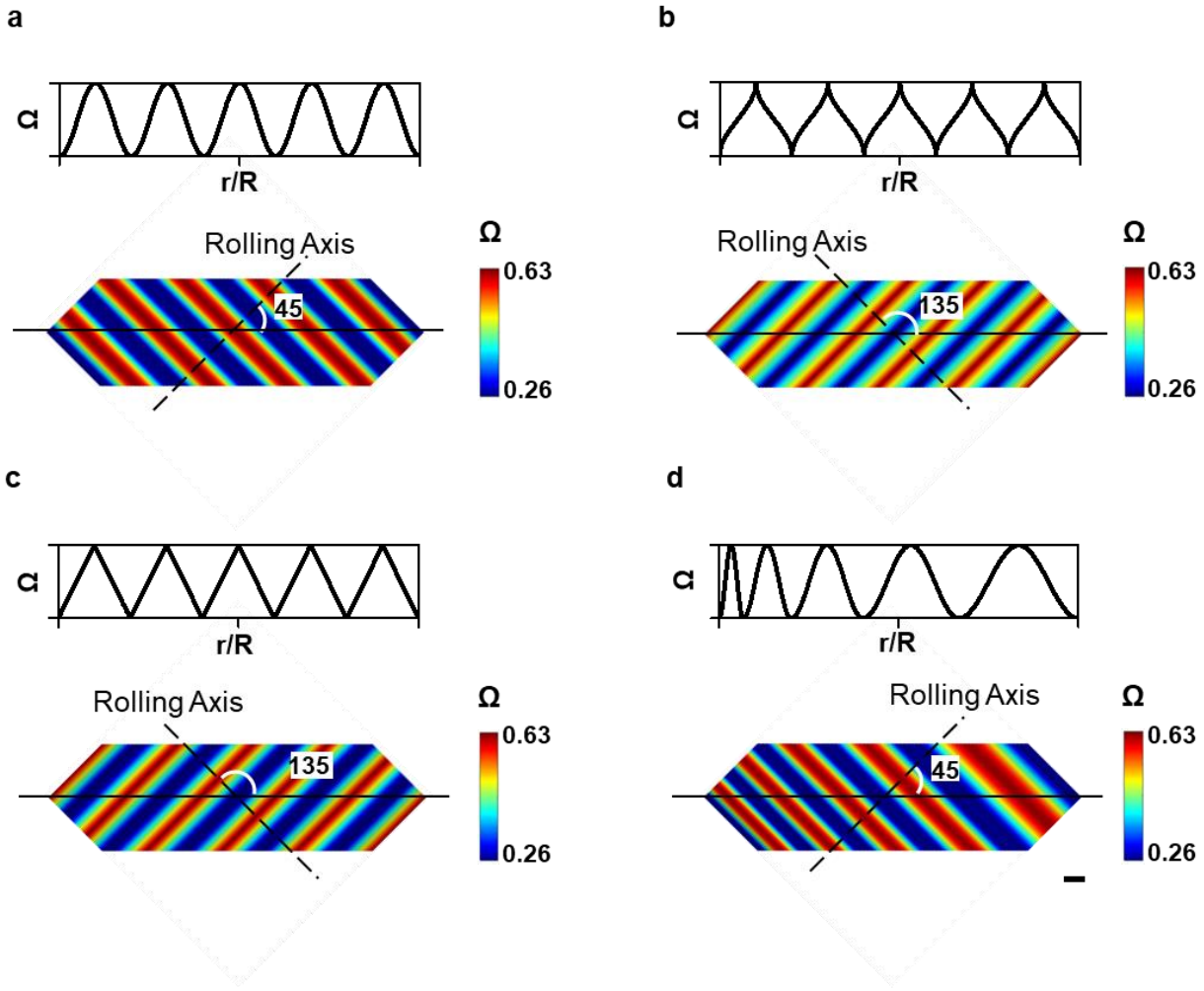

Figure 3-11 **a-d** base function (top panel) and Ω map (bottom panel) used to create helical structures with **a** cosine function metric at m=5 and θ=45. **b** arccosine function metric at m=5 and θ=135, **c** linear function metric at m=5 and θ=135, and **d** cosine function with varying wavelength metric at m=5 and θ=45. Scale bar is 2mm.

To further show the customizability of our process, we printed mathematically defined shapes with arbitrary boundaries (Figure 3-12). Since the 3D formation happens through local (point-to-point) interactions that lead to out-of-plane deformation, any change in the boundary (Figure 3-12**a**) or introducing arbitrary holes (Figure 3-12**b**) would not substantially change the overall shape as long as it does not affect the self-supportiveness of the structure (Figure 3-12**c**).

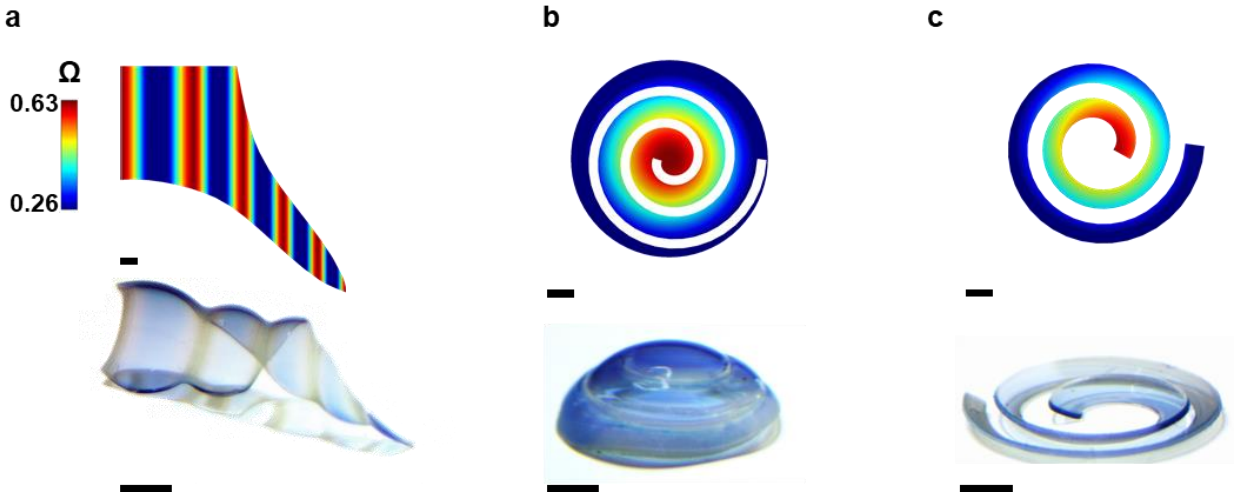

Figure 3-12 Ω map (top) and image (bottom) of **a** solid helical sample made with arbitrary metric boundary of cosine function at m=5 and θ=45, **b** solid spherical cap with spiral internal hollow pattern, **c** solid spherical cap with spiral metric boundary. Scale bars is 2mm.

3.4.6 Multi-Material Printing

This method can build multi-material 3D structures. Creating structures with a continuous texture of different materials is one of the key advantages of additive manufacturing, setting it apart from traditional methods.[42] To show the similar control, we established a multi-step printing procedure, where different precursors form discrete parts of the samples. For example, we made primary shapes with constant positive and constant negative curvatures with material patterns of gold nano-composite and pure polymer (Figure 3-13**a-d**). In the first printing sequence, the gold nano-composite phases are printed using gold added precursor (0.05 g/L gold nano-particles). The rest of the shape is then made from pure precursor at the second step printing. To avoid growth

discontinuity and overexposure, the exposure mask of the second step needs to complete that of the first step to make a full, consistent metric (Figure 3-13**a,b** and Figure 3-14**a)**. However, for high-resolution patterns such as line patterns with ~100 μm line width (Figure 3-13**c,d** and Figure 3-14**b**), that is consisting of several phase boundaries, underexposure at the boundaries causes Ω discontinuity and the appearance of unintended boundary gaps. Therefore, full exposure masks were used in the second-step printing to maintain Ω accuracy and consistency. However, since the line patterns do not follow the target metric, they restrain the full deformation and slightly decrease the overall curvature of the shapes.

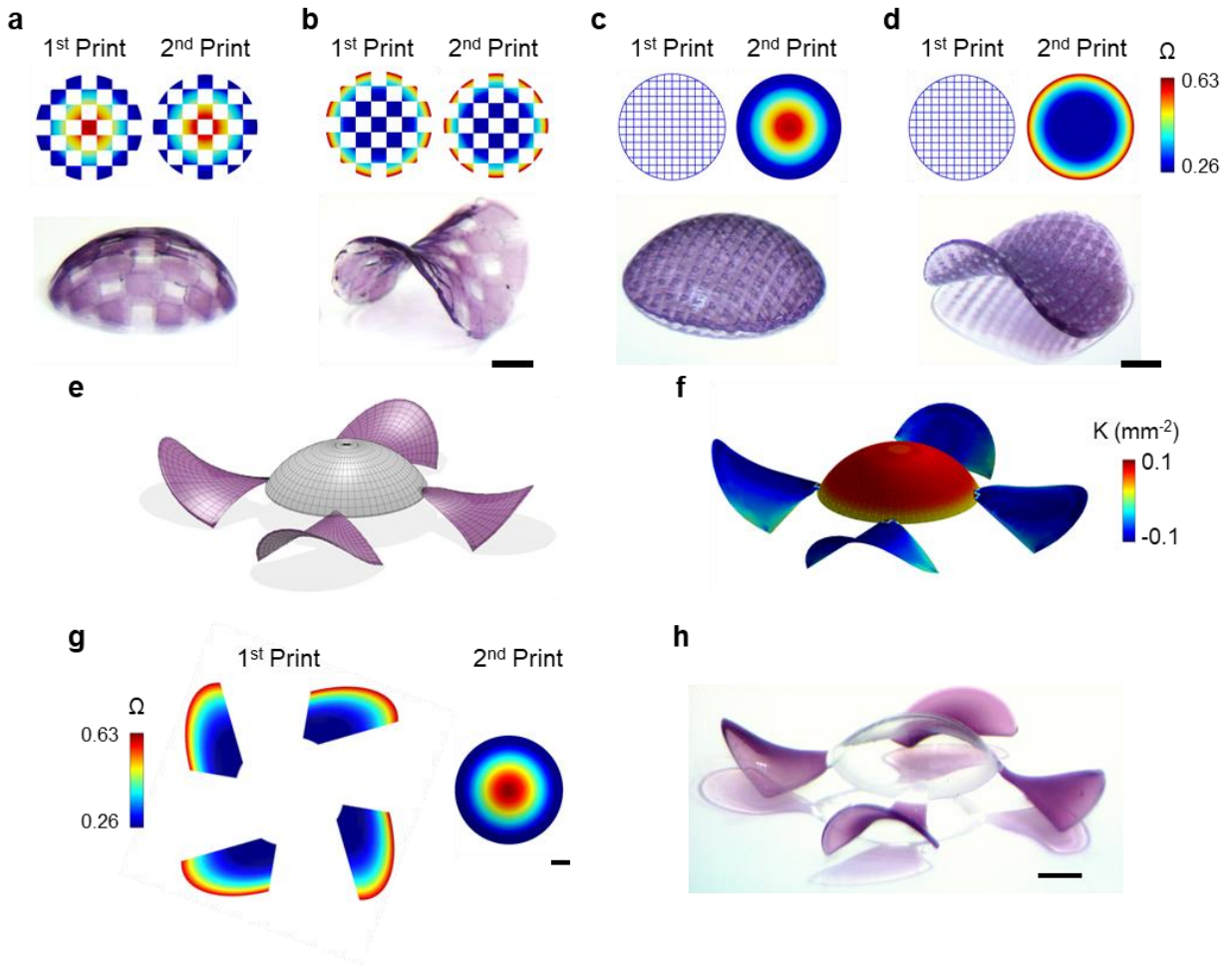

Figure 3-13 Multi-Material Printing. **a,b** Spherical cap **a** and saddle **b** with a checkered pattern of pure polymer and gold-composite regions. Top panel shows associated metrics for two step printing. Gold containing precursor is used to print composite parts at the 1st step. Pure precursor is used to print the rest of the structure at the 2nd step. Bottom panel shows the 3D formed structures at solid state. scale bar is 2mm. **c,d** Spherical cap **c** and saddle **d** with a line pattern of gold-composite in a pure polymer background. Top panel shows associated metrics for two step printing. Gold containing precursor is used to print composite lines (~100 μm) at the 1st step. Pure precursor is used to print the rest of the structure at the 2nd step. Bottom panel shows the 3D formed structures at solid state. scale bar is 2mm. **e** Target 3D model of a propeller with double material pattern. **f** Extracted Gaussian curvature of the target model. **g** Target metrics for 1st step printing (left), and 2nd step printing (right). **h** Final 3D formed solid structure. scale bar is 2mm.

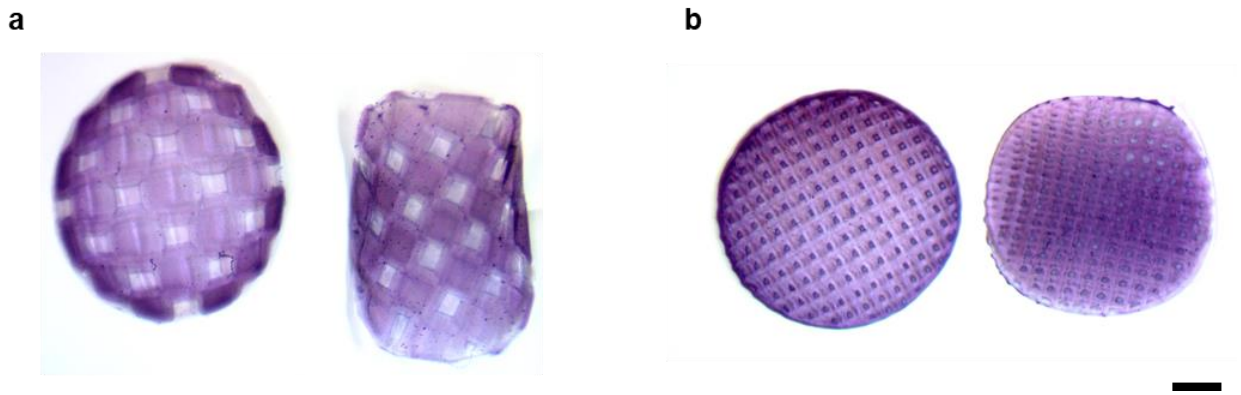

Figure 3-14 **a,b** Top view of the double material structures made by two step printing of **a** the spherical cap (Left) and saddle (Right) structures with checker pattern of gold composite and pure polymer, **b** Spherical cap (Left) and saddle (Right) structures with squire mesh line pattern of gold composite and pure polymer. Scale bar is 2mm.

As an example of the versatility and customizability of this method for making complex solid geometries with on-demand material profiles, we targeted a complex multi-material 3D shape with both negative and positive Gaussian curvatures. We chose a propeller with a four negatively curved ($K < 0$) blades and a cap-like ($K > 0$) center, to be made from gold nano-composite and pure polymer, respectively (Figure 3-13**e**). To design the growth pattern, we extracted the gaussian curvature of the model (Figure 3-13**f**) and replaced each component with a mathematically known metric. For the center component with $K > 0$, the metric function of a spherical cap was used, while for the blades, a portion ($\sim \pi/3$) of an elongated negative component with $\Omega(r/R) = \Omega_{min}/(1-(r/c(\theta)R)^2)^2$ where $c(\theta) = n/\sqrt{1+(n^2-1)Sin^2(\theta)}$, and $n = 0.5$ was used to match the curvature data (Figure 3-13**g** and Figure S11). After designing the metrics, the blades were made at the first step printing using gold added precursor, while the middle was created from the pure precursor at the second printing step. We then used temperature cycling and stabilization process to from air-stable multi-material propeller with perfect shape accuracy (Figure 5H). We

used the same approach to make a stabilized solid helical structure with a material pattern of silica composite and pure polymer phase (Figure S12, Supporting Information).

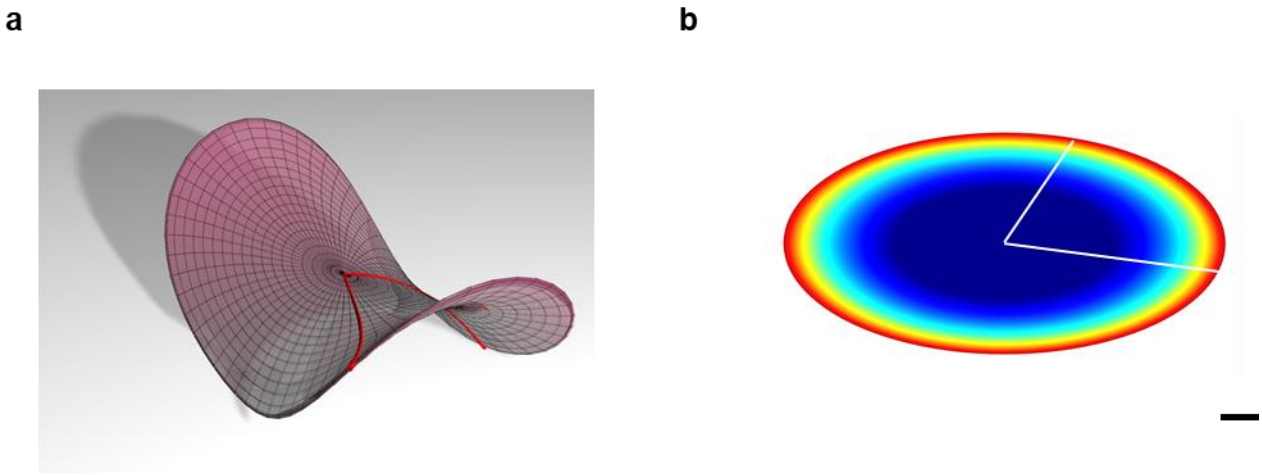

Figure 3-15 **a** 3D model of the elongated saddle used for propeller's blade. Red lines show the used portion. **b** Ω map of the elongated saddle used for propeller's blade. White lines show the used portion. Scale bar is 2mm.

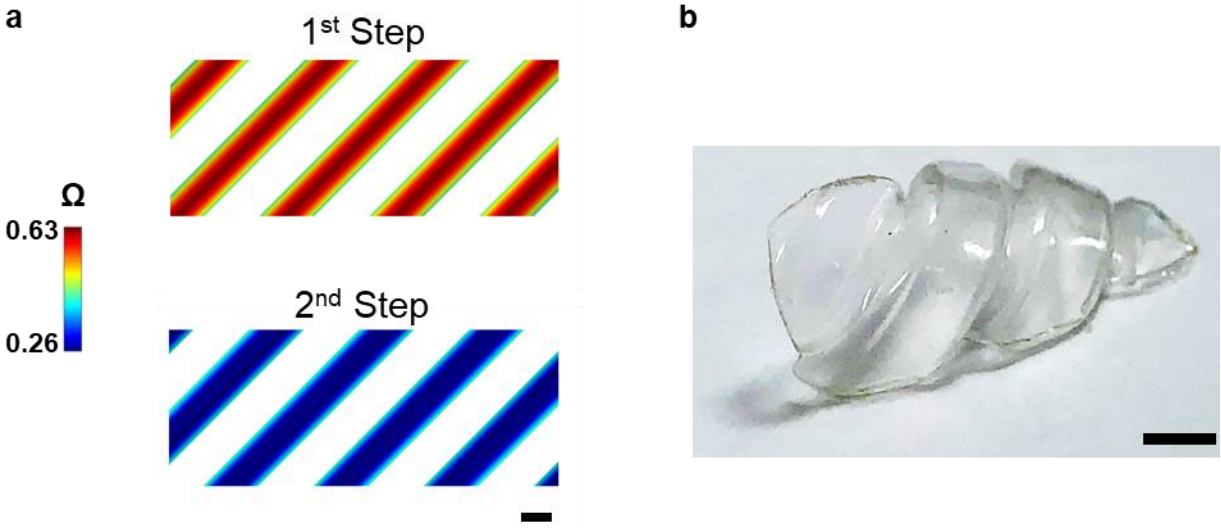

Figure 3-16 **a** Ω map of the 1st step printing using precursor with 5 wt% silica (top) and 2nd step printing using pure precursor (bottom) . **b** Resulted stabilized solid helical structure. Scale bar is 2mm.

3.5 CONCLUSION

Unlike traditional layer-by-layer additive manufacturing, our controlled out-of-plane deformation mechanism allows the creation of 3D structures in a short amount of time from a single layer material. The digital patterning used in this method offers simultaneous printing of 2D materials encoded with custom-designed metrics, rendering it scalable for creating diverse 3D shapes. High throughput fabrication and on-demand shape morphing combined with high mechanical properties, geometrical complexity, and multi-material printing capability offer a new strategy to address the issues and complement the current 3D manufacturing methods.

3.6 MATERIALS AND METHODS

3.6.1 Preparation of pure and composite precursor solutions

0.4 g if N-Isopropylacrylamide (NIPAm) (97%), 5.4 g of N,N′-Methylenebisacrylamide (MBAm) (99%), 3.1 mg of Poly(ethylene glycol) diacrylate (PEGDA) with the molecular weight of 700 g/mol , and 1.84 of Diphenyl(2,4,6-trimethylbenzoyl)phosphine oxide were added to a 1 mL solution of 1:3 volume ratio of water and acetone.

AEROSIL® OX 50 Fumed Silica was added to the main precursor with 5,10, 20 wt% in powder form. For gold nano-particle synthesis, we added 50 ml of deionized water to 20 mg of chloroauric acid ($HAuCl_4.3H_2O$, 99.9%, Sigma Aldrich) in a round-bottom flask. After heating to boiling state, 1.2 ml of 50 mg/ml sodium citrate solution ($Na_3C_6H_5O_7.2H_2O$, > 99%, Sigma Aldrich) were rapidly introduced into the flask with drastic stirring. The mixtures were continuously heated for a certain period until the appearance of a red color[43]. We then purified the solution by centrifuging the solution at 14000 rpm for 15 min for the total of three times. The aqueous solution of gold nano-particles with 0.05 mg of solid gold (40-60 nm) was used to the to make a precursor solution with gold concentration of ~0.05 mg/mL.

3.6.2 General and multi-material printing procedure

Shape-morphing 3D structures were created using our previously established Digital Light 4D Printing (DL4P) method[31]. Dynamic light projection grayscale lithography[31] was used to polymerize and cross-link the precursor solution into a 2D gel with a specific network density

pattern related to the calculated growth function (Ω). Digital light processing (DLP) projector (Vivitek D912HD) was used to spatially and temporally control the ultraviolet (UV) light using the generated STL file. Projection lithography cells were composed of a polydimethylsiloxane (PDMS) spacer with the inner dimension of 57x32x0.4 mm sandwiched between a PDMS substrate and cover-glass. To avoid oxygen interference during polymerization, precursors were nitrogen bubbled for 1 minute before introducing to the cells. Samples cured through the grayscale gel lithography method using a commercial projector as the light source (Vivitek D912HD). Grayscale exposure performed by applying 25 consecutive exposures of 2 sec (exposure level of $L=25^{44}$) to avoid overexposing surrounding XY pixels. Samples were made at 30 μm printing resolution with a total 1920x1080 available pixels. After required exposure, samples were detached from the PDMS side of the cell while attaching on the glass substrate and immediately washed with acetone, IPA, and water (0°C) 3 times to suppress the further reaction. To remove any unreacted monomer from the system, samples were detached from the glass substrate and stored at low temperature (4°C) (for maximum swelling) for three days while the water was being changed every 12 hours.

Multilayer structures were made by printing a second layer over a primary layer. The first layer was printed using the main precursor. Next, the cover-glass (with the parts attached to it) was lifted, and the spacer was exchanged with a thicker (~40-50 um) spacer. The samples' surfaces were then washed with IPA for three times while the first layer was attached to the cover-glass. The second precursor was then introduced to the cell, and the cover-glass (with the first layer attached to it) was placed back to the same position. Finally, the second precursor solution was printed to make the second layer.

3.6.3 Stabilizing the programed flat structures after printing

After printing step(s), samples were detached from the PDMS side of the cell while attaching on the glass substrate and immediately washed with acetone three times. The samples are then immediately dried using air. Samples can be stored for more than seven days in the ambient environment at this state.

3.6.4 Growth Calibration

To control the target metric (Ω) with light exposure, temperature-induced growth was calibrated for samples prepared by different exposure times. Growth ratio was defined as the area of the swelled (positive growth) or shrunk (negative growth) sample divided by the area of the as-prepared samples. The area shrinking ratios were calculated as A_{35}/A_0, where A_0 is the area of as-prepared hydrogel disks (Figure 1C). To measure the shrinking ratio, 5mm diameter digital masks were used for making samples with different exposure times. The areas of the as-prepared gels were measured just after printing, while the samples are still attached to the glass substrate. After being fully swelled at 4°C for three days, hydrogels were slowly heated over T_C temperature (35°C) and kept for 12 hours to ensure most of the water was excluded.

3.6.5 Printing primary shapes with constant Gaussian curvatures

Axis-symmetric shapes of cap, saddle, and cone were printed using known metric functions of eq. (1), eq. (2) and eq. (3), respectively (Fig S.

$$\Omega_{cap} = \frac{\Omega_{\max}}{(1+(r/R)^2)^2}\ , 0 < r/R < \sqrt{\sqrt{\Omega_{\max}/\Omega_{\min}} - 1} \quad (1)$$

$$\Omega_{saddle} = \frac{\Omega_{\max}}{(1-(r/R)^2)^2}\ , 0 < r/R < \sqrt{1 - \sqrt{\Omega_{min}/\Omega_{\max}}} \quad (2)$$

$$\Omega^{i}_{\text{cone}} = \Omega_{\min}\left(\frac{r}{R}\right)^{2(\alpha_i - 1)} \quad (3)$$

Here $\Omega_{\max}$ and $\Omega_{\min}$ are maximum and minimum achievable Arial deswelling rates, respectively and r/R is normalized printing cylindrical coordinate. The samples were printed using R=10mm.

3.6.6 Measuring 3D morphology accuracy

Axis-symmetric shapes of cap and cone with different amounts of programmed radius and deficit angles (δ) were made to study the 3D accuracy of the method with respect to the overall sample sizes. The cap samples were printed using eq. (1) at different R values of 3,5,7,9 and 10 mm.

Cone samples were made through eq. (3) at different α values of 0.5,0.6,0.7,0.8,0.9 and fixing R at 10 mm. The half-vertex angle (β) and angular deficit (δ) can be expressed as below

$$\beta = \text{ArcSin}(\alpha) \quad (4)$$

$$\delta = 2\pi(1-\alpha) \quad (5)$$

3.6.7 The dynamic mechanical properties

The dynamic mechanical properties of hydrogels at both swelled and deswelled states were measured at 25°C and 33°C, respectively, using a rheometer (DHR-2, TA Instruments) with a 20-

mm plate geometry. Hydrogel disks with a diameter of 20 mm were used. The shear storage modulus G′ and loss modulus G″ were measured by frequency sweeps of 0.05–10 Hz at an oscillatory strain of 1%.

3.6.8 Solidification procedure

We created the 3D shapes in shrunk state by implementing the temperature ramp in Figure 3-3**b** on swelled samples. Then we increased the water environment temperature of the 3D formed deswelled structures to 50^{o}C (Figure 3-3**b**). After soaking the samples for one hour, we changed the medium to the near-saturated saline solution (~20 w/v) at 50^{o}C. The samples were removed after 30 min of soaking in the saline solution and blotted and placed on an absorbent tissue to form the stable solid 3D structures.

SEM Microscopy: Air stabilized samples were silver coated for 2 min using CrC-100 sputtering system. SEM images of the surface were taken at different magnifications using Hitachi S-3000N Variable Pressure SEM, under SE mode.

Solid Coating: The solid samples where deep coated with PDMS (~70µm) and then sprayed with 50 µm of paint.

3.6.9 Tensile and hardness analysis of solid structures

Tensile tests were performed on deswelled and air stabilized shape. Tensile tests were performed according to the ASTM D638 standard, where the type V sample was used with the

overall printing size of 50x7.5x0.5 mm. A Microhardness test was performed on dried samples at a load of 0.1 KgF. The hardness in Vickers (HV) was calculated as follows:

$$\mathrm{HV} = 0.1891\frac{\mathrm{F}}{\mathrm{d}^2} \quad (6)$$

3.6.10 3D reconstruction

The 3D images and Gaussian curvatures K of experimentally created 3D structures were constructed based on the spin image 3D recognition method[45]. 3D images were then reconstructed using Autodesz 3Ds Max from the 2D images taken from different angles of the shape. The digital (STL) models were then exported to MATLAB to extract curvature data (Figure 3-9 **b,c**).

3.7 REFERENCES

1.Hu, J.; Meng, H.; Li, G.; Ibekwe, S. I., A review of stimuli-responsive polymers for smart textile applications. *Smart Materials and Structures* **2012,** *21* (5), 053001.

2. Park, S.-J.; Gazzola, M.; Park, K. S.; Park, S.; Di Santo, V.; Blevins, E. L.; Lind, J. U.; Campbell, P. H.; Dauth, S.; Capulli, A. K., Phototactic guidance of a tissue-engineered soft-robotic ray. *Science* **2016,** *353* (6295), 158-162.

3. Maeda, S.; Hara, Y.; Sakai, T.; Yoshida, R.; Hashimoto, S., Self-walking gel. *Advanced Materials* **2007,** *19* (21), 3480-3484.

4.Palagi, S.; Fischer, P., Bioinspired microrobots. *Nature Reviews Materials* **2018,** *3* (6), 113.

5. Techawanitchai, P.; Ebara, M.; Idota, N.; Asoh, T.-A.; Kikuchi, A.; Aoyagi, T., Photo-switchable control of pH-responsive actuators via pH jump reaction. *Soft Matter* **2012,** *8* (10), 2844-2851.

6.Asoh, T. a.; Matsusaki, M.; Kaneko, T.; Akashi, M., Fabrication of Temperature-Responsive Bending Hydrogels with a Nanostructured Gradient. *Advanced Materials* **2008,** *20* (11), 2080-2083.

7.Matsumoto, A.; Ishii, T.; Nishida, J.; Matsumoto, H.; Kataoka, K.; Miyahara, Y., A synthetic approach toward a self-regulated insulin delivery system. *Angewandte Chemie International Edition* **2012,** *51* (9), 2124-2128.

8.Kieviet, B. D.; Schön, P. M.; Vancso, G. J., Stimulus-responsive polymers and other functional polymer surfaces as components in glass microfluidic channels. *Lab on a Chip* **2014,** *14* (21), 4159-4170.
9.Ebara, M.; Uto, K.; Idota, N.; Hoffman, J. M.; Aoyagi, T., Rewritable and shape-memory soft matter with dynamically tunable microchannel geometry in a biological temperature range. *Soft Matter* **2013,** *9* (11), 3074-3080.
10.Zhang, M.; Rabiah, N. I.; Ngo, T. H.; Otanicar, T. P.; Phelan, P. E.; Swaminathan, R.; Dai, L. L., Thermo-responsiveness and tunable optical properties of asymmetric polystyrene/PNIPAM-gold composite particles. *Journal of colloid and interface science* **2014,** *425*, 12-19.
11.Dong, L.; Agarwal, A. K.; Beebe, D. J.; Jiang, H., Adaptive liquid microlenses activated by stimuli-responsive hydrogels. *Nature* **2006,** *442* (7102), 551.
12. Takashima, Y.; Hatanaka, S.; Otsubo, M.; Nakahata, M.; Kakuta, T.; Hashidzume, A.; Yamaguchi, H.; Harada, A., Expansion–contraction of photoresponsive artificial muscle regulated by host–guest interactions. *Nature communications* **2012,** *3* (1), 1-8.
13.Nagase, K.; Kobayashi, J.; Okano, T., Temperature-responsive intelligent interfaces for biomolecular separation and cell sheet engineering. *Journal of the Royal Society Interface* **2009,** *6* (suppl_3), S293-S309.
14.Momeni, F.; Liu, X.; Ni, J., A review of 4D printing. *Materials & design* **2017,** *122*, 42-79.
15.Jamal, M.; Zarafshar, A. M.; Gracias, D. H., Differentially photo-crosslinked polymers enable self-assembling microfluidics. *Nature communications* **2011,** *2* (1), 1-6.
16.Na, J. H.; Evans, A. A.; Bae, J.; Chiappelli, M. C.; Santangelo, C. D.; Lang, R. J.; Hull, T. C.; Hayward, R. C., Programming reversibly self-folding origami with micropatterned photo-crosslinkable polymer trilayers. *Advanced Materials* **2015,** *27* (1), 79-85.
17.Gladman, A. S.; Matsumoto, E. A.; Nuzzo, R. G.; Mahadevan, L.; Lewis, J. A., Biomimetic 4D printing. *Nature materials* **2016,** *15* (4), 413-418.
18.Ding, Z.; Yuan, C.; Peng, X.; Wang, T.; Qi, H. J.; Dunn, M. L., Direct 4D printing via active composite materials. *Science advances* **2017,** *3* (4), e1602890.
19.Jamal, M.; Kadam, S. S.; Xiao, R.; Jivan, F.; Onn, T. M.; Fernandes, R.; Nguyen, T. D.; Gracias, D. H., Bio-origami hydrogel scaffolds composed of photocrosslinked PEG bilayers. *Advanced healthcare materials* **2013,** *2* (8), 1142-1150.
20.Gladman, A. S.; Matsumoto, E. A.; Nuzzo, R. G.; Mahadevan, L.; Lewis, J. A., Biomimetic 4D printing. *Nature materials* **2016**.
21.Kotikian, A.; Truby, R. L.; Boley, J. W.; White, T. J.; Lewis, J. A., 3D printing of liquid crystal elastomeric actuators with spatially programed nematic order. *Advanced Materials* **2018,** *30* (10), 1706164.
22.Arslan, H.; Nojoomi, A.; Jeon, J.; Yum, K., 3D Printing of Anisotropic Hydrogels with Bioinspired Motion. *Advanced Science* **2018**, 1800703.
23. Zhao, Z.; Wu, J.; Mu, X.; Chen, H.; Qi, H. J.; Fang, D., Origami by frontal photopolymerization. *Science Advances* **2017,** *3* (4), e1602326.
24.Jamal, M.; Zarafshar, A. M.; Gracias, D. H., Differentially photo-crosslinked polymers enable self-assembling microfluidics. *Nature communications* **2011,** *2*, 527.
25.Huang, L.; Jiang, R.; Wu, J.; Song, J.; Bai, H.; Li, B.; Zhao, Q.; Xie, T., Ultrafast digital printing toward 4D shape changing materials. *Advanced Materials* **2017,** *29* (7).

26.Kim, J.; Hanna, J. A.; Byun, M.; Santangelo, C. D.; Hayward, R. C., Designing responsive buckled surfaces by halftone gel lithography. *Science* **2012,** *335* (6073), 1201-1205.
27.Boley, J. W.; van Rees, W. M.; Lissandrello, C.; Horenstein, M. N.; Truby, R. L.; Kotikian, A.; Lewis, J. A.; Mahadevan, L., Shape-shifting structured lattices via multimaterial 4D printing. *Proceedings of the National Academy of Sciences* **2019,** *116* (42), 20856-20862.
28.Sharon, E.; Efrati, E., The mechanics of non-Euclidean plates. *Soft Matter* **2010,** *6* (22), 5693-5704.
29.Pikul, J.; Li, S.; Bai, H.; Hanlon, R.; Cohen, I.; Shepherd, R., Stretchable surfaces with programmable 3D texture morphing for synthetic camouflaging skins. *Science* **2017,** *358* (6360), 210-214.
30. Siéfert, E.; Reyssat, E.; Bico, J.; Roman, B., Bio-inspired pneumatic shape-morphing elastomers. *Nature materials* **2018**, 1.
31.Nojoomi, A.; Arslan, H.; Lee, K.; Yum, K., Bioinspired 3D structures with programmable morphologies and motions. *Nature communications* **2018,** *9* (1), 3705.
32.Yan, S.; Jiang, C.; Guo, J.; Fan, Y.; Zhang, Y., Synthesis of Silver Nanoparticles Loaded onto Polymer-Inorganic Composite Materials and Their Regulated Catalytic Activity. *Polymers* **2019,** *11* (3), 401.
33.Kamath, G.; Deshmukh, S. A.; Baker, G. A.; Mancini, D. C.; Sankaranarayanan, S. K., Thermodynamic considerations for solubility and conformational transitions of poly-N-isopropyl-acrylamide. *Physical Chemistry Chemical Physics* **2013,** *15* (30), 12667-12673.
34.Zhang, Y.; Furyk, S.; Bergbreiter, D. E.; Cremer, P. S., Specific ion effects on the water solubility of macromolecules: PNIPAM and the Hofmeister series. *Journal of the American Chemical Society* **2005,** *127* (41), 14505-14510.
35.Uchida, M.; Sengoku, T.; Kaneko, Y.; Okumura, D.; Tanaka, H.; Ida, S., Evaluation of the effects of cross-linking and swelling on the mechanical behaviors of hydrogels using the digital image correlation method. *Soft matter* **2019,** *15* (16), 3389-3396.
36.Levine, H.; Slade, L., Water as a plasticizer: physico-chemical aspects of low-moisture polymeric systems. *Water science reviews* **1988,** *3*, 79-185.
37.Bekas, D.; Hou, Y.; Liu, Y.; Panesar, A., 3D printing to enable multifunctionality in polymer-based composites: A review. *Composites Part B: Engineering* **2019**, 107540.
38.Kim, J.; Hanna, J. A.; Hayward, R. C.; Santangelo, C. D., Thermally responsive rolling of thin gel strips with discrete variations in swelling. *Soft Matter* **2012,** *8* (8), 2375-2381.
39.Wu, Z. L.; Moshe, M.; Greener, J.; Therien-Aubin, H.; Nie, Z.; Sharon, E.; Kumacheva, E., Three-dimensional shape transformations of hydrogel sheets induced by small-scale modulation of internal stresses. *Nature communications* **2013,** *4*, 1586.
40. Byun, M.; Santangelo, C. D.; Hayward, R. C., Swelling-driven rolling and anisotropic expansion of striped gel sheets. *Soft Matter* **2013,** *9* (34), 8264-8273.
41. Moshe, M.; Sharon, E.; Kupferman, R., Pattern selection and multiscale behaviour in metrically discontinuous non-Euclidean plates. *Nonlinearity* **2013,** *26* (12), 3247.
42.MacDonald, E.; Wicker, R., Multiprocess 3D printing for increasing component functionality. *Science* **2016,** *353* (6307), aaf2093.
43.Li, C.; Li, D.; Wan, G.; Xu, J.; Hou, W., Facile synthesis of concentrated gold nanoparticles with low size-distribution in water: temperature and pH controls. *Nanoscale research letters* **2011,** *6* (1), 440.

44.Na, J.-H.; Bende, N. P.; Bae, J.; Santangelo, C. D.; Hayward, R. C., Grayscale gel lithography for programmed buckling of non-Euclidean hydrogel plates. *Soft matter* **2016,** *12* (22), 4985-4990.
45.Johnson, A. E.; Hebert, M., Using spin images for efficient object recognition in cluttered 3D scenes. *IEEE Transactions on pattern analysis and machine intelligence* **1999,** *21* (5), 433-449.

CHAPTER 4

4.1 CONCLUSION

Inspired by biological systems, we introduced a 2D material programming approach based on controlled lateral (in-plane) differential growth to create shape-morphing 3D surfaces with complex morphologies and motions. Our material system with phototunable swelling and shrinking behaviors uniquely allowed us to define target 3D shapes at both swelled and shrunk states. The swelling and shrinking rates of our material systems are also phototunable and thus locally programmable. More importantly, our experimental and theoretical studies revealed that the spatially nonuniform kinetics of 3D structures determines their dynamic shape evolution. Based on these results, we introduced the concept of dynamic target metrics that were used to predict the dynamic shape change of 3D structures. These findings allowed us to design dynamic 3D structures with programmed motions, critical for implementing complex functions but challenging to achieve via global external stimuli. Furthermore, we demonstrate modular design principles to create non-axisymmetric 3D structures with broad morphological diversity.

Next, by developing a thermal/chemical method, we stabilized the 3D morphologies of the target shapes formed in the shrunk state and achieved robust 3D solid structures. The creation of solid 3D surfaces significantly broadens the potential applications of this method as a 3D fabrication technique. We highlighted the versatility of our method by developing a sequential printing approach to make structures with patterns of multiple materials.

In summary:

1. We developed a method to create temperature-responsive hydrogels with a continuous pattern of degrees and rates of growth (swelling and shrinking) from a single prepolymer solution through photo-polymerization.

2. Our study reveals the mechanism of how the photo-polymerization process modulates the material properties of our temperature-responsive hydrogel systems with two types of crosslinkers with different lengths.

3. In contrast to previous studies, which form single stable 3D shapes at either the swelled or the shrunk state, our material systems with phototunable swelling and shrinking behaviors made us able to define target 3D structures at both the swelled and the shrunk states.

4. We developed a theoretical model for axisymmetric 3D shapes that can predict how a target metric translates to a 3D shape and vice versa.

5. We established simple yet versatile design principles that allow us to create nonaxisymmetric 3D structures with broad morphological diversity, including stingray-inspired 3D structures with programmed motions.

6. We solved the challenge of the modular assembly, how to interface modular components controlling their direction of deformation and orientation, by introducing the concept of "transitional components" and "linkers." This concept allows us to design modular 3D structures with complex morphologies through controlled deformation and orientation of modular components.

7. We demonstrated that the spatially nonuniform growth rate of 3D structures determines their progressive 3D shape evolution during temperature change, thereby allowing for programming their motions.

8. We developed the concept of dynamic target metrics that can be used to predict the dynamic shape change of 3D structures, important for the design of dynamic 3D structures (Fig. 4).

9. We found that the swelling and shrinking rates of our material systems are phototunable and thus locally programmable.

10. We demonstrated the ability to spatially control the rates of shape transformations by fabricating a ray-inspired 3D structure with programmed sequential motions.

11. We developed a shape stabilization method to maintain the morphology of the target 3D hydrogels in the ambient environment and achieved robust 3D solid shapes with mechanical properties similar to engineering polymers.

12. To show the versatility of our method in programming surfaces with various metrics, we created well-studied rolled sheets patterned with single direction lateral growth patterns. We demonstrated the advantages of continuous smooth growth patterns in creating structures with the isometric immersion of the target metric, making the shapes more predictable, consistent, and accurate.

13- We further introduced a multi-material approach to construct 3D structures with specific material patterns that enable the creation of 3D shapes with point-by-point material customizability.

Unlike traditional layer-by-layer additive manufacturing, our controlled out-of-plane deformation mechanism allows the creation of 3D structures in a short amount of time from a

single layer material. The digital patterning used in this method offers simultaneous printing of 2D materials encoded with custom-designed metrics, rendering it scalable for creating diverse 3D shapes. High throughput fabrication and on-demand shape morphing combined with high mechanical properties, geometrical complexity, and multi-material printing capability offers a new strategy to address the issues and complement the current 3D manufacturing methods.